LUND UNIVERSITY

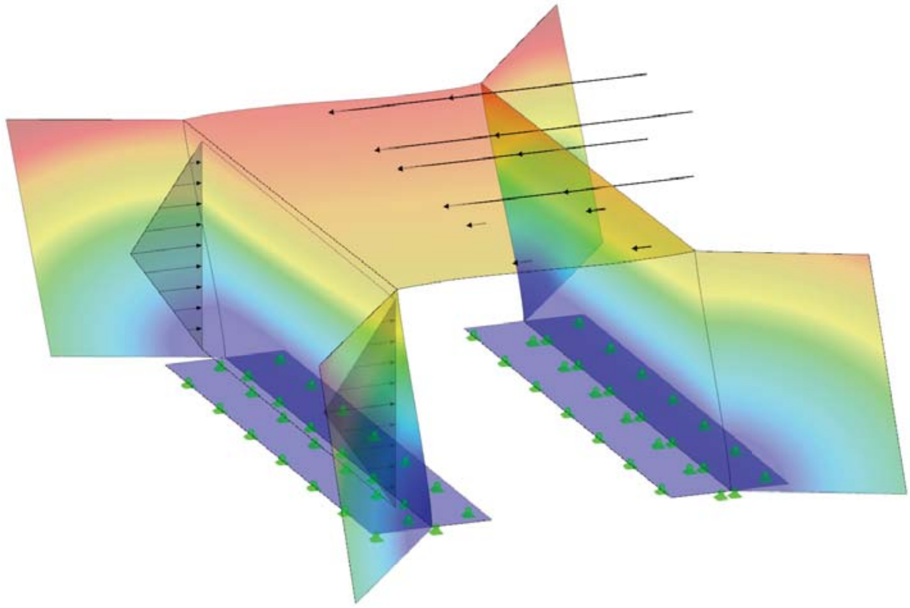

A STUDY ON EARTH PRESSURE ON ABUTMENT WALLS OF PORTAL FRAME BRIDGES

DENIZ AHADI and PHILIP LEWIS

Structural Mechanics

Master's Dissertation

DEPARTMENT OF CONSTRUCTION SCIENCES

DIVISION OF STRUCTURAL MECHANICS

ISRN LUTVDG/TVSM--24/5272--SE (1-164) | ISSN 0281-6679

MASTER'S DISSERTATION

A STUDY ON EARTH PRESSURE ON ABUTMENT WALLS OF PORTAL FRAME BRIDGES

DENIZ AHADI and PHILIP LEWIS

Supervisors: Professor **KENT PERSSON**, Division of Structural Mechanics, LTH
and **SEBASTIAN OKRAJNI**, Consultant, Afry

Examiner: **SUSANNE HEYDEN**, Associate Professor, Division of Structural Mechanics, LTH.

Printed by V-husets tryckeri LTH, Lund, Sweden, June 2024 *(Pl)*.

For information, address:
Division of Structural Mechanics,
Faculty of Engineering LTH, Lund University, Box 118, SE-221 00 Lund, Sweden.
Homepage: www.byggmek.lth.se

Abstract

Portal frame bridges are one of the most popular types of bridges in Sweden. These bridges consists of a framework structure that mitigates the use of bearing supports and expansion joints which in turn makes them economically viable, efficient and robust. The structure makes use of having vertical surfaces such as abutment walls that are in contact with soils, meaning that braking forces, thermal expansion and adjacent loading can be transmitted through the structure into the surrounding soil. This creates intricate soil structure interaction which require careful consideration of how these earth pressures impact the structure.

When calculating increased earth pressure due to horizontal loading, following the Swedish Transport Authority (STA) regulations was necessary. However, the current process was both time-consuming and flawed, neglecting crucial soil mechanics. Commercial software like Dlubal's RFEM offered tools for soil-structure interaction analysis which this thesis employed. Various spring model theories are modelled and compared with STA regulations.

Eight different types of portal frame bridge designs, with five different modelling theories were analysed. Parameters such as span, width, height, thickness and soil characteristics were examined. Each bridge design had a variation of bridge models with varying values of key parameter to derive a result to discern patterns, similarities, and discrepancies across the bridge designs. All spring models were implemented in RFEM with springs that deactivate under tension to simulate soil mechanics more accurately. A few bridges implemented passive earth pressure springs to analyse the impact.

The results showed that all the spring models have movement in the bottom slab unlike the assumptions the STA states. The results also showed that all the spring models had similar contact stresses, with a maximum value at the surface of the abutment wall which decreased with depth reaching a minimum value at the foundation slab. Predictably, the earth pressure distribution of STA models aligned with regulatory standards.

The spring bed models simulated more realistic behaviour of the structure and the distribution of the earth pressure. This lead to a depth varied distribution of sectional forces, which left room for optimizable structural design. The lack of an iterative process decreased the computational time to process a design.

In summary, this master thesis aimed to initiate discussion concerning the necessity of revising the STA, since the methodology to model the earth pressure lacks physical connection. The triangular stress distribution with its peak in the centre of the abutment wall and the restricted movement of the foundation slab inadequately represented the structural behaviour. Moreover, this necessitated a force equilibrium process through an iterative procedure, leading to a time-consuming methodology. The regulation needs reconsideration and refinement of current practises.

Sammanfattning

Plattramsbroar är en av de mest populära brotyperna i Sverige. Bestående av en ramstruktur som minskar behovet av rullager och expansionsleder, vilket i sin tur gör dem ekonomiskt lönsamma, strukturellt effektiva och beständiga. Strukturen utnyttjar vertikala ytor som rambenen vilka är i kontakt med jorden. Detta innebär att bromskrafter, termisk expansion och intilliggande belastning kan överföras genom strukturen till den omgivande marken. Detta skapar komplex interaktion mellan jorden och brostruktur som kräver noggrann övervägning om hur dessa påverkar strukturen.

När ökat jordtryck av horisontell belastning beräknas är det Trafikverkets regelverk som ska följas. Den nuvarande processen är tidskrävande, bristfällig samt försummar avgörande geotekniska egenskaper. Kommersiell programvara som Dlubals RFEM erbjuder verktyg för analys av geokonstruktioner, som detta examensarbete använder. Olika fjädermodeller baserade på olika teorier modelleras och jämförs med Trafikverkets föreskrifter.

Åtta olika typer av plattramsbroar, med fem olika modelleringsteorier analyserades. Parametrar som spännvidd, bredd, höjd, tjocklek och geotekniska egenskaper undersöktes. Varje bromodell hade en uppsättning av broar med varierande värden på västenliga parameter för att urskilja mönster, likheter och skillnader mellan de olika bromodellerna. Alla fjädermodeller implementerades i RFEM med icke-linjära fjädrar som avaktiverades vid dragspänning för att simulera jordens geotekniska egenskaper mer noggrant. På några broar implementerades passiva jordtrycksfjädrar för att analysera effekten.

Resultaten visar att alla fjädermodeller har rörelse i bottenplattan. Det visade sig också att alla fjädermodeller hade liknande utformning på kontakttrycket, med ett maximalt värde vid toppen av rambenet som minskade med djupet och nådde ett minimum värde vid grundplattan. Förutsägbart så följde jordtrycksfördelningen i Trafikverkets modeller med regelverkets bestämmelser.

Fjädermodellerna simulerade ett mer realistisk beteende av strukturen och jordtryckets fördelning. Detta ledde till en mer varierad fördelning av snittkrafterna, vilket lämnar utrymme för en mer optimerbar konstruktion. Genom att inte använda en iterativ process minskades beräkningstiden för att bearbeta en modell.

Sammanfattningsvis ämnar detta examensarbete att initiera diskussion kring behovet att förbättra Trafikverkets regelverk eftersom metoden för att modellera jordtrycket saknar fysisk koppling. Den triangulära spänningsfördelningen med sin topp i mitten av rambenet och den begränsade rörelsen i plattan representerar inte strukturens beteende. Dessutom krävs en iterativ process för att ta fram kraftjämvikt, vilket leder till en tidskrävande metodik. En modernisering av Trafikverkets regelverk och en förfining av nuvarande praxis behövs.

Acknowledgements

This master's thesis was performed at the Division of Structural Mechanics at Lunds University, in cooperation with AFRY AB.

First and foremost, we would like to say our deepest gratitude to our supervisor, Professor Kent Persson at Lund University, for his invaluable help and guidance throughout the project. We also extend our thanks to our supervisor from AFRY, Sebastian Okrajni, for his support and insights during the process.

Special thanks to the people on the fifth floor of the V-house which supplied bread, cheese, coffee and tea throughout the project. Without the provided sustenance the report would never have been finished in time.

As for me, Deniz, I would like to thank my family and my girlfriend for being there, supporting me and motivating me to always have my head up high and to do my best every day during this master thesis.

And as for me, Philip, I'd like to thank my family for supporting and encouraging me throughout my time at the university. The Gustafsson sculpture you gave me has now served its purpose and *lyftet* is now complete.

Finally we both would like to say thanks to the friends that made our time here so memorable.

Lund, June 2024
Deniz Ahadi and Philip Lewis

Table of content

1 Introduction

1.1 Background

Integral bridges are widely used in Sweden because of their ease of construction, lack of bearing supports and expansion joints. They are constructed to handle both vertical and horizontal loads using a framework structure, with bridge spans ranging from 2 meters to 25 meters. Horizontal loads from braking forces, thermal expansion, and surcharge loading are transmitted through the vertical elements to the soil, resulting in increased earth pressure on the abutment walls [1]. This phenomenon is considered during the design of the structure.

Since the structure with the soil is statically indeterminate the soil pressure requires force equilibrium equations and deformations relationships, to determine the load distribution caused by the increased earth pressure - Naturally resulting in soil-structure interaction (SSI) [1]. All traffic related infrastructure is regulated by the Swedish Transport Authority named “Trafikverket”. According to the Swedish Transport Authority TRVINFRA-00227 the increased earth pressure load on a abutment wall has a triangle shaped distribution with the apex in the middle of the abutment walls and zero at the base of the foundation and the surface [2]. This method of calculating the increasing earth pressure is an iterative process which is unfavourable and time consuming for the engineer. This may also create sectional forces in the abutment walls that do not reflect the reality of the situation.

In engineering practise, there exist varying methods on how to model soil-structure interaction. Some methods try to replace the subgrade soil with a structural element such as the Winkler or Pasternak foundation model [3]. Other methods tries to model the soil more physically “correct” using a continuum model [4].

This work will focus on comparing different methods of modelling the soil compared to the Swedish Transport Authority method and regulation. These methods aim to generate a more precise distribution, thereby reducing the time-consuming iterative process associated with the current model.

1.2 Objectives

The objective of this thesis are the following:

- Compare and analyse different soil spring models with the Swedish Transport Authority’s regulations, the differences in the sectional forces and the movement of the abutment wall.

- Draw conclusions in what parameters effects the various bridge models.
- Determine a more adequate soil distribution with the use of spring models in comparison to the Swedish Transport Authority's regulations.

1.3 Limitations

Due to intricacy when modeling integral bridges and foundations, the following limitations have been set.

- Concrete quality has been set to C40/50 throughout the thesis and assumed to have linear elastic behaviour.
- No considerations have been taken into account that the reinforcement affects the stiffness of the structure.
- The concrete is considered uncracked.
- Fatigue behaviour was not studied
- Groundwater effects were not considered, hence the groundwater level was deemed to be well below the structures depth.
- The bridge dimensions where not set to represent realistic portal frame bridge designs, instead the dimensions were chosen to amplify the parametric effects.
- Self-weights are disregarded.
- Only characteristic loading was used.
- The wing walls dimensions where set to be constant through out all bridge models.

1.4 Procedures

This thesis intends to compare the Swedish Transport Authority's calculating regulations of increased earth pressure on the abutment wall of portal frame bridges with different spring based models. This will be achieved by conducting a parametric analysis in the finite element software, on different portal frame bridge designs using various spring foundation theories. The results of the models will be compared with each other by the sectional forces and deformations occurring in the abutment wall.

2 Theory

2.1 Integral bridge

2.1.1 Definition

Integral bridges by definition are when the bridge deck is made without any joints between the structure and embankment. These bridges without expansion joints are divided into two categories “jointless deck” and “integral”. Jointless deck means that there is translational movement between the superstructure and the substructure through bearings. Integral deck has no translational movement between the superstructure and substructure creating a continuous frame [5]. This thesis will focus on the category “integral”, no translational movement between super- and substructure, seen in figure 2.2. Figure 2.1 shows an example of a portal frame bridge.

Figure 2.1: Portal frame bridge located in Norra Fäladen, Lund.

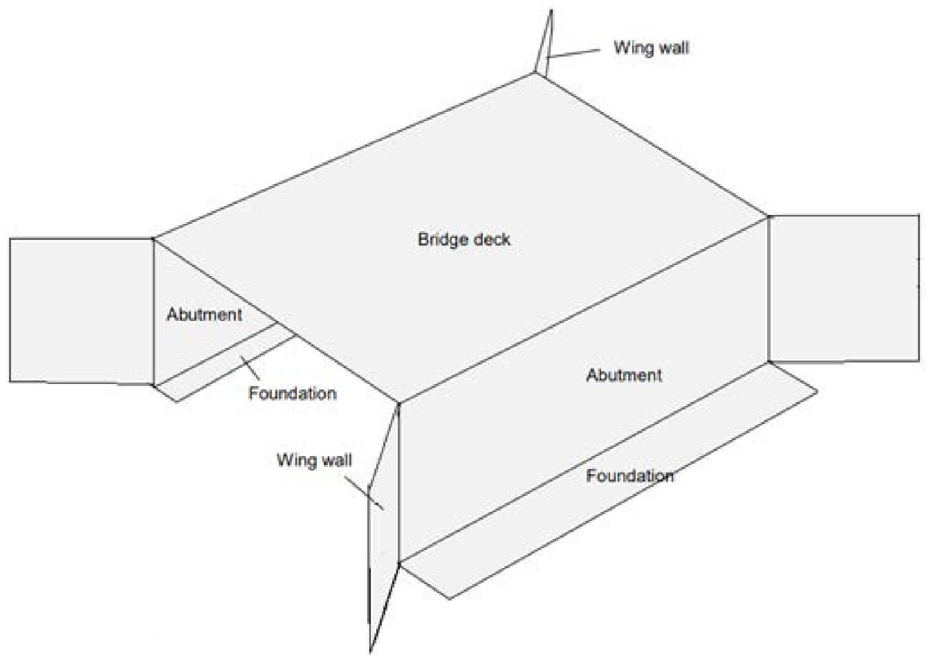

Figure 2.2: The elemental structures of a portal frame bridge.

2.1.2 Characteristics

Integral bridges, also known as portal frame bridges are cost effective and do not necessitate the same level of maintenance as a conventional bridge or jointless deck due to the lack of bearing [6]. The omission of structural elements that separate the superstructure from the substructure leads to distinct statical action compared to traditional bridges with bearing. Integral bridges feature a deck that ends in a diaphragm that is fixed to abutment walls that are rigidly connected to the foundation, forming a frame [5].

Integral bridges can have various configurations of material usage, in the United States there are composite integral bridges spanning 120 meters, in this case conventional elastic analysis fails to explain how the bridge works [6].The standard integral bridge called portal frame bridge which consists entirely of reinforced concrete frame will be the focus of this master thesis.

The frame abutment walls work with the soils and thus derives resistance from them in lateral bending, and restrains movement that is created by forces applied on the deck. This restraining effect can be as beneficial as it is detrimental, in some cases given in figure 2.3 where the soil is trying to restrain thermal expansion leading to increased internal forces. The restraining capability depends on the soil characteristics of the backfill.

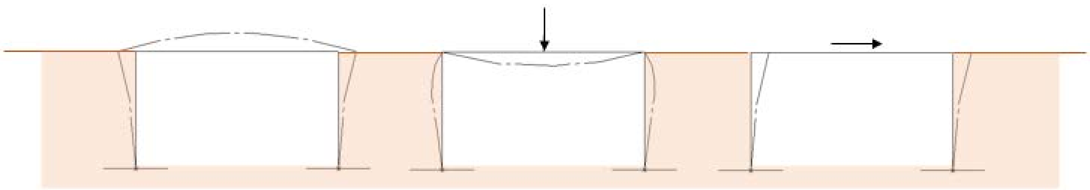

Figure 2.3: Illustration of the movement into the soil occurring from thermal expansion on the left, movement from vertical loading in the middle and horizontal translation from braking forces.

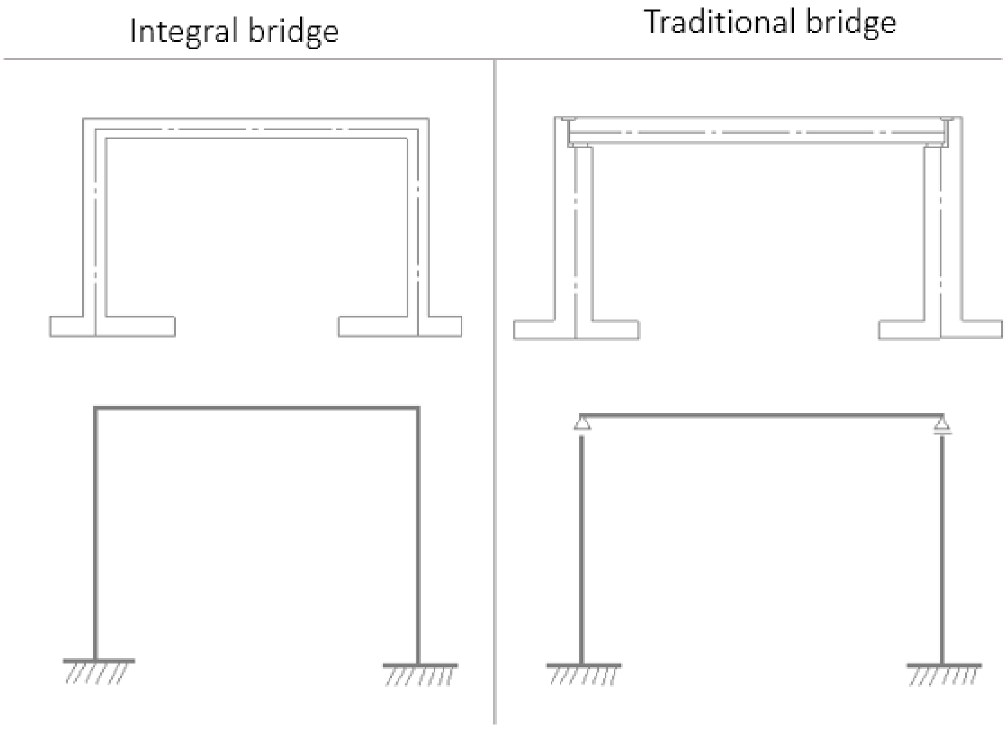

Figure 2.4: The difference in the modelling of a integral bridge compared to a traditional bridge.

2.1.3 Modelling

Portal frame bridges as shown in figure 2.4 illustrates that integral bridges are statically indeterminate where internal forces are influenced by the stiffness distribution of the structure and support displacement.

Constructing a structural model for an integral bridge requires both the superstructure and substructure, given their substantial interaction, unlike in traditional bridges. Likewise, the inclusion of backfill in the integral bridge design is crucial, as the displacement of the structure impacts the stresses exerted on the entire bridge. Horizontal displacement induces cyclic loading on the backfill due to vertical and horizontal traffic loads, as well as thermal expansion shown in figure 2.3. [7]

2.2 Soil mechanics

One of the primary distinctions between soil and other construction materials lies in its multi-phase composition, consisting of soil grains, water and voids known as pores. These pores can be filled with water (resulting in saturated soil) or air. In certain cases, the pores may contain both, resulting in a condition called unsaturated soil. These small differences lead to great differ in the soil behaviour. [8]

Soils are further defined into cohesive and non-cohesive soils. Non-cohesive soils feature direct contact between its particles leading to the forces in the soil being transmitted by friction forces and normal forces. In contrast, cohesive soil is connected via water and the forces are instead transmitted by hydrogen bonding, van der Waal forces and electrostatic interaction. [9]

The groundwater level (GWL) is another factor that will affect the stresses in the soil leading to smaller stress values compared to the same soil above the GWL. This is because the soil will have the effective unit-weight, instead of only the soils unit-weight. The ground water will reduce the unit-weight of the soil based on Archimedes principle. [9]

Additionally, soil behaviour is further complicated by its non-fully elastic behaviour. In fact, soil inhibits plastic deformation almost immediately when loaded, resulting in deformations that are irreversible [8]. Both the plastic and elastic behaviour of the soil depends on the pressure history and the existing stresses in the soil. Especially, the maximum historical pressure, so called pre-consolidation pressure [10].

Furthermore, when studying different soil depths, there are often soil layers with different properties. For simplification of this thesis the soil layers have been assumed to be one homogeneous soil mass, illustrated in the simplified model as seen in figure 2.5 [11].

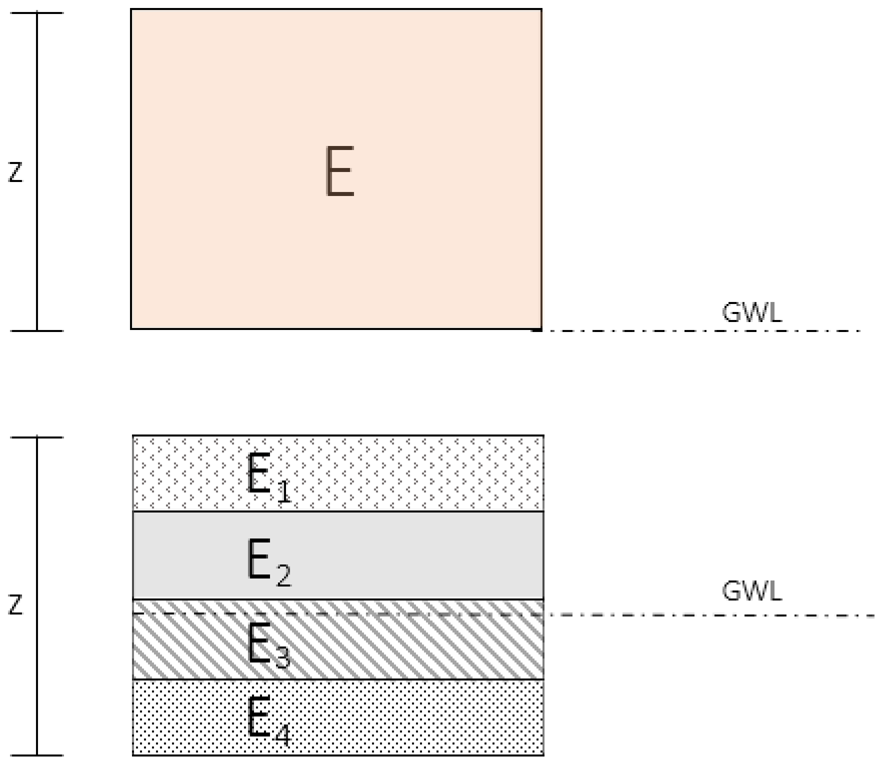

Figure 2.5: Illustrations of Soil layer models with the top one beeing a simple one layer model and the bottom one a multi layer model.

2.2.1 Soil modelling

As mentioned, soil is a material with complex behaviour, notably the nonlinear stress and strain behaviour, the effects of pressure history and the interplay of elastic and plastic attributes [12].

Modelling the soil to prevent plastic deformations is important and this is done by checking the passive and resting earth pressure. When dealing with a retaining wall structure, in this thesis the abutment wall, different types of earth pressure occurs. When a horizontal force is applied the retaining wall will move and deform. The soil against the wall will have a passive earth pressure that varies with depth. If the force is greater then the passive pressure, the soil will be subjected to plastic deformations, passive earth pressure failure occurs. [11]. Calculating the passive earth pressure is important in order to limit the stresses translating into the spring and is done through the equation 2.1. The passive and resting earth pressure coefficients are denoted K_p and K_o respectively. $\sigma_v(z)$ is the earth pressure and $\Delta\sigma_H$ is the earth pressure when considering passive earth pressure failure.

$$\Delta\sigma_H = \sigma_v(z) \cdot (K_p - K_o) \tag{2.1}$$

There are computer softwares that can model numerically and analyse the geotechnical continuums of soil. These programs have the potential to create advanced soil models that can process the extensive variety of soil behaviour. Despite that, subgrade models are more commonly used in foundation engineering for their accuracy in terms of computational efforts. Subgrade models are simple and flexible, only modelling certain characteristics of the soil [3]. There exists a variety of subgrade soil models with different ways of visualizing the model with physical elements as shown in table 2.1 [13].

Table 2.1: Different subgrade models with corresponding visualizing physical elements adopted from [13]

Subgrade model	**Physical element used to visualize model**
Winkler Hypotheses	springs
Pasternak Hypotheses	shear layer + springs
Filonenko-Borodisch	deformed, pretensioned membrane + springs
Rhines	Springs+ plate+ shear layer+ springs
Hetényi	Springs+ plate+ springs

.

2.2.2 Winkler foundation

The Winkler method stands as one of the oldest and most renowned foundation models employed in SSI (Soil-Structure Interaction) analyses. The extensive utilization in both research and engineering foundation practices can be credited to its simplicity and ease of mathematical implementation [3]. Originating from the late 19th century, the Winkler Hypothesis assumes a linear relationship between the deflection, w and the force, p acting on an elastic foundation, where k_w is the Winkler constant (spring stiffness) making it a widely adopted approach [14].

$$p = k_w \cdot w \rightarrow k_w = \frac{p}{w} \tag{2.2}$$

However, one major drawback of the model is that it does not consider the importance of shear mechanisms that occur in a soil as seen in figure 2.6, which illustrates the Winkler soil-models deformation compared to the the real displacement. This happens due to the lack of adequate consideration of proper spring coupling and leads to complications that must be considered when constructing a Winkler model. This has led to the use of more advance models that replicates soil behaviour more realistically than the Winkler model. A trademark of these models is the incorporation of spring coupling that takes the shear mechanism into account [3].

The Winkler model for this project is illustrated in figure 2.6. Where the soil is depicted as an elastic foundation and is represented by a bed of continuous linear springs with the stiffness k_w, solely acting in a single axial direction. The springs are placed against the abutment wall, the wing walls and on the bottom of the foundation slab. The springs are attached to two nodes. However, the bottom nodes are fixed resulting in the deformation in those nodes being zero and are therefore not added to the system of equation of the spring elements.

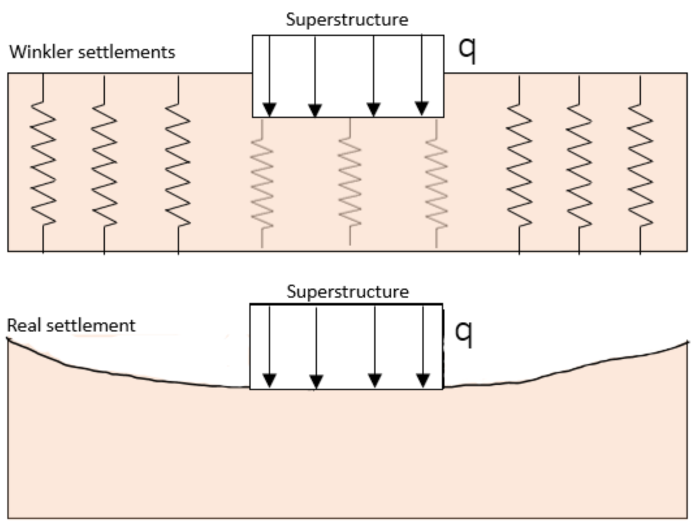

Figure 2.6: Deformation of Winkler foundation compared to realistic displacements.

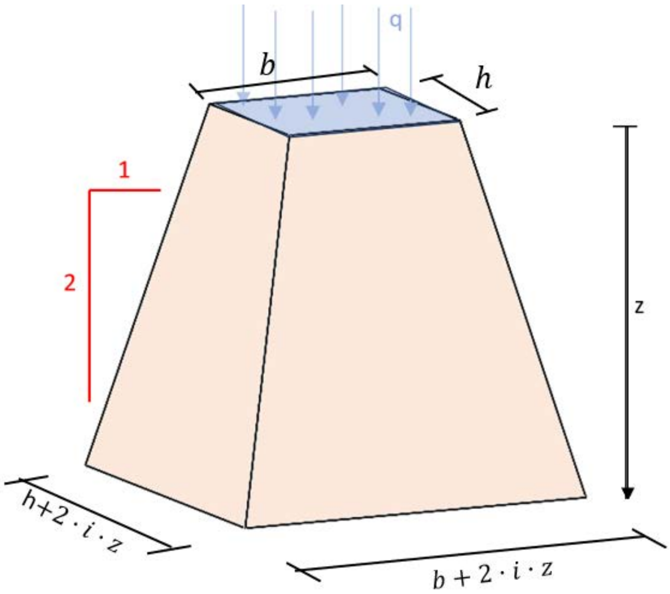

Figure 2.7: Illustration of the stress distribution with a 2:1 inclination.

Spring stiffness and the 2:1 Method

The spring stiffness is derived from equation 2.2 and can be calculated by firstly using the 2:1 method [9] to calculate the approximate stresses in the soil, $\Delta\sigma_z$ from a load q acting on a limited area. Then the displacement, δ can be calculated and with this the spring stiffness can be obtained.

The 2:1 method for a 3-D model distributes the load q on a rectangular area that increases the stress $\Delta\sigma_z$ with the correlation that if the width b and length h, which the load acts on increases by one unit on each side the depth z increases by two units as seen in figure 2.7 and equation 2.3. The inclination i is therefore set to $\frac{1}{2}$.

$$\Delta\sigma_z = \frac{qbl}{(b+z)(l+z)} \tag{2.3}$$

The displacement δ are derived from equation 2.4 where ε_z is the soil strain and E is the soils Young's modulus. The distributed load q when calculating the displacements δ is assigned to the value of $P = 1\text{N}$. This is implemented because the load magnitude does not influence the stiffness of linear springs.

$$\delta = \int_0^z \varepsilon_z dz = \int_0^z \frac{\Delta\sigma_z}{E} dz \tag{2.4}$$

The spring stiffness k_w is then calculated as equation 2.5 where $P = 1\text{N}$ as mentioned previously.

$$k_w = \frac{P}{\delta} \tag{2.5}$$

The primary limitation of the Winkler model used is as mentioned before the lack of shear mechanism, which results in non-accurate displacements because of the complete lack of shear resistance in the soil. This shear resistance, if it was implemented correctly in the model, would distribute the load to a larger area and a more accurate displacement would be obtained. The displacements from the model would then act on a more extensive area and lead to subdued realistic displacement as seen in figure 2.6.

Moreover, the model assumes the soil to be entirely elastic, thereby disregarding its plastic behavior. This implies that if the load is cyclic or entirely removed, the soil would revert to its original shape (non-deformed). This is not true in practice where the soil can develop irreversible deformations.

The Winkler model will be implemented in RFEM using linear springs with a cut-off limit to prevent tension forces. Some analyzed cases will also include a limit that restricts forces beyond the yield stress, coupled to the passive earth pressure. Some of the advantages and disadvantages of a one parameter model in RFEM is presented in table 2.2 [15].

2.2.3 Pasternak foundation

To address the inadequacies of the Winkler model, numerous improved methods have been proposed. One such method, often referred to as a "two-parameter model", The Pasternak hypothesis is a more improved method. Based on the Winkler hypothesis, it addresses some of the shortcomings by introducing shear interactions between the Winkler spring elements. Essentially the Pasternak model is a refined Winkler model, featuring an additional shear layer. This is depicted in figure 2.8 showing a Pasternak model with the shear layer. [16]

Table 2.2: Advantages and disadvantages of a one parameter model in RFEM adopted from [15].

Advantages	**Disadvantages**
Easy input	Inadequate soil modeling
Short computation time	No consideration of the soil's shear resistance
	No consideration of adjacent soil area
	No definition of soil layers
	Few realistic results

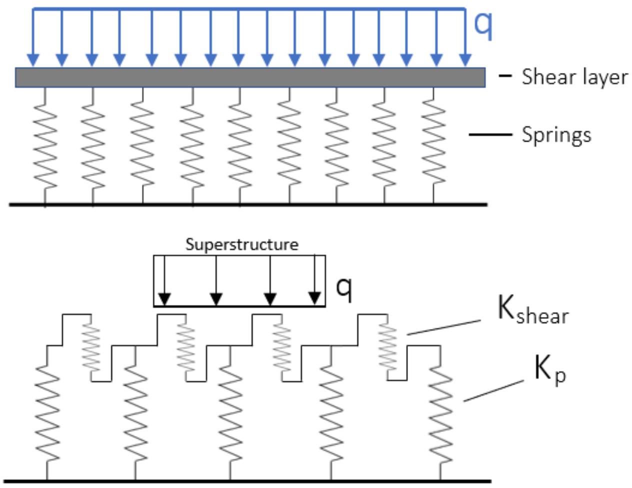

Figure 2.8: Illustration of the Pasternak model.

The Pasternak equation shares similarities with the Winkler equation 2.2. However, it introduces a second parameter that includes shear interaction between the Winkler spring elements due to the added shear layer. When modelling the shear layer, assuming the material is isotropic and homogeneous, the shear modulus of the shear layer is equal to $G_x = G_y = G$. The following differential equation 2.6 is then derived where k_p is the stiffness of the springs and w is the deflection $w = w(x, y)$ and p is the applied pressure. [17]

$$p = k_p w - G \bigtriangledown^2 w \tag{2.6}$$

The challenge when modeling with the Pasternak model lies in its improvement of the Winkler model. When studying equation 2.6 the subsequent conclusion can easily be drawn. If the stiffness of the shear layer is too great the displacements would be underestimated and the foundation soil would also displace in a larger area [15]. In this master's thesis, the Pasternak model will be implemented by using RFEM's own modules.

The advantages and disadvantages using the two-parameter model in RFEM are presented in table 2.3 [15].

Table 2.3: Advantages and disadvantages of a two parameter model in RFEM adopted from [15].

.

Advantages	**Disadvantages**
Realistic results if used properly	Definition of soil layer only approximated
Consideration of adjacent soil areas	Additional considerations and inputs necessary
Consideration of the shear resistance in the soil Short computational time	

2.3 Swedish Transport Authority regulations

The Swedish Transport Authority (STA) is a Swedish government agency. The agency is responsible for the long-term planning and construction of Sweden's aviation, shipping, railways and road traffic infrastructure. Based on societal-development perspective, STA aims to establish conditions for a socio-economically efficient, long-term sustainable transport system that is internationally competitive. Within this, STA is responsible for all the infrastructure regulations that one must follow. [18]

In this master thesis as mentioned before the focus will be on the regulation of bridge type structures in accordance with TRVINFRA-00331 "Bro och broliknande konstruktion, Bärighetsberäkning" [19] and TRVINFRA-00227 "Bro och broliknande konstruktion, Byggande" [2]. More specifically, these regulations manages the increased earth pressure on constructional components horizontal movement against soil. When calculating the increased earth pressure against abutment walls, the regulation in chapter 8.3.5.1 "Ramben, pelare i jordfyllning, pålar m.m."[19] is used and declares the following: Increased earth pressure due to the horizontal movement of the construction against soil shall be calculated according to equation 2.7. Equation 2.7 applies to the level $z = h/2$ and underneath this level the earth pressure shall be assumed to decrease linearly to zero when $z = h$, as a triangular distribution, depicted in figure 2.9.The earth pressure against the abutment wall must not result in passive earth pressure failure and is calculated in Appendix A.2.

$$\Delta p = c \cdot \gamma \cdot z \cdot \frac{\delta}{h} [\mathrm{kN/m^2}] \tag{2.7}$$

Where:

- $c = 300$, when the earth pressure is favourable.
- $c = 600$, when the earth pressure is unfavourable.
- γ, is the soil material unit-weight (mean) from ground level down to the depth z.
- z, is the depth below ground surface [m].
- δ, is the horizontal displacement of the construction at the surface towards the soil.
- h, is the abutment wall height [m].

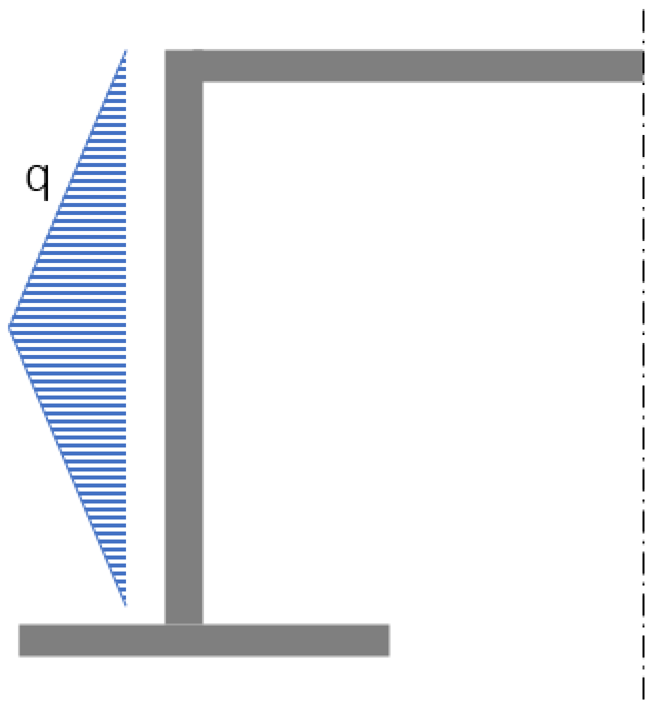

Figure 2.9: Illustration of triangular load distribution on an abutment wall.

2.4 Brigade foundation method

Brigade is a finite element software that uses Abaqus solver from Simulia to ensure accurate and reliable results and is used by civil engineers working in the field. Brigade has a method of replacing the slab of an integral bridge as seen in figure 2.10 with equivalent springs attached to the bottom of the abutment walls. The stiffness of the equivalent springs are calculated by the properties of the slab and soil below to reduce the computational demand. [20]

The rotational spring stiffness are calculated with the following:

$$k_{\theta t} = \frac{E_k \cdot B^2 \cdot L}{5} \tag{2.8}$$

$$k_{\theta l} = \frac{E_k \cdot B \cdot L^2}{5} \tag{2.9}$$

Where E_k is the elastic modulus of the supporting soil, B is the total width of the slab and L is the total length of the slab. The calculation of the vertical spring stiffnesses k_z is based on the relationship between the rotational stiffness and is calculated with the following equation:

$$k_z = 0.5(\frac{k_{\theta t}}{I_t} + \frac{k_{\theta l}}{I_l})A \tag{2.10}$$

This method does not account for horizontal stiffness in the slab and assumes that there is always linear behaviour and complete contact. The structure will completely rely on earth pressure to deal with horizontal movement. For the increased earth pressure, this model can be combined with previously mentioned methods such as the Swedish Transport Authority regulation of an opposite force reaction or applying a spring bed in accordance with the Winkler or Pasternak hypotheses.

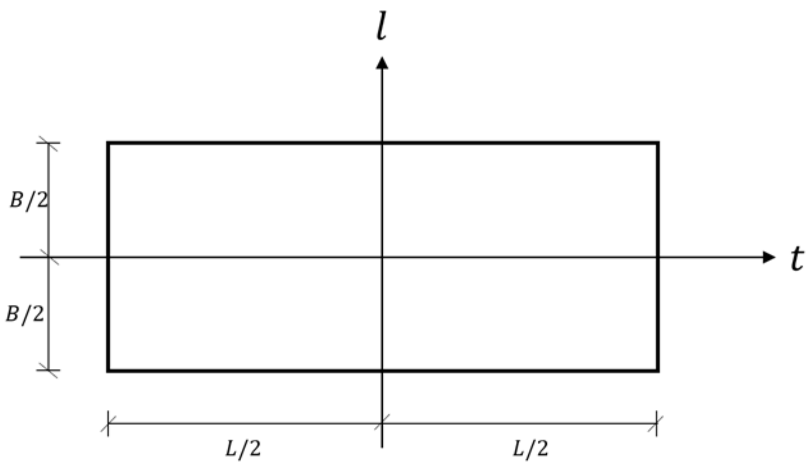

Figure 2.10: Slab dimensions.

2.5 Loads

Only the characteristic braking loads are implemented in the analysis of this work. Other load combinations such as serviceability limit state, ultimate limit state or temperature dependent loads are outside the scope of this thesis and are not implemented. Traffic loads acting on the bridge are described in EC1-2, and the bridge deck is divided into notional lanes with a width of 3 meters shown in figure 2.11. A bridge is designed by dividing the maximum number of notional lanes possible within the width of the carriageway; however, lanes may be left out if proven to contribute to a favourable load effect.

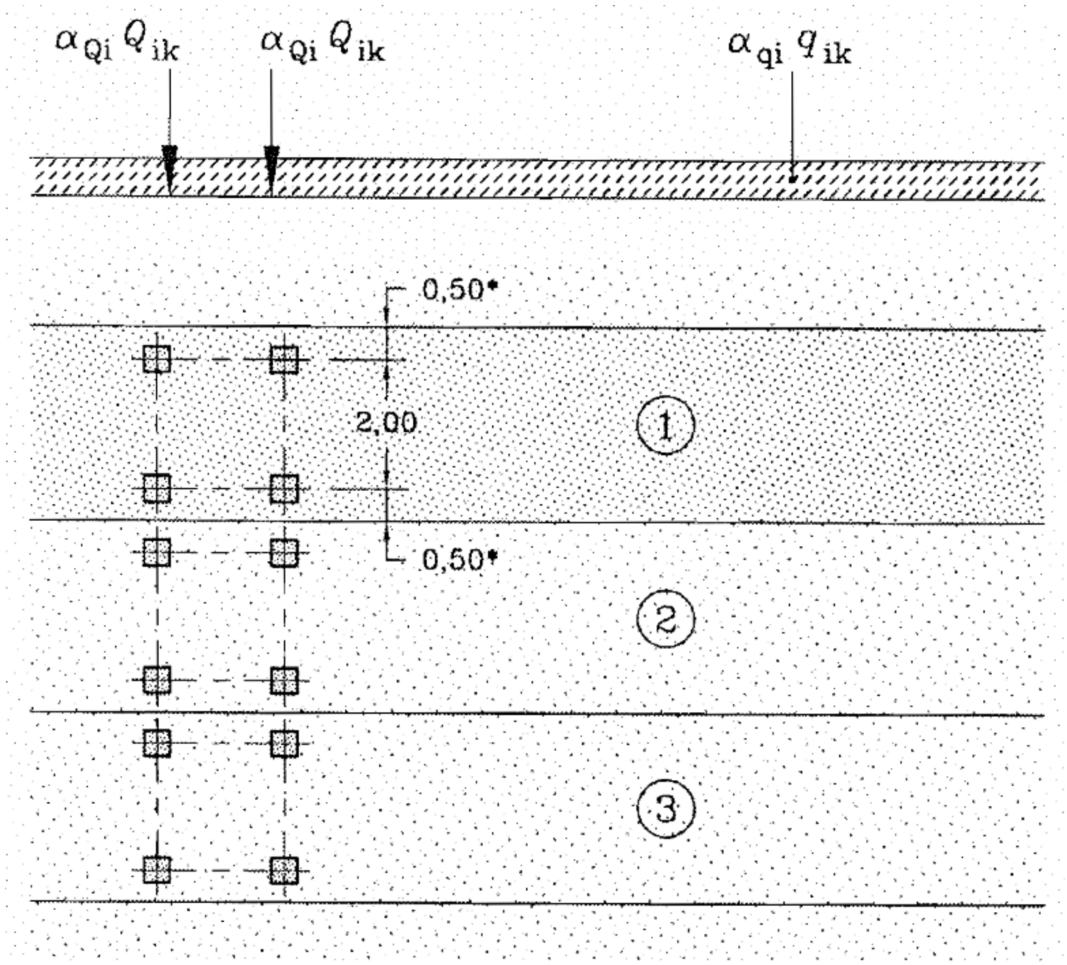

Figure 2.11: Notional lanes according to EC1-2.

Table 2.4: Load magnitude and adjustment factors for each notional lane according to EC1-2.

Location	Tandem system axle load, Q_{lk}[kN]	Adjustment factor, a_{Qi}	UDL system, Q_{lk}[kN/m^2]	Adjustment factor, a_{qi}
Lane Number 1	300	0.9	9	0.8
Lane Number 2	200	0.9	2.5	1
Lane Number 3	100	0	2.5	1
Other lanes	0	-	2.5	1
Remaining area	0	-	2.5	1

Load model 1 which is used for calculating the braking force was derived using SS-EN 1991-2, 4.4.1. The horizontal braking force is denoted as Q_{lk} and is the force from each axle which acts on the bridge deck located on top of the abutment wall. This force is calculated using equation 2.11 and conditions specified from equation 2.12.

$$Q_{lk} = 0.6a_{Q1}(2Q_{1k}) + 0.1a_{q1}q_{1k}w_1L_f \tag{2.11}$$

$$180a_{Qi}(kN) \leq Q_{lk} \leq 900 \text{ [kN]} \tag{2.12}$$

The characteristic loads for the tandem system and uniformly distributed load are from SS-EN 1991-2:2003 and adjustment factors from the National Annex.

- Q_{lk}, characteristic braking force [kN] for each axle.
- a, adjustment factor from National Annex.
- w_i, notional lane width [m].
- L_f, bridge span [m].

$$Q_{1k} = 0.6 \cdot 0.9 \cdot 2 \cdot 300 + 0.1 \cdot 0.8 \cdot 9 \cdot 3 \cdot L_f = 324 + 2.16 \cdot L_f \text{ [kN]} \tag{2.13}$$

$$Q_{2k} = 0.6 \cdot 0.9 \cdot 2 \cdot 200 + 0.1 \cdot 1.0 \cdot 2.5 \cdot 3 \cdot L_f = 216 + 0.75 \cdot L_f \text{ [kN]} \tag{2.14}$$

$$Q_{3k} = 0.60 \cdot 2 \cdot 100 + 0.1 \cdot 1.0 \cdot 2.5 \cdot 3 \cdot L_f = 0.75 \cdot L_f \text{ [kN]} \tag{2.15}$$

$$Q_{Remaining} = 0 + 0.1 \cdot 1.0 \cdot 2.5 \cdot 3 \cdot L_f = 0.1 \cdot 1 \cdot 2.5 \cdot 3 \cdot L_f = 0.75 \cdot L_f \text{ [kN]} \tag{2.16}$$

The braking load is a point load which increases linearly with the length of the span. On top of the length, the load will increase with the number of notional lanes that fit inside the carriageway.

2.6 Finite element method

Many of the challenges encountered by engineering mechanics are modelled with intricate differential equations. Frequently these problems yield into solutions that are to complicated to address with traditional analytical methods. Consequently, a more efficient method is necessary. The finite element method (FEM) is a widely used method for these types of calculations and is one of the most powerful approaches for dealing with complex differential equations to solve a physical problem. [21]

FEM provides a numerical strategy to approximate the solutions of these complex general differential equations. These differential equations formulate the problem over a defined area which can range from one to three dimensions. With the finite element method the structure is divided into smaller segments known as finite elements, allowing it to solve approximate solutions for each element. These elements are then assembled together to construct the entire region. [21]

When modelling in a Finite element program a mesh needs to be assigned to the model. The mesh partitions the structure into a collection of finite elements, each governed by equilibrium conditions. The approximation between each element is done in the nodal points of the mesh. The values at the nodal points can be approximated in different ways, linear, quadratic, cubic and so on. All the finite element calculations in this master thesis are done by using RFEM software. Further information on the finite element method can be obtained from Ottosen and Petersson [21].

2.6.1 Newton-Raphson iteration

Complexity occurs when modelling with Pasternak and Winkler models if the spring elements act with a non-linear behaviour. Due to this the material stiffness matrix changes with each expansion step, where the stiffness matrix describes the stiffness properties of the material. The RFEM software deals with this problem by solving it with Newton-Raphson iterations. The method converges quadratically, hence greater accuracy is achieved for each iteration conducted. The calculations are stopped if convergence cannot be achieved. The Newton-Raphson iteration method is used in RFEM. The function is linearized at a starting point and the stiffness matrix of the preliminary step is used in all iterations. At the point where the function equals zero in the linearized iteration step, a tangent is placed.[15]

The following equations (2.17-2.19) are used in the step chart of the Newton-Raphson iteration. The load is divided into load steps by adding the external load through load increments.

$$^{t+t\Delta}\mathrm{f}_e =^t \mathrm{f}_e + \Delta f \tag{2.17}$$

- t, Time/load step.
- f_e, External load.
- Δf, New load increment.

The predictor step is defined by the equations below and linearizes the stiffness-matrix.

$$^t_0\mathrm{K}\Delta_0\phi =^{t+t\Delta} \mathrm{f}_e -^t_0 \mathrm{f}_i \tag{2.18}$$

- $^{t+t\Delta}\mathrm{f}_e$, Increased external force by a further load step.
- K, Preliminary stiffness matrix.
- ϕ, strains
- $^t_0\mathrm{f}_i$, internal force of the previous time step

The iteration step also called the corrector step, checks if equilibrium is fulfilled, meaning that the sum of the loads is zero. However, this is almost impossible to achieve computationally through the iteration process . To solve this problem RFEM has a built-in break-off limit function. The break off limit function 2.19 interrupts the iteration process when sufficient accuracy has been achieved.

$$R = \left|^{t+t\Delta}\mathrm{f}_e -^{t+t\Delta} \mathrm{f}_i\right| < \epsilon \tag{2.19}$$

- t, Time step
- ϵ, epsilon break-off limit
- R, Break-off limit

- f_e, External load.
- f_i, Internal force.

In figure 2.12, the epsilon break-off limit, ϵ is set to RFEM's default setting which gives a precision of 0.05% [15]. Figure 2.12 shows how the Newton-Raphson method iterates until a sufficient value is achieved. Equation 2.20 shows the function.

$$^{t+t\Delta}\mathrm{R} - ^{t+t\Delta}\mathrm{F}^0 \tag{2.20}$$

The break-off limit is not reached in the first iteration and in the second iteration (Red line). The distance of the tangent stiffness in the third iteration (blue line) is small enough for convergence to be achieved. During the iteration, the deformation Δu^i is summed up.

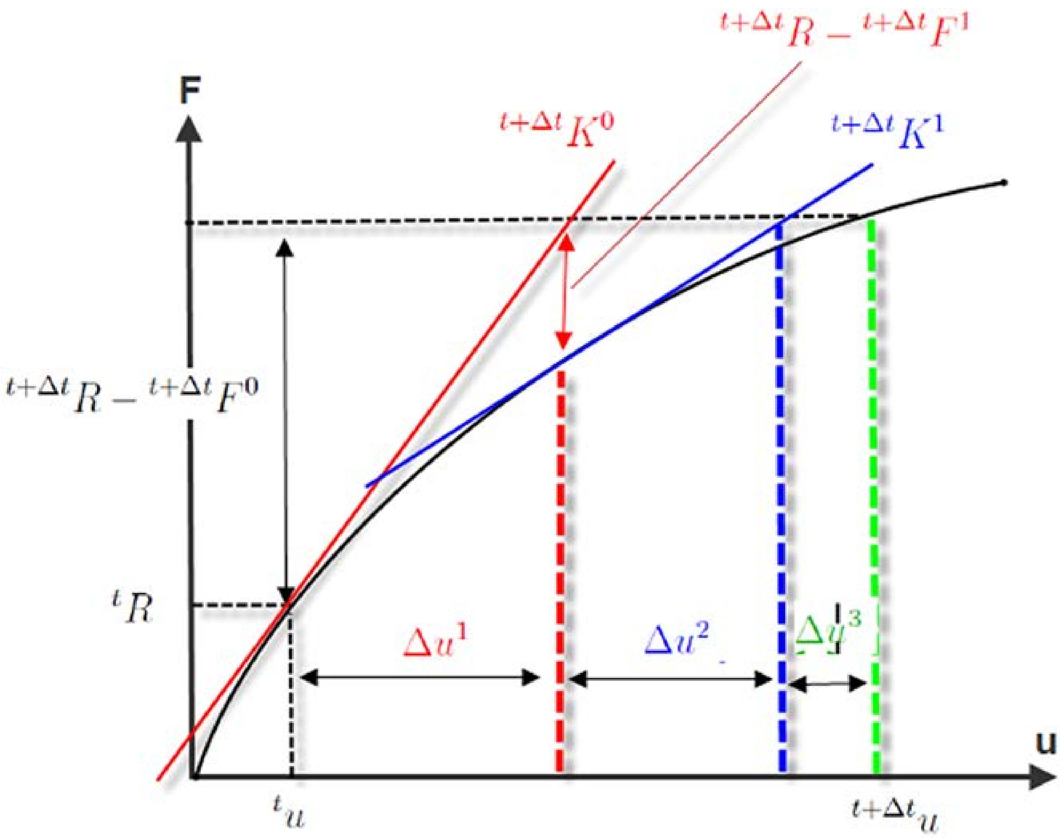

Figure 2.12: First iteration process for Newton-Raphson [15].

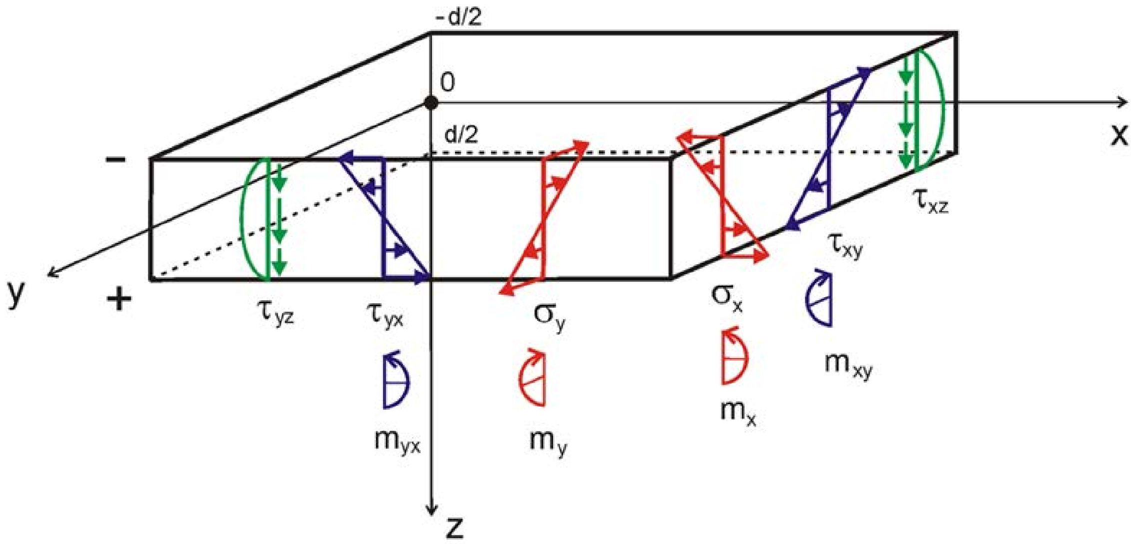

Figure 2.13: Sectional forces for surfaces [15].

2.6.2 Sectional forces

In the process of designing a structure, the derived section forces are of great importance and they are visualized in figure 2.13

There is a fundamental difference between the internal forces acting on a surface and those acting on a member. While a member's moment rotates along its relevant axis, a surface moment operates in the direction of the relevant local surface axis. For instance, the moment m_y rotates about the surface x-axis, and similarly, the moment m_x rotates around the y-axis, as depicted in the figure above. Internal forces and moments for a downward z-axis as illustrated in figure 2.13 are determined using the following formulas, which are applied within RFEM. [15]

$$m_x = \int_{-\frac{d}{2}}^{\frac{d}{2}} \sigma_x z dz \tag{2.21}$$

$$m_y = \int_{-\frac{d}{2}}^{\frac{d}{2}} \sigma_y z dz \tag{2.22}$$

$$m_{xy} = \int_{-\frac{d}{2}}^{\frac{d}{2}} \tau_{xy} z dz \tag{2.23}$$

$$V_{xz} = \int_{-\frac{d}{2}}^{\frac{d}{2}} \tau_{xz} dz \tag{2.24}$$

$$V_{yz} = \int_{-\frac{d}{2}}^{\frac{d}{2}} \tau_{yz} dz \tag{2.25}$$

In this thesis the torsional moment $M_{xy} = M_{yx}$ will not be regarded as much as the main axis moments M_x and M_y, since the forces along the main axis of the abutment surface will be the focus of evaluation.

2.6.3 Contact stress

For foundation design, the contact stresses on the foundations are of utmost importance for an engineer. To compare the earth pressure from the different models the contact stresses from the abutment wall surfaces are vital. This is done in RFEM where the contact stress σ_z, is defined in equation 2.26. [15]

$$\sigma_z = \frac{F_z}{A} \tag{2.26}$$

F_z is the contact force in local z-axis in the finite element node.

A is the finite element nodes application area.

For some models the maximum contact stresses are limited according to equation 2.27.

$$\sigma_z \leq \Delta\sigma_H \tag{2.27}$$

Deriving the maximum contact stresses $\Delta\sigma_H$, for the models that implement passive earth pressure springs is mentioned previously in chapter 2.2.1.

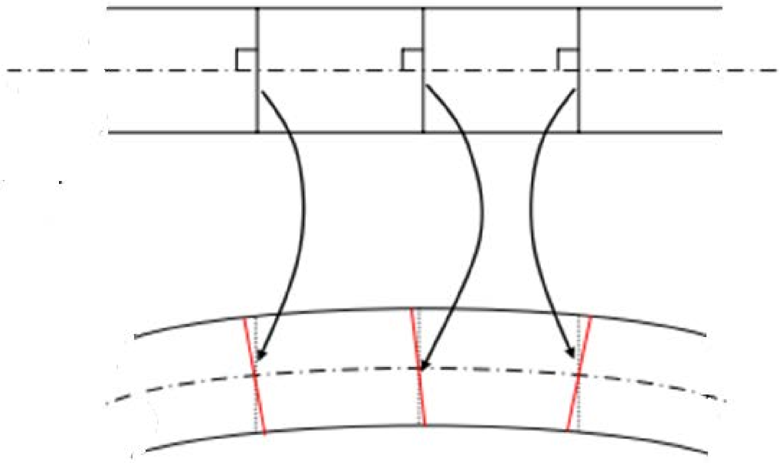

Figure 2.14: Illustration of the post-deformation axis not being perpendicular to the undeformed state.

2.6.4 Mesh

The model will consist of planar shell elements based on Reissner-Mindlin plate theory [15]. The theory is applied in cases involving thick plates, incorporating shear deformation and inertia, and it does not necessitate the post-deformation axial axes to be perpendicular to the undeformed cross-section as shown in figure 2.14 [22].

Each element consists of four nodes with six degrees of freedom that facilitates displacement and rotation of x,y and z-direction as seen in figure 2.15.

These four node linear elements opposed to eight node quadratic elements reduce computational efforts while providing accurate results and allow wall elements to be directly coupled to beam elements. However it is not recommended to implement point-by-point torsional stresses into the rotational degree of freedom since this specific degree of freedom is very responsive in shell elements [15]. In classical plate theory (Euler-Bernoulli) the strains γ_{xz} and γ_{yz} are zero, however as stated before the Reissner-Mindlin theory allows shear deformation meaning $\gamma_{xz} = \gamma_{yz} \neq 0$.

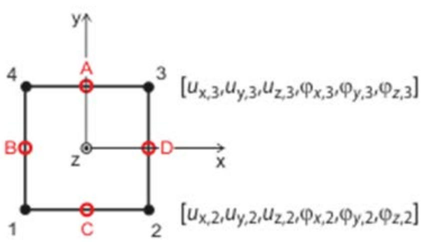

Figure 2.15: Element consisting of four nodes and a total of 24 degrees of freedom [15].

3 Method

3.1 Definition of models

3.1.1 Geometry

Various geometries were analyzed in the modelling, but some constraints have been set to the geometry to allow ease of comparison. All models consisted of a foundation connected to a framework of a bridge deck and abutment walls. Some examples of studied models are shown below in figure 3.1, ranging from large spans to smaller width and varying foundation design.

The various parameters that were studied was the height of the bridge, span length, width, abutment wall thickness and foundation size. The parameters affect the bridge in various ways described in the theory behind soil mechanics (chapter 2.2) and loads applied on a portal frame bridge. The width, height and foundation size of the bridge affects the spring stiffness according to the 2-1 method of stress distribution in the soil. The span length affects the load magnitude in accordance to the Eurocode derived in chapter 2.5 Loads.

The wingwalls were included in the models but were not of varying design. They are of a square design, set to protrude three meters at a 45-degree angle from the abutment walls in every model and equal in height to the abutment walls. The foundation, bridge deck and abutment walls were set to equal width in every design. When the models were created in RFEM the structure was created as one part meaning that the concrete surfaces are tied together creating moment stiff corners between the various structural parts, since uncracked concrete was assumed.

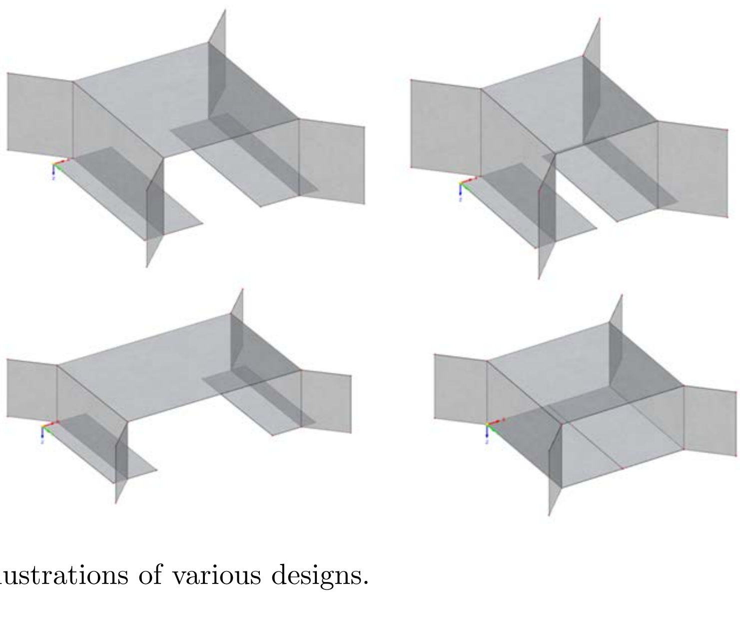

Figure 3.1: Illustrations of various designs.

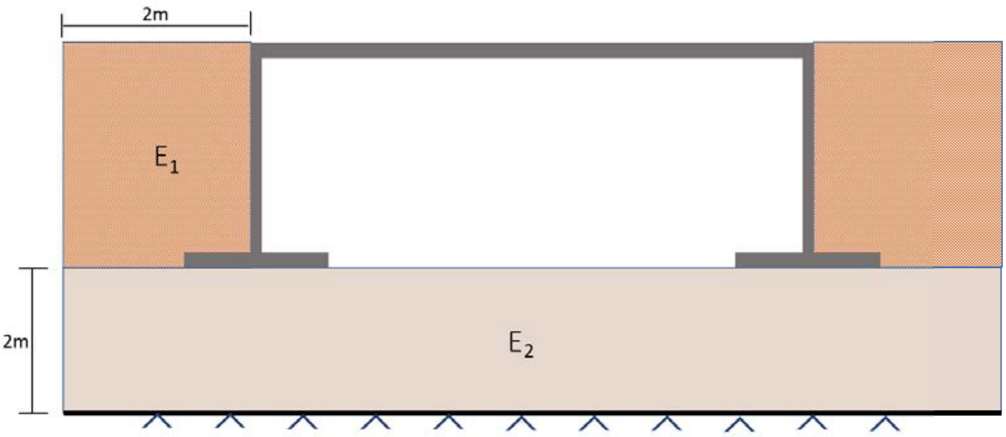

Figure 3.2: The soil condition around the bridge.

3.1.2 Foundation design

A foundation analysis was conducted which analysed the impact various soils had on the bridge designs by changing the elastic modulus of the soil $E1$ and $E2$ as seen in figure 3.2, these designs are presented in chapter 3.3.2. Once the analysis of various soils was completed, a standard was chosen to be used throughout the parametric study. Below the foundation slab there were two meters of densely compacted gravel with a high elastic modulus of $E2$=100 MPa. The soil by the abutment walls was compacted backfill with an elastic modulus of $E1$=50 MPa derived from Appendix A.1, Table A.1. These values impacted the stiffness of the springs that were applied to the surfaces for the Winkler and Pasternak model. However, since the elasticity was constant only the dimensions of the surfaces in contact with the soil will change the applied spring stiffness.

3.1.3 Model verification

In this chapter the models in RFEM were verified to ensure reasonable structural behavior.

The self-weights of the concrete structure are implemented using RFEM modules, choosing European standard with a concrete quality of C40/50. The Models were verified by checking the maximum deflection of the mid span for all the base models for Bridge 1-1 due to the structures self-weight with comparison to hand calculations of two different elementary cases. The span in the middle should act between two cases, a simply supported beam and a beam that is fixed in both ends. With more similarities to a beam with fixed ends, see Appendix A.5.1.

The moment distribution of the bridge deck was checked to see if the moment distribution is similar to the elementary cases shown in A.5.1. The result from Appendix A.5.1 yielded to the conclusion that the model tested had reasonable structural behaviour. It is from here on out assumed that all the models tested in RFEM will have reasonable structural behaviour, due to the geometrical similarities.

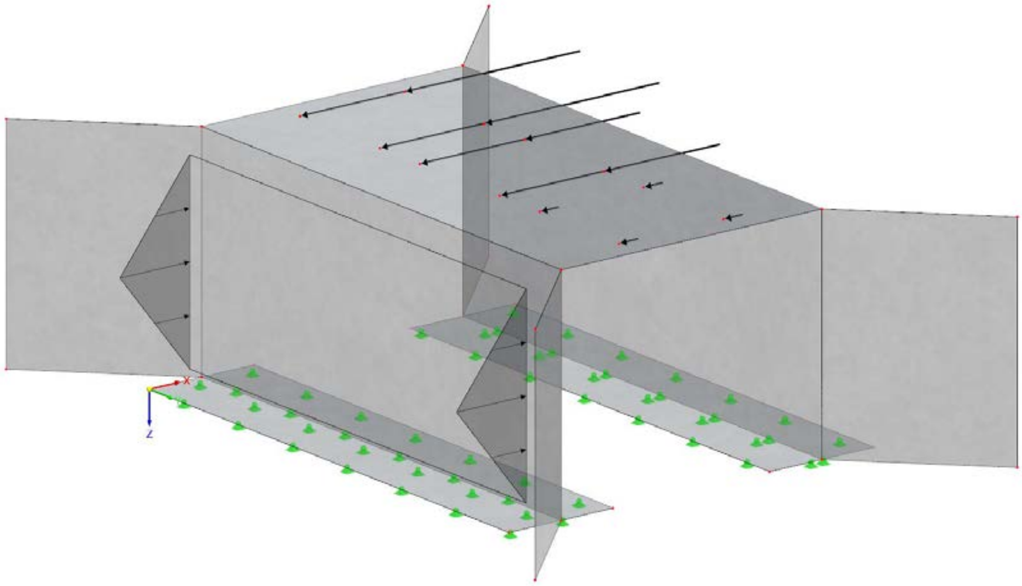

Figure 3.3: An example of how the STA method is applied.

3.1.4 Swedish Transport Authority model

When modelling in accordance to STA, the foundation slabs were set to have zero displacements in all axial directions. The braking loads were implemented according to chapter 2.5. The earth pressure when implemented, was placed as a surface distributed triangular load on the abutment wall, acting in horizontal direction. The wing walls were not included and were not subjected to any earth pressure in the STA model, however still contributed to the overall stiffness of the structure. The RFEM model is depicted in figure 3.3.

The triangular earth pressure was calculated as mentioned in chapter 2.3. This was an iterative process, where firstly the model was loaded with no earth pressure and braking loads. The deflection at the top of the abutment wall was then extracted and implemented in STA's equation 3.1 to calculate the favourable earth pressure. The calculated earth pressure was then applied in the model to receive a new deflection at the top of the abutment wall. Once again, the new deflection received was implemented in equation 3.1 and a new earth pressure was calculated and implemented in the model again. This process was repeated until equilibrium of the relative error was achieved in u_i, as depicted in figure 3.4. See calculations in Appendix A.6.

$$\text{Relative error } (u_i) = \frac{u_i - u_{i+1}}{u_i} \tag{3.1}$$

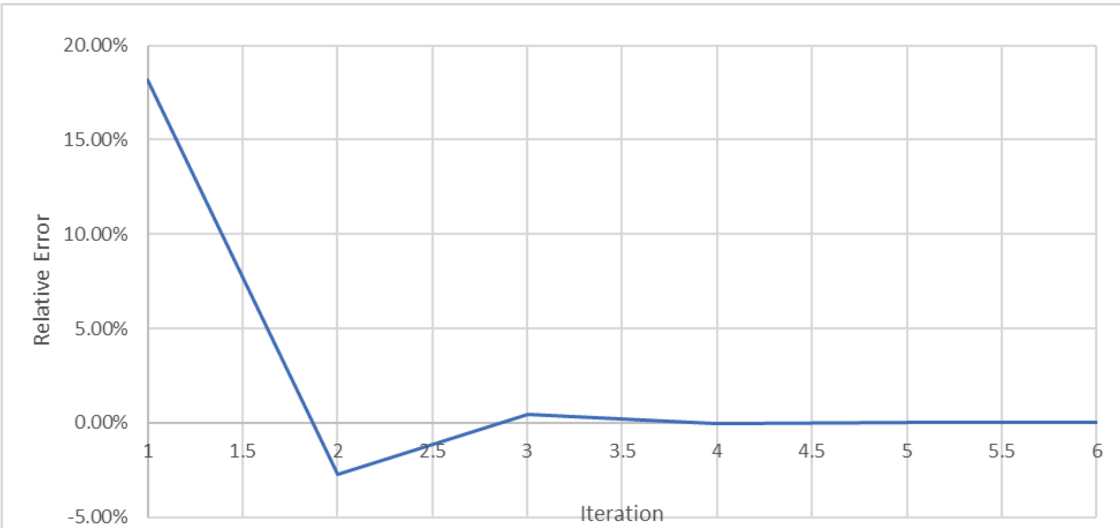

Figure 3.4: Shows an example diagram for the number of iterations it can take for a model to reach full load equilibrium.

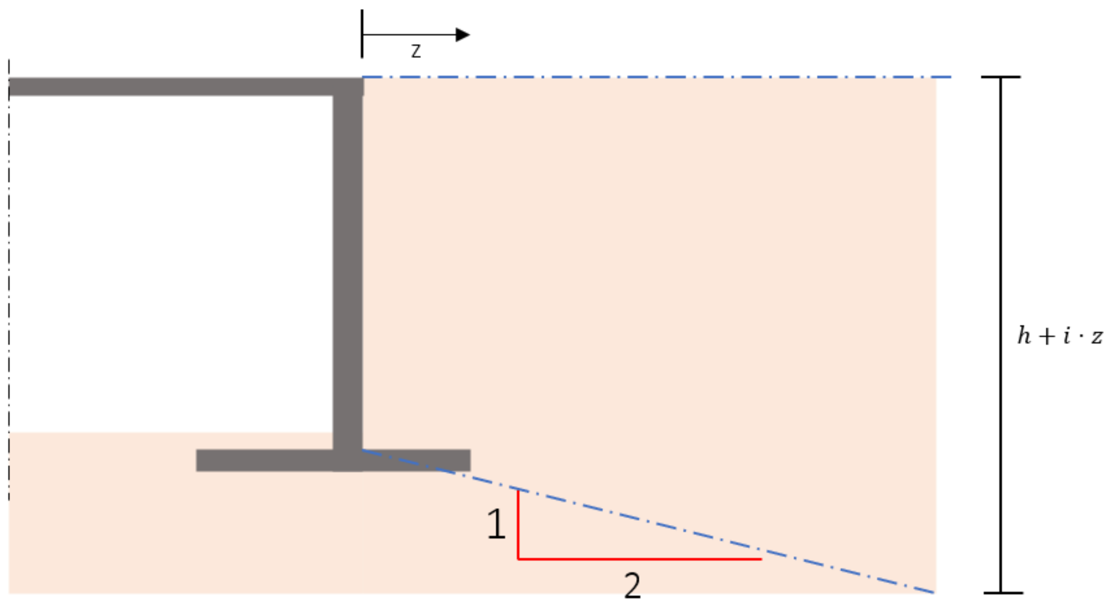

Figure 3.5: Illustration of the modified 2-1 method for abutment wall.

3.1.5 Winkler model in RFEM

The Winkler method was utilized, incorporating non-linear spring elements to model the soil structure. These spring elements were positioned perpendicular to the bridge model surface, acting as axial supports. In determining the stiffness of these springs k_w, a uniform vertical load of magnitude 1 was assumed on the slab, as described in chapter 2.2.2. The process was repeated for the vertical spring bed on the abutment walls and wingwalls, with modifications to accommodate the soil's limited ability to distribute loads beyond the carriageway surface was employed, based on equation 2.5 in chapter 2.2.2. In this modified method, the depth z is plotted on the horizontal axis, and the increased stress $\Delta\sigma_z$ correlates with a 2-1 ratio with the depth and area on one side, without stress distribution on the other side seen in figure 3.5. Further calculations are provided in the Appendix A.4.

The entire vertical structure, including the wing walls, contributes to the earth pressure due to springs being applied to the surface. Additionally, braking loads were applied as described in Chapter 2.5 on the bridge deck surface and seen in figure 3.6 below.

The model was restricted in vertical and horizontal y-axis movement from the boundary condition set to the abutment wall line in the slab, seen in figure 3.6. Furthermore, there are springs placed on the entire surface of the slab and since the vertical boundary condition is only set on a line it allowed for rotation in the slab, hence the need for non-linear springs to simulate a slab placed on soil.

Additionally, springs were added to the line of the slab (green line in figure 3.6) that would simulate the thickness of the slab going into the soil as well as the friction on the bottom of the slab.

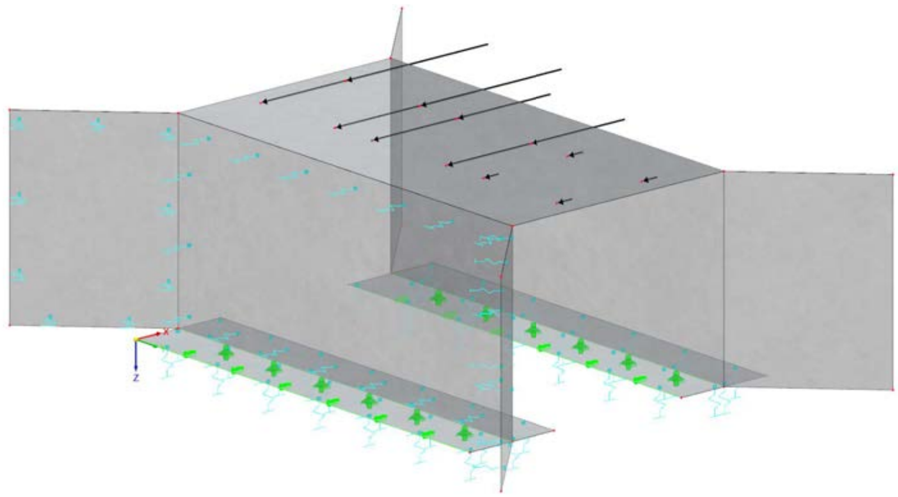

Figure 3.6: Example of how the Winkler model is applied on the designs.

3.1.6 Pasternak model in RFEM

The springs, boundary conditions and loads in the Pasternak model were implemented the same way as for the Winkler model as detailed in chapter 3.1.5 with non-linear surface spring supports, in accordance with Dlubal. The spring stiffnesses k_p in the Pasternak model were set equal to the stiffness k_w from the Winkler model. Additionally, the shear stiffness of the springs in the Pasternak models were equated to the spring stiffness k_p. The braking loads for the models were implemented as described in chapter 3.1.5. [15]

3.1.7 Brigade method

For the Brigade model, the slab was removed from the model and replaced with equivalent springs seen in figure 3.7 which allowed movement in vertical direction unlike the other models. Movement was restricted in y-direction as this movement was of no interest comparably with the other models. The increased earth pressure is modelled using both Winkler and Pasternak spring beds for comparable results to the previously mentioned models.

Steps for deriving the stiffness of the springs that replace the slab was presented in chapter 2.4 and calculated in Appendix A.7.

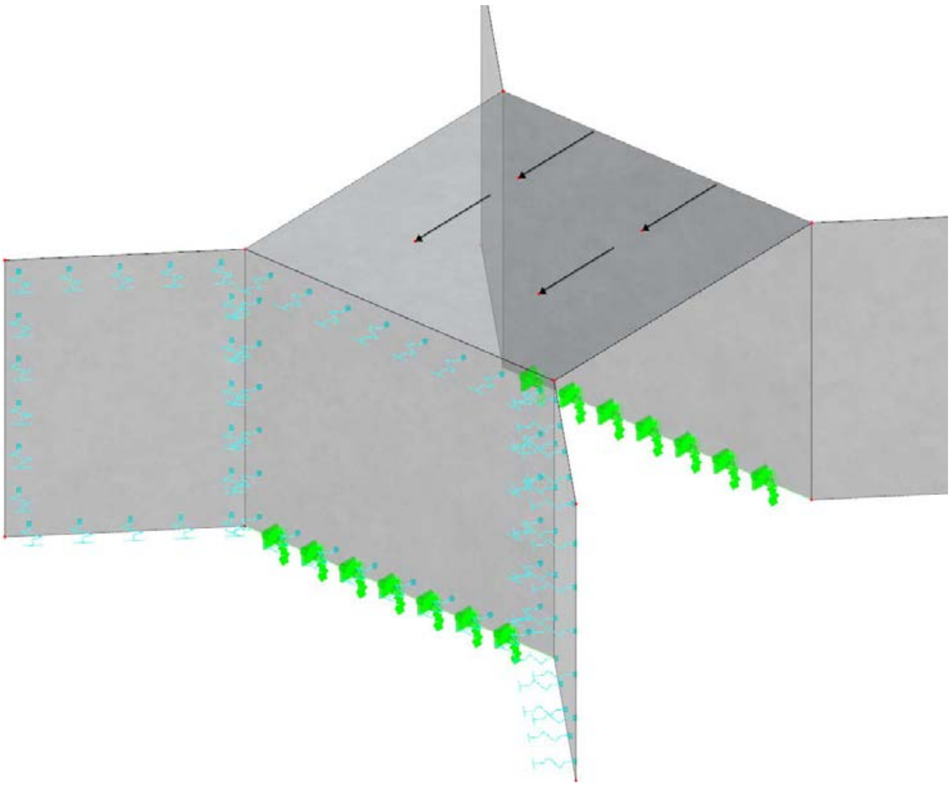

Figure 3.7: Example of how the Brigade model is applied on the designs.

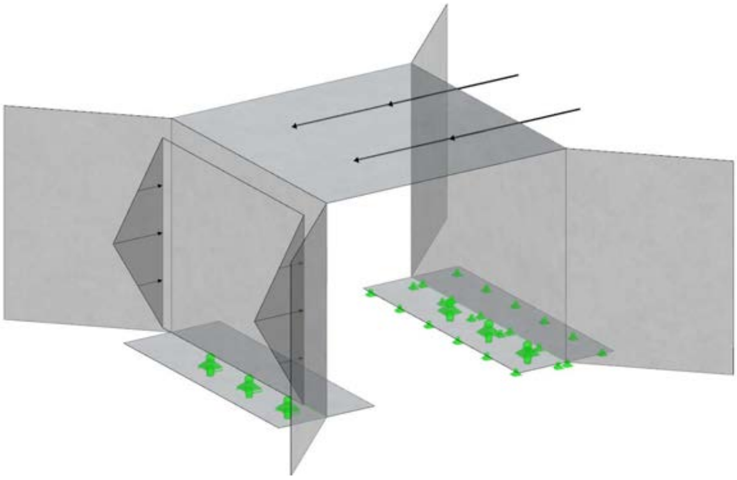

Figure 3.8: STA model with restricted movement on the side not experiencing any earth pressure and only restricted vertically on the side where the earth pressure is active.

3.1.8 Translational analysis of STA model

For the Translational analysis of the STA model the foundation slab on the side of the bridge not experiencing increased earth pressure is restricted in all directions while the other side of the bridge facing the soil is only restricted vertically, as can be seen below in figure 3.8.

Since the setup above still allowed for one side to hinder translation of the foundation slab through the stiffness of the structure, an additional design was implemented, with an arbitrary stiff rotational spring joint located at the base of the restricted foundation slab illustrated by the red marker in figure 3.9. The additional design acted as an intermediate between the standard design and only relying on increased earth pressure according to the Swedish Transport Authority regulations to stop translational horizontal movement of the abutment wall.

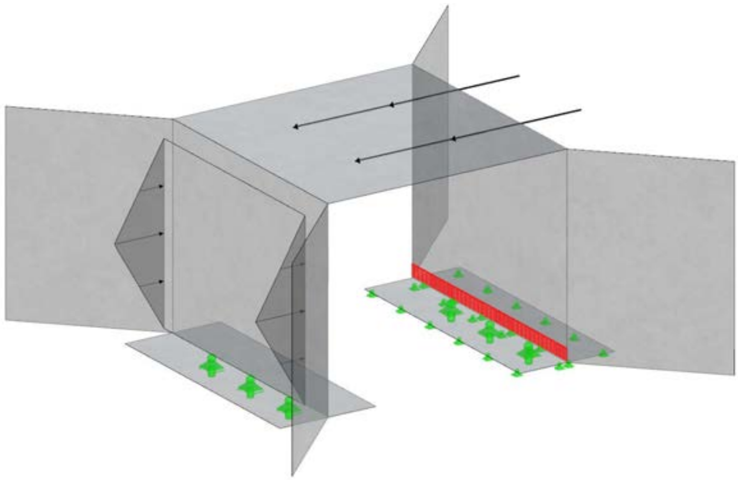

Figure 3.9: STA model with an additionally added arbitrary stiff rotational spring joint (red line).

3.2 Finite element model

In this chapter, the finite element modelling configurations utilized in RFEM are described. The analysis conducted was geometrically linear, indicating a first-order analysis where equilibrium was assessed based on the undeformed structural system. Direct equation system was employed to eliminate the need for iterations; however, the presence of nonlinearities required iterative processes. To ensure clarity, the nonlinear equation system was solved directly through iterative calculations where Newton Raphson was employed, as detailed in Chapter 2.6.1. As discussed in Chapter 2.6.4, the Reissner-Mindlin plate theory was adopted for the shell elements used in all models.

3.2.1 Mesh and mesh convergence

To ensure accuracy, stability and efficiency of the computed models, a thorough mesh convergence analysis is imperative. Having accuracy and stability in a model denotes that the model converges to the same result as a very fine mesh with many nodal elements. The challenge with increased nodal elements is the decrease of model efficiency. The objective with mesh convergence is to obtain a mesh that is fine enough to ensure stability and accuracy of the model whilst ensuring manageable computational efforts.

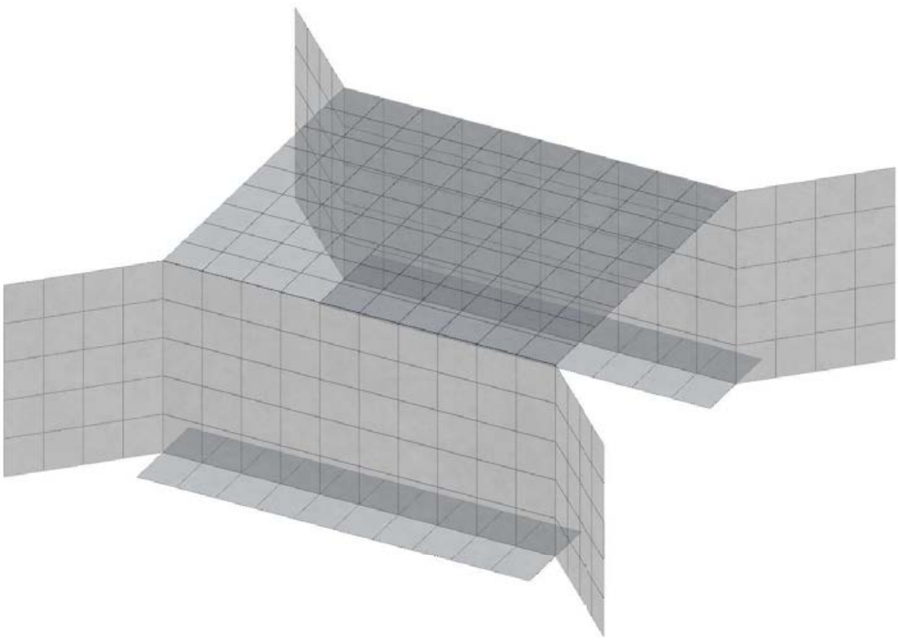

Figure 3.10: Meshed RFEM model with the shell elements rendered onto the surfaces of the structure.

The mesh convergence analysis was done by testing the model with different mesh sizes and plotting the relative error of the deflection, u and the moment, m_x, m_y against the different mesh sizes. The deflection and moments are taken from the same point as shown in figure 3.12. The relative error is calculated using equation 3.2 for deflection and equation (3.3-3.4) for moments, where the maximum deflection, u_{max} and the maximum moment, is obtained from the finest mesh conducted.

$$\text{Relative error } u = \frac{u_{max} - u}{u_{max}} \tag{3.2}$$

$$\text{Relative error } m_x = \frac{m_{x,max} - m_x}{m_{x,max}} \tag{3.3}$$

$$\text{Relative error } m_y = \frac{m_{y,max} - m_y}{m_{y,max}} \tag{3.4}$$

The mesh convergence was performed on the smallest design (see appendix 4.1), with fixed supports at the bottom slab and a braking load applied in accordance with chapter 2.5 loads. For simplicity and ease of comparing results, the mesh size will be set to 0.1 meters throughout the parametric study. Which was equivalent to 13300 number of elements for the smallest design and corresponded to a relative error of roughly 0.5% for the analysed parameters.

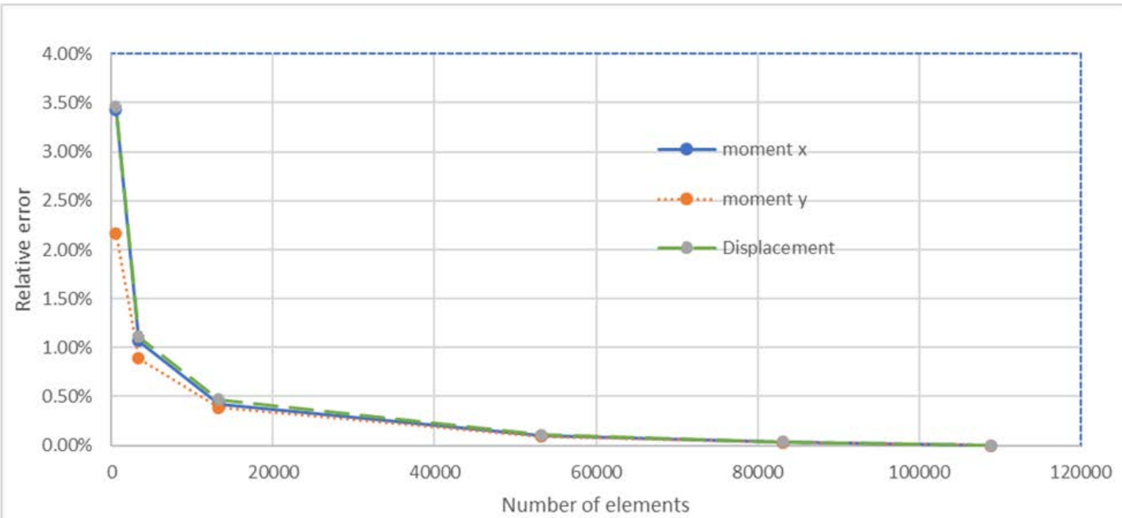

Figure 3.11: Resulting mesh convergence analysis for moments m_x,m_y and horizontal deflection u.

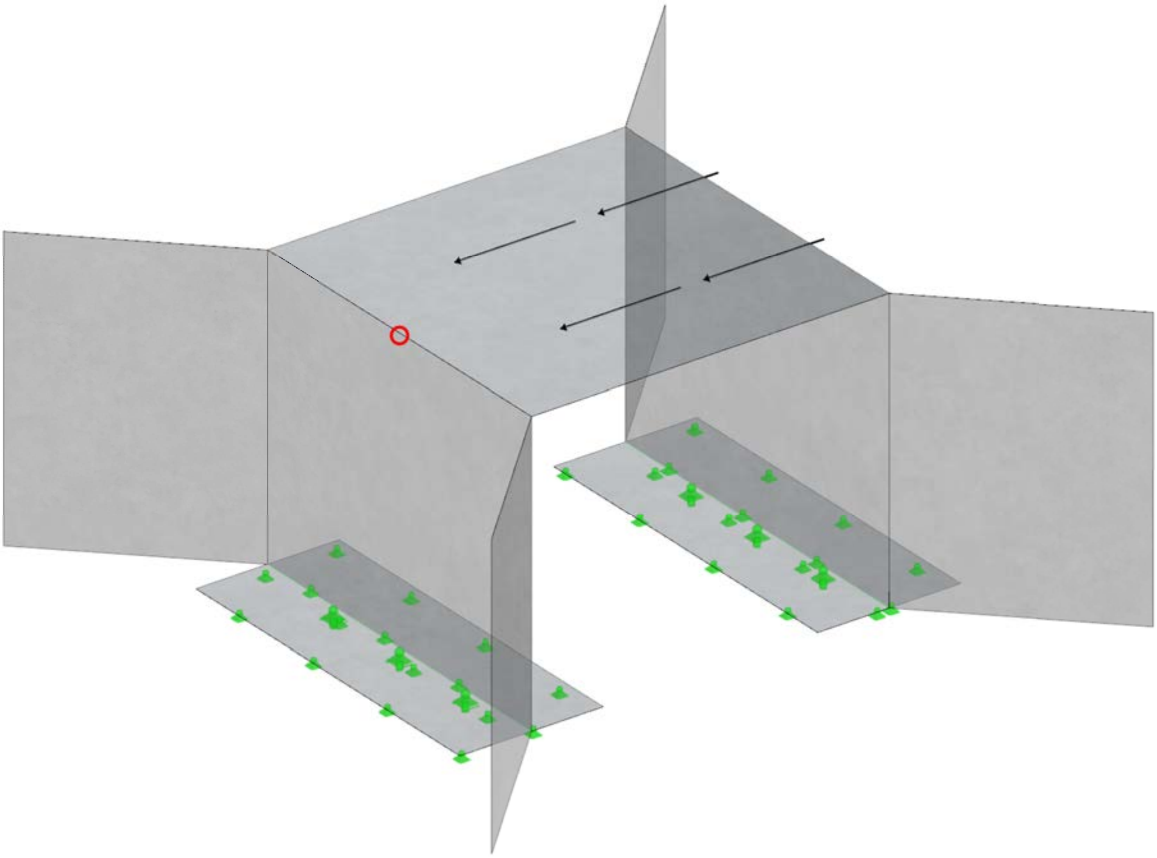

Figure 3.12: Red dot indicated node where values where taken during the mesh convergence study.

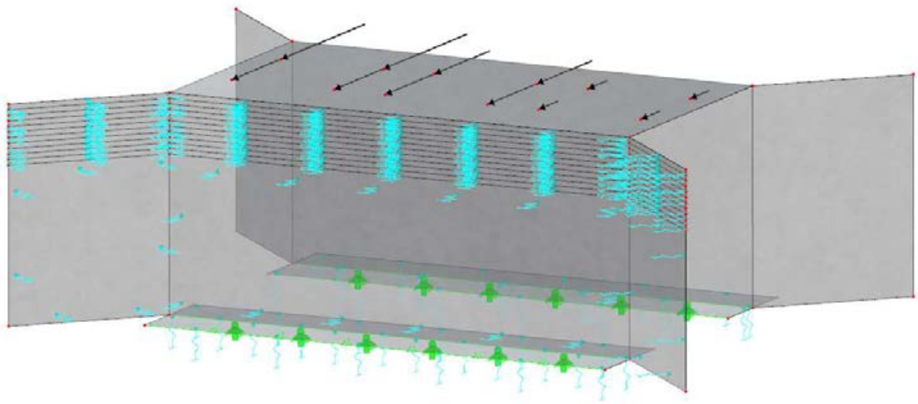

Figure 3.13: Shows the failure simulation model.

3.2.2 Passive earth pressure

Since the passive earth pressure is not to be exceeded it was derived using reasonable values between the mean value and the highest value presented in table A.2 in Appendix A.2. This passive earth pressure is kept constant, using a soil unit weight of 20 kN/m^3, a passive earth pressure coefficient of 5.0 and a resting earth pressure coefficient of 0.3. Calculations are presented in Appendix A.2.

This was only applied to a few Bridge designs through non linear springs that deactivate once the contact stresses exceed the passive earth pressure presented in appendix A.3. The setup is presented in figure 3.13 which illustrates the various surface elements with a height of 0.1 meters down to a depth of 1 meter as seen in figure 3.13. Each surface has springs with an individual yield stress linked to the passive earth pressure.

3.3 Parametric study

As mentioned in chapter 3.1.1, the parameters were studied by changing the size of one parameter whilst keeping the others constant, this is shown in chapter 3.3.2. The results were taken from the result-section function in RFEM as depicted in figure 3.14. For the result-sections Horizontal top and Horizontal bottom the deflection u_z according to the axis seen in figure 3.15.

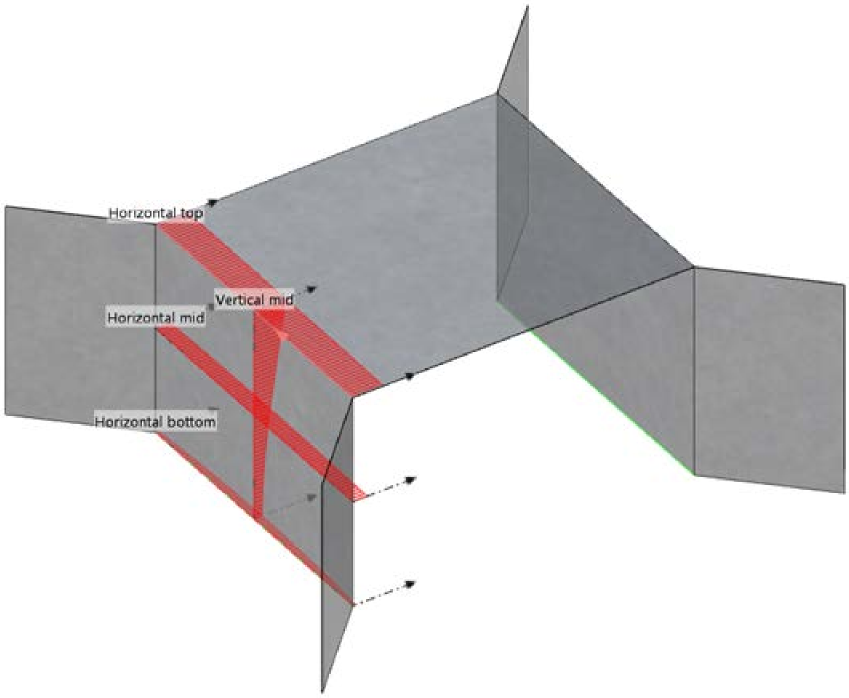

Figure 3.14: The result sections placed on the abutment wall.

For the result section line Vertical mid also called result-section 2, sectional forces m_y, and v_y were extracted, as well as the contact forces along the height of the abutment wall according to the local axis seen in figure 3.15. From the result section line Horizontal mid, also called result-section 1 sectional forces m_x, v_x and v_y were derived from the local axis.

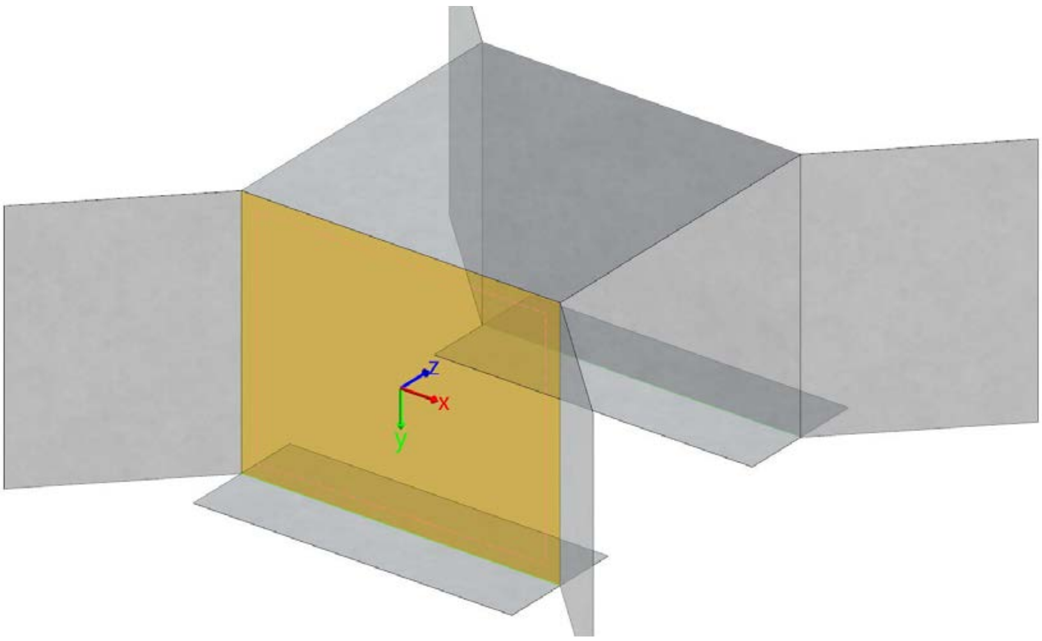

Figure 3.15: Depiction of the local axis for the abutment wall surface. Red colour represents the x-axis, green colour represents the y-axis and blue colour represents the z-axis.

In total eight different bridge types were analysed with three designs for each type of bridge. One should note that some of the different bridge types does not reflect realistic dimensions for a real-life bridge. Certain dimensions might be too large or too small to realistically be constructed as a portal-frame bridge. However, this was done to obtain a broader understanding of how a parameter influenced the section forces and displacements of the different bridge types. For all the models studied, the coordinate system seen in figure 3.15 was used.

Worth noting is that the moments m_x, m_y were oriented according to figure 2.13 in chapter 2.6.2 since the model consisted of surfaces.

3.3.1 Load entities

The bridge was analysed for characteristic load combination and only considered horizontal loads from braking and applied according to chapter 2.5. The values for the loads were determined in Appendix A.3.

3.3.2 Bridge Design

For the various bridge designs the following parameters presented in figure 3.16 below are varied, the thickness t of the abutment wall was also varied in one of the bridge designs. For Bridge design 1-3, 4-3 and 7-1 presented in tables below the soil failure criteria were analysed.

Figure 3.16, depicts the variable parameters and table 3.1-3.8 presents the different parameters used for the different models.

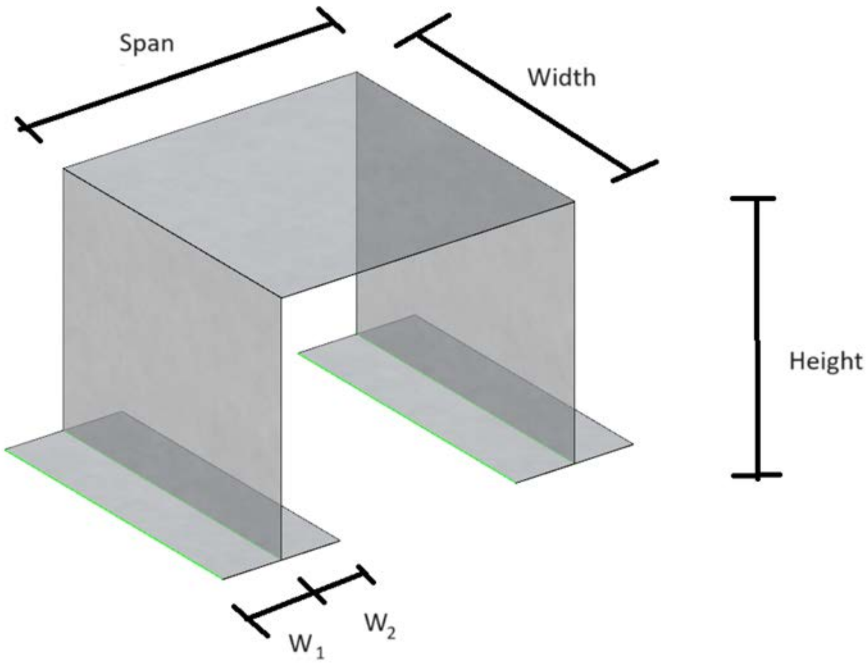

Figure 3.16: Location of the parameters varied.

Table 3.1: Bridge 1 parameters, blue column indicates variable of interest.

Bridge 1					
Type	**Span [m]**	**Width [m]**	**Height [m]**	**W1 [m]**	**W2 [m]**
Bridge 1-1	5	5	4	1	1
Bridge 1-3	5	9	4	1	1
Bridge 1-5	5	14	4	1	1

Table 3.2: Bridge 2 parameters, blue coloumn indicates variable of interest.

Bridge 2					
Type	**Span [m]**	**Width [m]**	**Height**	**W1 [m]**	**W2 [m]**
Bridge 2-1	5	7	6	1	2
Bridge 2-3	15	7	6	1	2
Bridge 2-5	25	7	6	1	2

Table 3.3: Bridge 2.2 parameters, blue coloumn indicates variable of interest.

Bridge 2.2					
Type	**Span [m]**	**Width [m]**	**Height**	**W1 [m]**	**W2 [m]**
Bridge 2-2-1	5	7	4	1	2
Bridge 2-2-3	15	7	4	1	2
Bridge 2-2-5	25	7	4	1	2

Table 3.4: Bridge 3 parameters, blue coloumn indicates variable of interest.

Bridge 3					
Type	**Span [m]**	**Width [m]**	**Height**	**W1 [m]**	**W2 [m]**
Bridge 3-1	8	7	5	1	1
Bridge 3-3	8	7	5	1	2.5
Bridge 3-5	8	7	5	0	4

Table 3.5: Bridge 4 parameters, blue coloumn indicates variable of interest.

Bridge 4					
Type	**Span [m]**	**Width [m]**	**Height [m]**	**W1 [m]**	**W2 [m]**
Bridge 4-1	5	7	4	1	1
Bridge 4-3	5	7	6	1	1
Bridge 4-5	5	7	8	1	1

Table 3.6: Bridge 5 parameters, blue coloumn indicates variable of interest.

Bridge 5						
Type	**Span[m]**	**Width [m]**	**Height**	**W1 [m]**	**W2 [m]**	**Abutment,** t **[m]**
Bridge 5-1	5	5	4	1	1	0.5
Bridge 5-3	5	5	4	1	1	0.65
Bridge 5-5	5	5	4	1	1	0.8

Table 3.7: Bridge 6 parameters, blue coloumn indicates variable of interest.

Bridge 6						
Type	**Span [m]**	**Width [m]**	**Height [m]**	**W1**	**W2 [m]**	**E2 [MPa]**
Bridge 6-1	5	5	4	1	1	50
Bridge 6-3	5	5	4	1	1	100
Bridge 6-5	5	5	4	1	1	150

Table 3.8: Bridge 7 parameters, blue coloumn indicates variable of interest.

Bridge 7						
Type	**Span [m]**	**Width [m]**	**Height [m]**	**W1**	**W2 [m]**	**E1 [MPa]**
Bridge 7-1	5	5	4	1	1	20
Bridge 7-3	5	5	4	1	1	50
Bridge 7-5	5	5	4	1	1	80

4 Results

After concluding the parametric study of the bridges, the results were plotted, and the comparative analysis of the intricate interplay between the manipulated parameters and their resultant effects on deformation and sectional forces was carried out. By varying key geometric variables, and the loading conditions according to the Eurocode, the following results aimed to discern patterns, similarities, and discrepancies across the bridge designs. The iteration process for the STA models and the results from the deformations of the STA translational models are also presented in this chapter.

Ultimately, this chapter contributes to the broader understanding of bridge engineering principles and provides valuable insights for the discussion. Key plots from the deformation in the slab and contact stresses between the soil and abutment wall have been presented in this result section, however all plots of section forces from the bridge designs are shown in Appendix 2.6.2.

The initial results presented in chapter 4.1 to chapter 4.8, are for Bridge 1 through 7 and do not account for soil plasticity, while chapter 4.9 will introduce the results from bridge design 1-3, 4-3 and 7-1 with springs incorporated to account for soil plasticity.

4.1 Bridge design 1, varying width

For Bridge design 1 the width of the bridge varied while the other geometric variables where kept constant. This was a deliberate choice since altering the width does not affect the magnitude of the braking loads. Instead, this only accommodates more notional lanes according to the Eurocode. However, adding more lanes does not linearly increase the magnitude of the overall load due to the adjustment factor reducing the loads of the additional lane. Increase of width will also allow for more soil structure interaction between the abutment wall and soil.

In appendix A.9.1, The sectional forces and the top deformation can be found for Bridge design 1. The horizontal deformations in the slab are presented in figures 4.1-4.3. The results of Bridge 1 indicate that varying the width of the abutment wall does not affect the overall maximum deformations in the horizontal axis. It does change the appearance of the plot with a peak deformation that strays from the centre of the structure towards the edge as the width increases. The deformation between the models varies, the brigade methods converge with each other while overall the methods have similar magnitude of distribution between them.

Figure 4.1: Deformations in the bottom slab for Bridge 1-1, 5 meters width.

Figure 4.2: Deformations in the bottom slab for Bridge 1-3, 9 meters width.

Figure 4.3: Deformations in the bottom slab for Bridge 1-5, 14 meters width.

The contact stresses on the abutment wall due to the earth pressure are presented in figures 4.4-4.6. All the spring bed modules give approximately the same distribution curve with a maximum value by the surface but behave like converging pairs. The Winkler and Pasternak model have a greater slope in all different cases than the Brigade models. The STA model has maximum contact stress in the middle of the abutment wall and much lower magnitude overall compared to the rest.

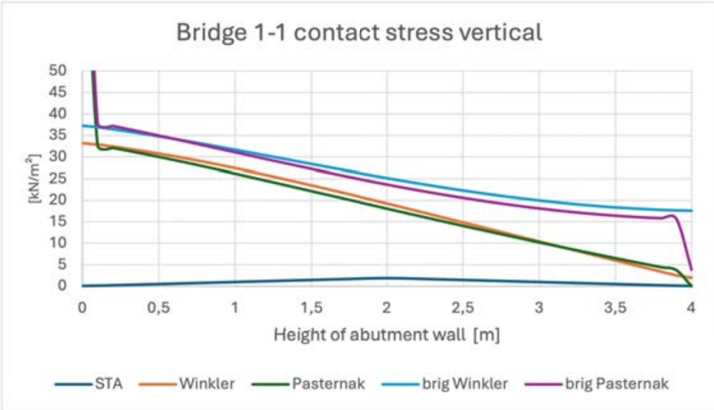

Figure 4.4: Contact stress on the abutment wall, Bridge 1-1, 4 meters height.

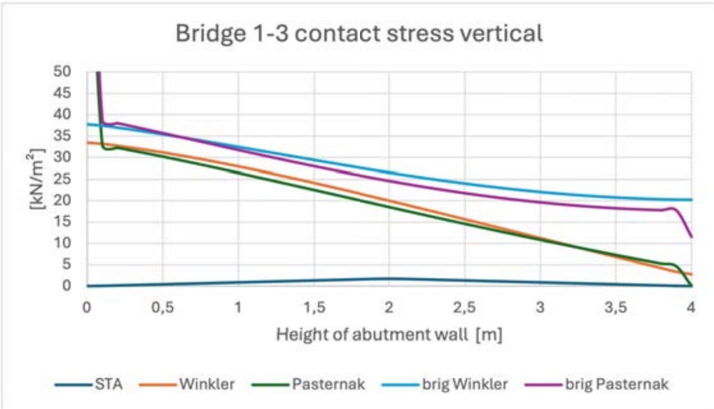

Figure 4.5: Contact stress on the abutment wall, Bridge 1-3, 4 meters height.

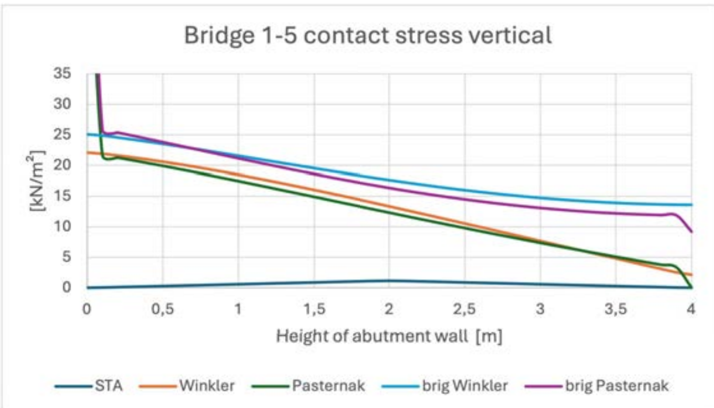

Figure 4.6: Contact stress on the abutment wall, Bridge 1-5, 4 meters height.

4.1.1 Sectional forces and deformations for Bridge 1, varying width

When studying the deformation at the top of the abutment wall, as seen in Appendix **??**, all the models show negative deformations. The STA models give the lowest deformation values, while the Brigade models give the highest. As the width increases, the deformations become less consistent and exhibit more variation due to the implementation of additional notional lanes resulting from the increased width.

The sectional forces for Bridge 1 are presented in Appendix A.9.1. Horizontal result section in the middle, show that the symmetry of the moment M_x around the y-axis creates large negative moment in the edges of the structure. The Brigade methods, unlike the regular Winkler and Pasternak methods, have positive moments in the centre of the structure when the width of the structure is large. Worth noting is that STA method has positive moments in the mid-horizontal result section throughout the design.

The shape of the deformation curves at the top (Appendix figures A.33-A.35) and bottom of the abutment wall for Bridges 1-3 and 1-5 does not resemble those of other bridge designs. This difference is due to the applied braking load (see Chapter 2.5, Loads) on the bridge deck, where more notional lanes are added as the width increases. According to SS-EN 1991-2, 4.4.1, the braking load is not equivalent for all lanes, resulting in slightly higher deformation for all models where notional lane 1 is located, with decreasing deformations for lanes 2 and 3. In some parts of the bridge deck in bridge model 1-5, there are no notional lanes (see Appendix A.8.1 Bridge 1), leading to the observed deviation in deformation for Bridges 1-3 and 1-5.

Result-section 2 presented in Appendix A.9.1 indicate that the largest moments M_y around the x-axis diminishes with an increase in width. All the methods have the designing moments in the same location, largest negative moment at the surface and largest positive moment by the foundation slab. As the width increases the moment converges to zero for Pasternak and Winkler method. For the brigade methods they induce smaller negative moments compared to the other bed module methods, however the positive moments by the foundation slab are larger.

For the shear forces shown in appendix A.9.1 the magnitude of the shear force exhibited in the STI method is constant from the surface to the base of the structure. Spring methods show similar traits to each other, having maximum shear force by the surface that converge to zero at the base of the slab as the width of the abutment wall increases.

4.2 Bridge design 2, varying span

For Bridge Design 2, the focus turned towards varying the span while keeping the other geometric parameters constant. This adjustment isolated the influence of span length on deformations and sectional forces on the abutment wall. Longer spans increase the load linearly due to the braking loads being a function of the span. Keeping the width and height of the abutment wall constant allows for the soil structure interaction to be examined with varying load magnitudes.

In appendix A.9.2, The sectional forces and the deformation at the surface of the abutment wall can be found for Bridge design 2.

The deformations from the bridge design are presented below which indicate that inwards horizontal movement occurs and the magnitude of this phenomena increases with the span, The distribution of the deformation is similar between the methods. Slight flattening occurs of the deformation curve when the span increases, which could be indicative of the load moving further away and facilitating stress distribution in the bridge deck prior to the load transfer to the abutment wall.

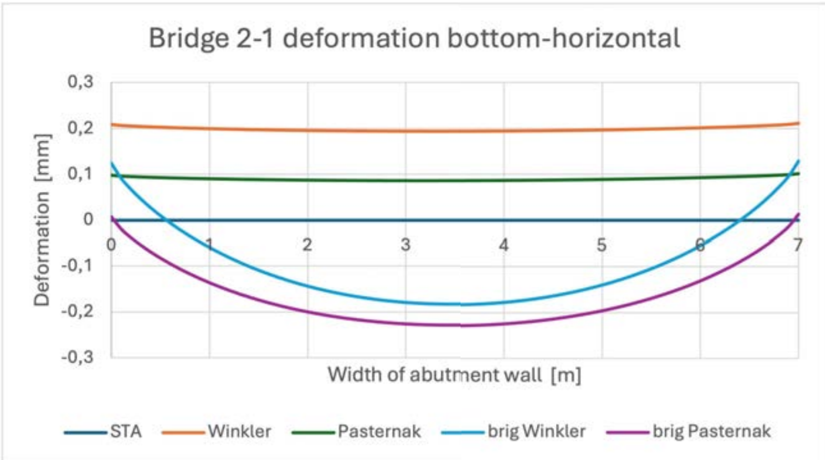

Figure 4.7: Deformations in the bottom slab for Bridge 2-1, span of 5 meters.

Figure 4.8: Deformations in the bottom slab for Bridge 2-3, span of 15 meters.

Figure 4.9: Deformations in the bottom slab for Bridge 2-5, span of 25 meters.

The contact stress for all spring models behave similarly with a maximum value at the surface and a minimum value at the base of the structure. With an increase in span the brigade methods converge with the regular Winkler and Pasternak methods. The STA model indicates little change of contact stress between the various designs, showing completely different behavior compared to the spring methods, until a depth of 3 meters has been reached.

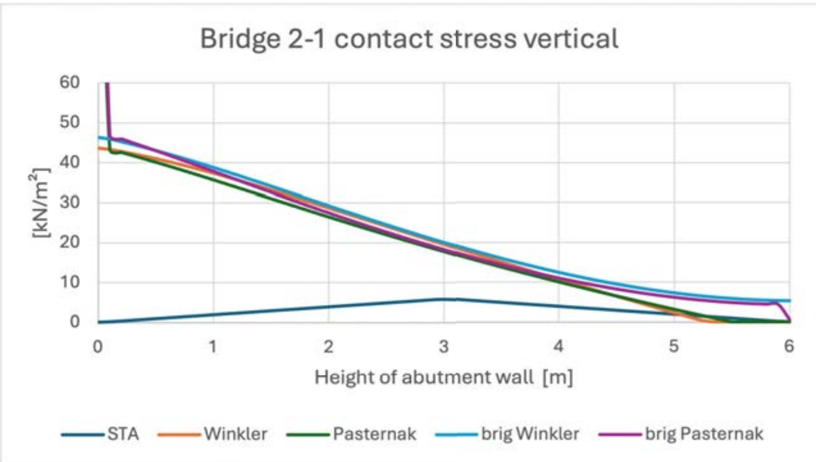

Figure 4.10: Contact stress on the abutment wall, Bridge 2-1, span of 5 meters.

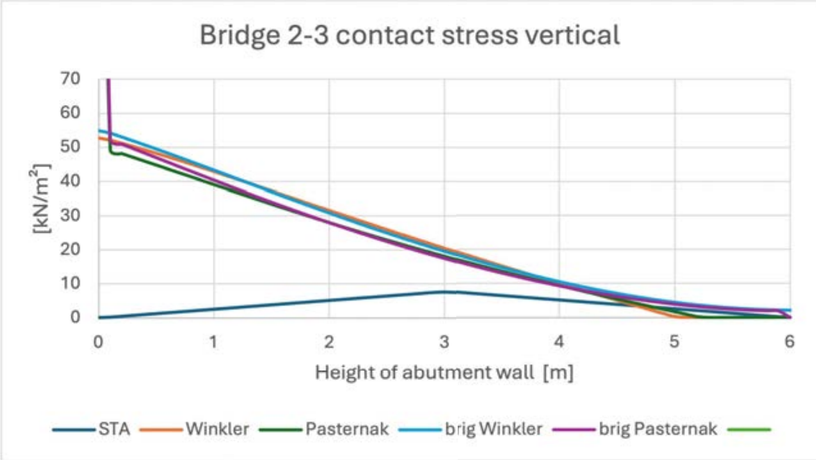

Figure 4.11: Contact stress on the abutment wall, Bridge 2-3, span of 15 meters.

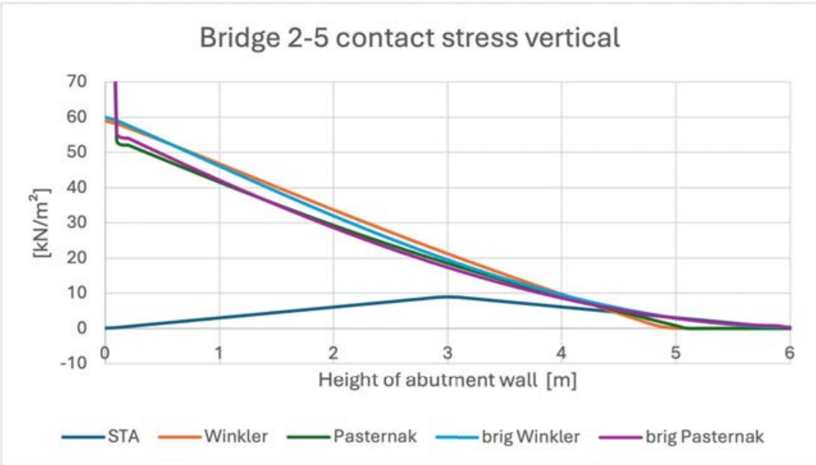

Figure 4.12: Contact stress on the abutment wall, Bridge 2-5, span of 25 meters.

4.2.1 Sectional forces and deformations for Bridge 2, varying span

The sectional forces for Bridge 2, are presented in Appendix A.9.2.

When studying the deformations at the surface of the abutment wall for all the Bridge 2 models seen in A.9.2. The result from Bridge 2 showed that the STA model was particularly sensitive to increased span length for the deformations at the top of the abutment wall, meaning larger deformations compared to the spring models. This is due to the nature of the STA model having no contact stresses at the surface. The other models show approximately the same deformation despite the increase of span length.

The Moment in horizontal section 1 in Appendix A.9.2 show that all the models have a similar shape of the moment distribution, but the STA model always gives a positive moment around y-axis. The other models show similar shape of the moments compared to the STA model but shifted in the negative direction. Creating negative rotation at the edge of the abutment wall and positive in the center of the wall. The increased span length increases the maximum positive moment for all models but have an immense impact on the STA model which shows a much larger positive moment compared to the rest.

The shear forces for horizontal section 1 are presented in A.9.2. The shear force in x-directions resulted in Winkler and Pasternak correlating with the STA models while the brigade methods show much larger sectional shear forces. However, as the span length increases the STA model gradually aligns with the shape of the brigade model. For the shear force in y-direction, the models have similar distribution except for STA which gives larger shear force distribution compared to the rest.

Moment M_y around the x-axis in vertical section 2 in A.9.2, shows that the STA model does not follow the same distribution as the rest of the models. The STA model gives an almost linear distribution with higher maximum values compared to the other models. Moreover, the brigade models have similar distribution with each other, same goes for the Winkler and Pasternak models. All the spring models have approximately the same negative moment but the Brigade models give a higher positive moment at the bottom of the abutment wall compared to the Pasternak and Winkler models.

The shear force V_y in vertical section 2 are presented A.9.2. The spring models have similar distribution with largest shear forces at the top of the abutment wall, and slopes down to approximate zero at the bottom. The brigade models give slightly higher values than the Winkler and Pasternak model at the bottom. The STA models distribution stands out as an outlier, having almost constant force throughout the height of the wall, with a small drop at the end. Compared to the spring models, STA gives much higher shear force values compared to the spring models, except for the initial meter down from the surface.

4.3 Bridge design 2-2, varying span

Bridge 2.2 is a subcategory of Bridge 2, with similar focus towards varying the span, however the height of the abutment wall is reduced for more in depth analysis of the behaviour of the bridge.

The deformation from Bridge 2.2 are presented below which indicate that inwards horizontal movement occurs in the Winkler and Pasternak model as the span increases from the first design that shows outwards horizontal movement for all methods. The phenomena increases with the span, showing a shift towards positive inwards movement as the span increases. This is due to the bridge deck becoming slimmer with increased span, allowing rotation to occur due to the earth pressure. This indicates that not only does the stiffness of the abutment wall affect the deformations, but also the stiffness of the bridge deck. In practical scenarios, cracking at the joint between the abutment wall and the bridge deck can occur, which would compromise the rotational stiffness of the joint – leading to different movement. The distribution of the deformation is similar between the methods. In appendix A.9.3, The sectional forces and the top deformation can be found for Bridge design 2-2.

When the direction of the deformation flips from negative to positive the Winkler method is affected the most which can be seen in figure 4.13 where it has lower deformation than Pasternak, compared to figure 4.14 where the Winkler model has larger positive deformation compared to Pasternak. figure 4.15 of Bridge design 2-2-5 shows an amplified version of Bridge design 2-2-3 due to the increase in span.

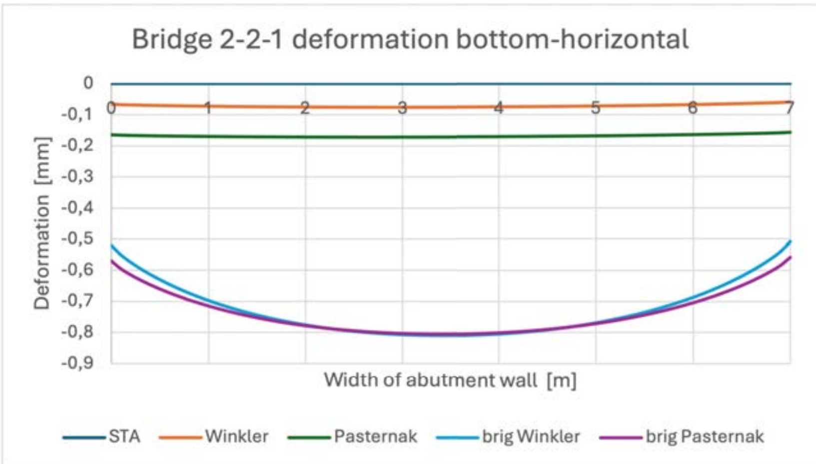

Figure 4.13: Deformations in the bottom slab for Bridge 2-2-1, span of 5 meters.

Figure 4.14: Deformations in the bottom slab for Bridge 2-2-3, span of 15 meters.

Figure 4.15: Deformations in the bottom slab for Bridge 2-2-5, span of 25 meters.

The contact stress presented in figure 4.16-4.18 for Bridge 2-2 shows that the STA follows a triangular shape with an small increase in its peak middle value when the span length increases. The Winkler and Pasternak models have a similar distribution with large initial contact stresses at the surface of the structure that linearly decrease and converges with zero at the base of the foundation slab. For the Brigade models exhibit the largest contact stresses, they behave similarly to the Winkler and Pasternak models with linear drop-off with an increase in depth. However, the Brigade models give higher contact stress at the bottom of the abutment wall compared to the other models.

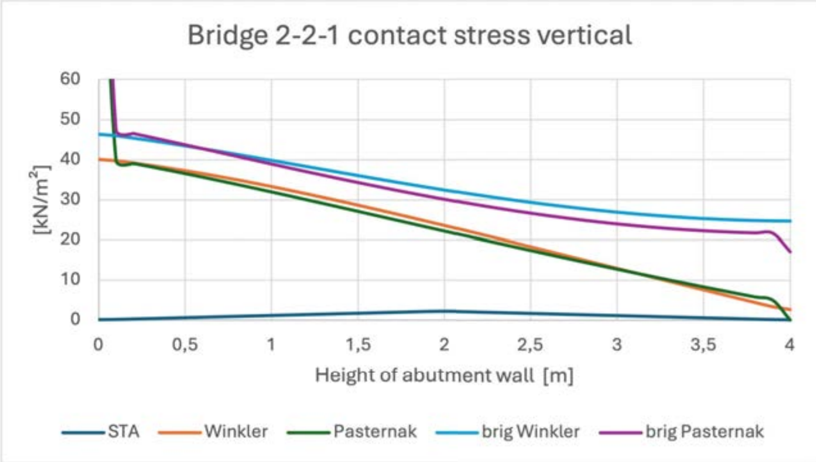

Figure 4.16: Contact stress on the abutment wall, Bridge 2-2-1, height of 4 meters and span of 5 meters.

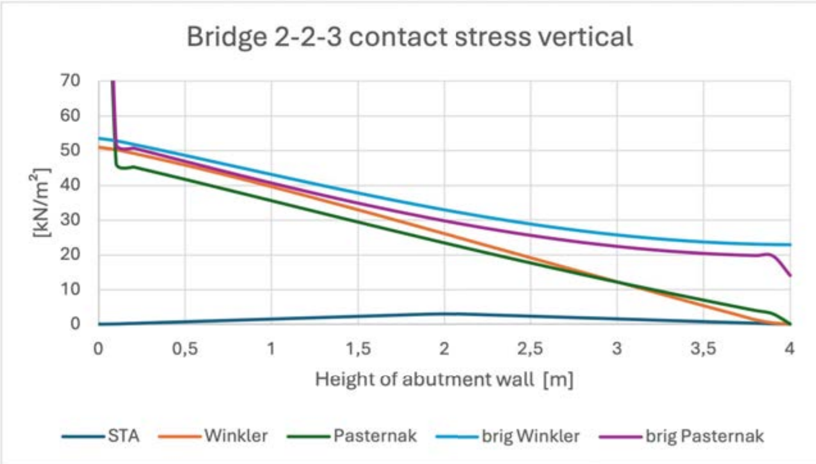

Figure 4.17: Contact stress on the abutment wall, Bridge 2-2-3, height of 4 meters and span of 15 meters.

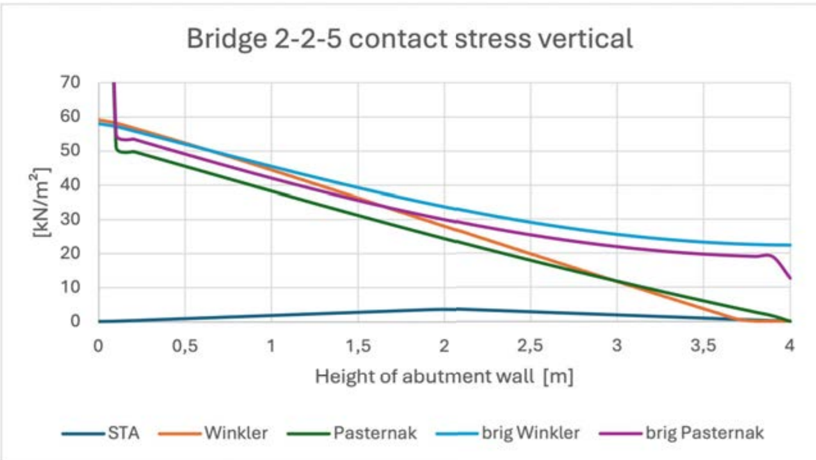

Figure 4.18: Contact stress on the abutment wall, Bridge 2-2-5, height of 4 meters and span of 25 meters.

4.3.1 Sectional forces and deformations for Bridge 2-2, with varying span

The sectional forces for Bridge 2-2, are presented in Appendix A.9.3.

The deformation in the top of the abutment wall increases when the span length increases, with the STA model showing the lowest deformation. The Winkler models deformation increases the most giving it the highest deformation of them all when the span has the largest length. The rest of the models have approximately the same distribution throughout Bridge 2-2.

When studying the moment, M_x distribution of the horizontal section 1 around the y-axis, all the models have similar distribution shape (arch shape) except for the STA. The STA model only gives positive oriented moments whilst the other models give negative oriented moments at the edges but positive moments in the middle. The Winkler model has negative M_x moments throughout the design, Pasternak is similar but has slight shifted arch shape causing positive moments in bridge design 2.2.5 for the center of the wall.

The shear forces for horizontal section 1, are presented in Appendix A.9.3. The shear forces in x-direction for Bridge 2-2-1 resulted in Winkler and Pasternak showing mirrored forces compared to Brigade and STA model. However, with an increase of the span the models converge and show the same force direction but with varying magnitude. Brigade showing consistently larger forces throughout the design. For shear forces in the y-direction the methods have converging pairs. The STA model shows largest forces with a steep slope in the edges of the abutment wall towards the wing-walls, Winkler and Pasternak share the behaviour but with a lower amplitude.

The moments, M_y around the x-axis for the vertical section 2 showed that the Brigade models and Winkler/Pasternak models behave as converging pairs initially. However, when the span length increases all the spring models converge to the same distribution. The STA models remain linear throughout the design.

The shear force V_y in vertical section 2 shows that the spring models have similar distribution (negative linear slope) which correlate when the span length increases. The Brigade models showed the largest positive and negative shear forces throughout the design. The STA model stands out as almost a constant shear force distribution and gives overall much higher shear force values after one meter down from the top of the abutment wall. All the models have very small changes to the shear force values when the span length increases.

4.4 Bridge design 3, varying the foundation slab design

For Bridge Design 3 the foundation slabs were the primary focus, and which was deliberately varied in size to compare two distinct bridge configurations conventional portal frame bridge to a design with a closed cross section. This approach aimed to demonstrate the influence the slab had on the sectional forces in the abutment wall. Since a large slab would be stiffer in regard to translational deformations. Inherently isolating the influence of structural stiffness of the foundation to the sectional forces.

In appendix A.9.4, The sectional forces and the top deformation can be found for Bridge design 3.

The deformation for Bridge 3 is presented below in figures 4.19-4.21. The main focus is between Bridge design 3-1 and 3-5. Bridge 3-5 has a fully closed cross section as seen in Appendix A.29. The results from Bridge 3-5 indicates that rigid body motion occurs since the rotation that appears to happen in the Winkler method for Bridge 3-1 and 3-3 that causes horizontal inwards motion does not appear in a closed cross section. There is minimal change to the Brigade methods.

Figure 4.19: Deformations in the bottom slab for Bridge 3-1, $W1$ and $W2$ is 1 meters.

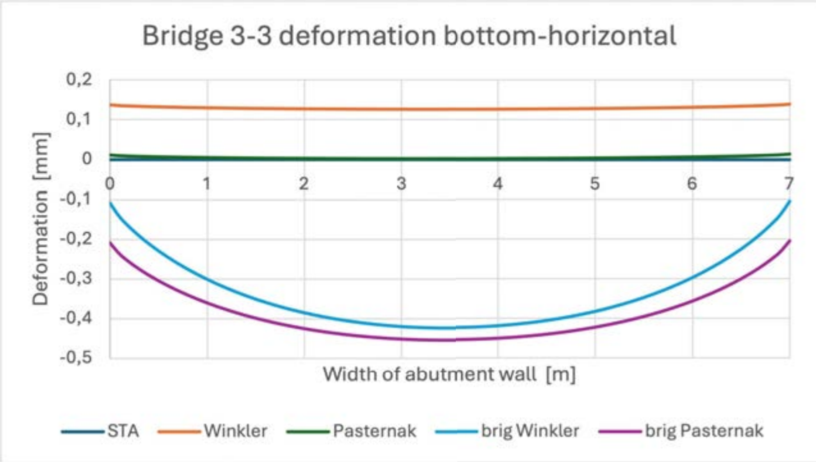

Figure 4.20: Deformations in the bottom slab for Bridge 3-3, $W1$ is 1 meter and $W2$ is 2.5 meters.

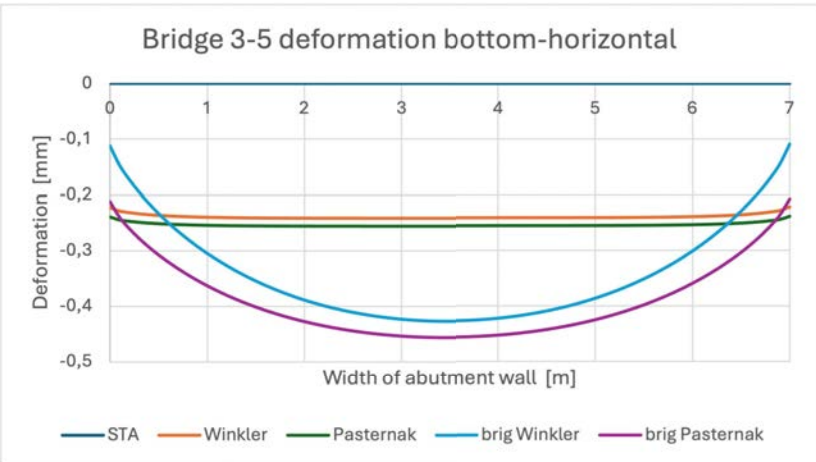

Figure 4.21: Deformations in the bottom slab for Bridge 3-5, this design is the closed cross section.

When the Bridge varies from an open to a closed cross-section as in Bridge 3, the structural movement acts more as a rigid body motion. This can be seen for the Winkler and Pasternak models at the deformation in the bottom pushing the entire structure against the backfill soil (Bridge 3-5). When modelling with the Brigade models this phenomenon does not occur as the slab was replaced with rotational stiffness springs. As the same for the STA model because it does not allow for movement in the bottom of the slab

For Bridge 3, the contact stresses in figure 4.22-4.24 from the different models have similar distributions, except for the STA model. However, when the slab resembles more a closed cross section the spring models begin to diverge from each other. Forming converging pairs, the brigade models come together, as do the standard Winkler and Pasternak models. Whilst the STA model maintains identical distribution for all graphs.

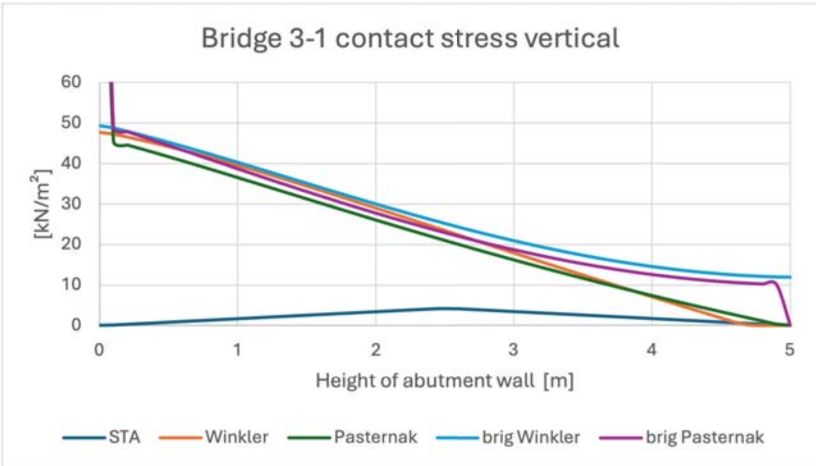

Figure 4.22: Contact stress on the abutment wall Bridge 3-1, $W1$ and $W2$ is 1 meters.

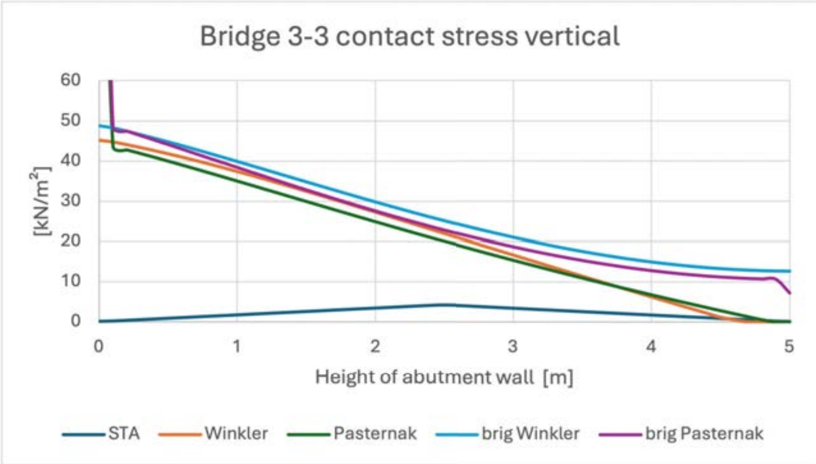

Figure 4.23: Contact stress on the abutment wall Bridge 3-3, $W1$ is 1 meter and $W2$ is 2.5 meters.

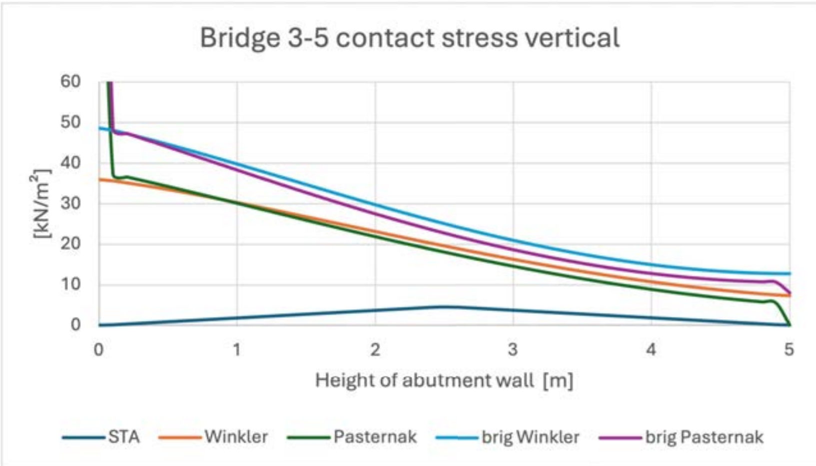

Figure 4.24: Contact stress on the abutment wall, Bridge 3-5, this design is the closed cross section.

4.4.1 Sectional forces and deformations for Bridge 3, varying the foundation slab design

The deformation at the top of the abutment wall in A.9.4, shows that all the models have approximately the same deformation, however when the slab becomes a closed cross section the Winkler and the Pasternak models show less deformation compared to the STA and Brigade models.

The moment distribution for M_x A.9.4 for horizontal section 1, show that all the spring models have similar distributions. The spring models converge when the cross section is closed. The STA model differs from the other models in a way that it only has positive moments. Whilst the spring models have both positive moment in the middle of the abutment wall and negative at the edges. When the cross section is closed the maximum positive moment of the STA model has approximately the same value as the maximum positive moment for the Winkler and Pasternak model.

The shear force V_x A.9.4 for horizontal result section in the middle, resulted in all the models having similar distributions. But the Brigade models always give a higher maximum shear force at the edges of the abutment wall compared to the other models. However, in the middle of the abutment wall all the models give roughly the same results. For the shear force V_y A.9.4 in horizontal middle result section, all the models have similar load distribution, but the STA model consistently gives the highest positive shear force in the middle of the abutment wall whilst the negative shear force at the edges are comparable to the Winkler and Pasternak models. The Brigade models have larger positive shear force compared to Winkler and Pasternak, however the Brigade models have almost only positive shear force throughout the distribution. When the cross section is closed the Pasternak and Winkler models maximum positive shear force V_y converge to the Brigade models.

Moment M_y in result-section 2 A.9.4, show that all the spring models have the same curved distribution whilst the STA model has a more linear distribution. When the cross section is closed the spring models converge to each other. The STA models positive and negative moments are always greater than the spring models, not aligning well when the cross-section is closed.

The shear force V_y in the result-section 2 A.9.4, shows all the spring models have a similar distribution slope, however the Brigade models have a steeper slope when the cross section becomes closed compared to Winkler and Pasternak. The STA models show constant shear force regardless of depth giving much larger shear forces after 1 meter depth compared to other models. However, the maximum shear force is obtained from the Brigade models close to the surface (less than 1 meter depth).

4.5 Bridge design 4, varying height

In Bridge Design 4, the height of the structure was the variable and other parameters were constant, this configuration allowed for more translation of contact forces due to the increase in surface area of the abutment wall, moreover it also influences the stiffness of the overall structure allowing for larger deformations. This step aimed to isolate the heights impact on the structures behaviour.

In appendix A.9.5, The sectional forces and the top deformation can be found for Bridge design 4.

The results for deformations in the bottom slab for bridge 4 indicates that the height of the structure impacts the direction of the movement, which can be seen in figure 4.25-4.27. The Winkler method has the smaller deformation compared to Pasternak on movement outwards, however when the height increases and the direction of the movement changes the Winkler method is larger than Pasternak. The brigade models deformation increase in the positive direction at the top and bottom of the abutment wall when the height increases.

Figure 4.25: Deformations in the bottom slab for Bridge 4-1, with a height of 4 meters.

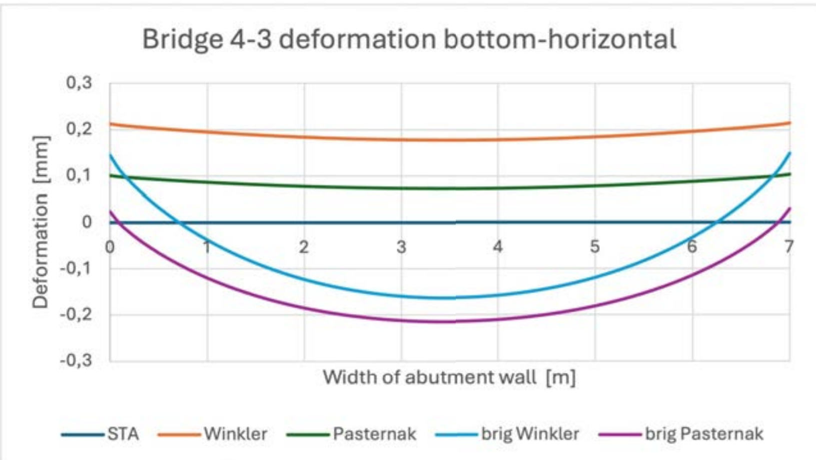

Figure 4.26: Deformations in the bottom slab for Bridge 4-3, with a height of 6 meters.

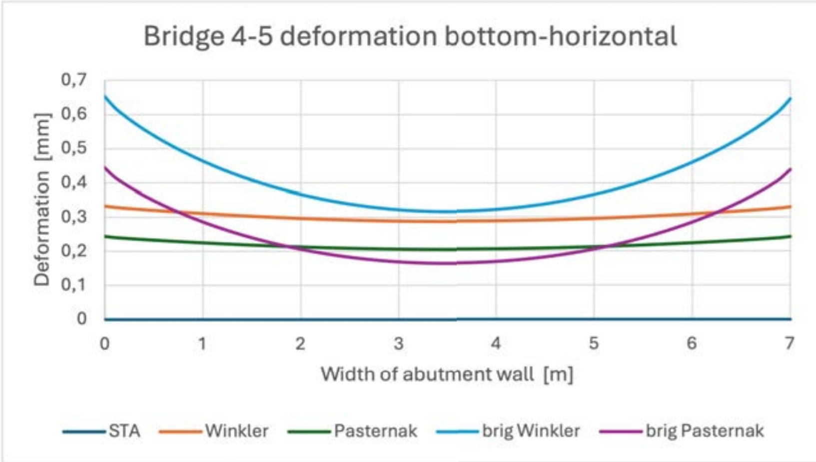

Figure 4.27: Deformations in the bottom slab for Bridge 4-5, with a height of 8 meters.

The contact stress shown for Bridge 4, presented in figure 4.28-4.30 show poor correlation between the spring methods and the STA model. The Spring models have maximum contact force at the surface which steadily decrease with depth, while the STA models have maximum contact force in the middle of the height of the abutment wall. When the height increases the spring models converge with each other, and a phenomena occurs near the slab where the contact force is zero for the spring models before reaching the bottom of the slab.

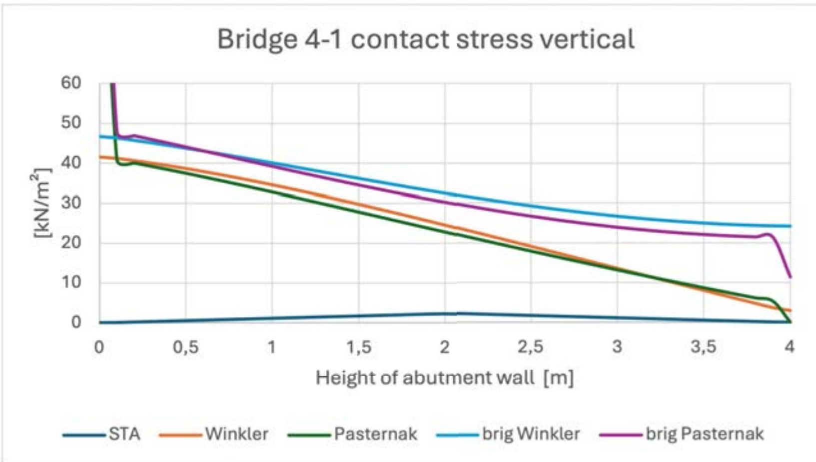

Figure 4.28: Contact stress on the abutment wall, Bridge 4-1, with a height of 4 meters.

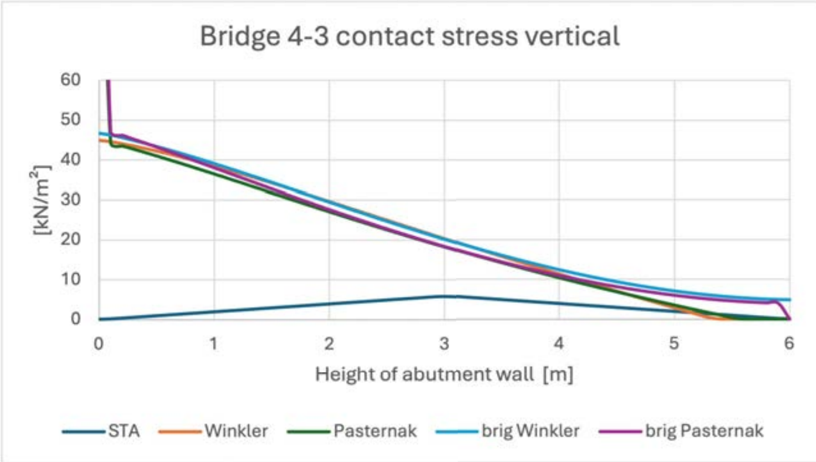

Figure 4.29: Contact stress on the abutment wall, Bridge 4-3, with a height of 6 meters.

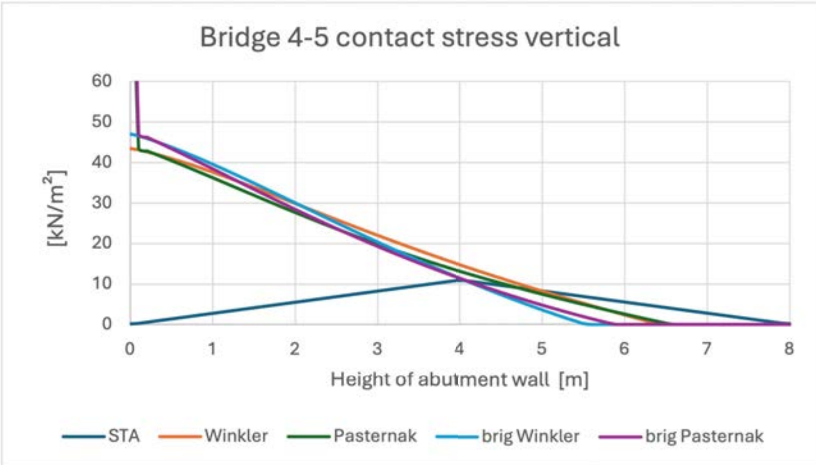

Figure 4.30: Contact stress on the abutment wall, Bridge 4-5, with a height of 8 meters.

4.5.1 Sectional forces and deformations for Bridge 4, varying height

The sectional forces for Bridge 4 are presented in appendix A.9.5. Horizontal result section in the middle show that the moment M_x is affected by the height of the abutment wall. STA shows positive maximum moments in the center of the abutment wall throughout the design. While the other methods converge on each other showing very similar results with maximum negative moments in the edges of the structure.

Shear forces V_x, V_y for the mid-horizontal result section indicate that the results from the all the methods converge with increased height. The outlier being the STA method for shear forces acting in the y-direction showing very large forces while other methods are showing negligible forces.

the vertical result section show similar results to the horizontal result-section where all the spring models converge with each other, and STA is an outlier showing much larger forces. For instance, the moment My acting around the x-axis show that the STA method is linear from the surface down to the slab and is not affected much by the increase in height, while the spring methods converge with each other, and the designing moment converges to zero by the slab as the height increases.

The shear force V_y in the vertical result section has similar traits to the moments. Forces converge to zero in the slab as the height increases in all spring methods, while STA deviates showing lower initial forces by the surface of the abutment wall but consistently higher forces throughout the depth of the structure.

4.6 Bridge design 5, varying the abutment wall thickness

Bridge Design 5 analysed the influence of stiffness to the sectional forces by only varying the thickness of the abutment wall while keeping all geometries constant, this aimed to isolate the impact of the abutment walls stiffness.

In appendix A.9.6, The sectional forces and the top deformation can be found for Bridge design 5.

The deformations for Bridge 5 presented below indicate that the Winkler, Pasternak and STA models all have similar deformations, around zero. The variation of thickness give approximately the same results for all three models, only showing a small negative deformation increase for the Pasternak models. However, both Brigade models give explicitly negative deformations. Which increases with the abutment wall thickness. The wall thickness indicate rigid body motion behaviour appears when the abutment wall gets thicker, all methods exhibit outwards transnational deformations in the stiffest design.

Figure 4.31: Deformations in the bottom slab for Bridge 5-1, with an abutment wall thickness of 0.5 meters.

Figure 4.32: Deformations in the bottom slab for Bridge 5-3, with an abutment wall thickness of 0.65 meters.

Figure 4.33: Deformations in the bottom slab for Bridge 5-5, with an abutment wall thickness of 0.8 meters.

Figure 4.34-4.36 illustrate the distribution of contact stress along the abutment wall. All models exhibit roughly similar stress distribution patterns, except for the STA model. As the thickness of the abutment wall increases, the spring models begin to diverge from each other, forming converging pairs: the brigade models come together, as do the standard Winkler and Pasternak models. However, the distribution in the STA model remains almost unchanged, regardless of the wall thickness.

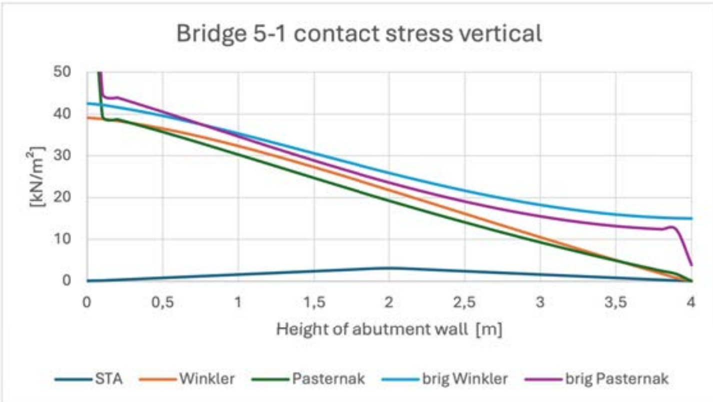

Figure 4.34: Contact stress on the abutment wall, Bridge 5-1 , with an abutment wall thickness of 0.5 meters.

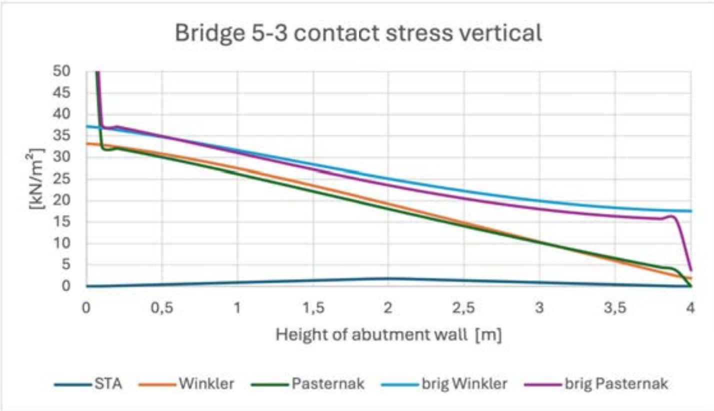

Figure 4.35: Contact stress on the abutment wall, Bridge 5-3, with an abutment wall thickness of 0.65 meters.

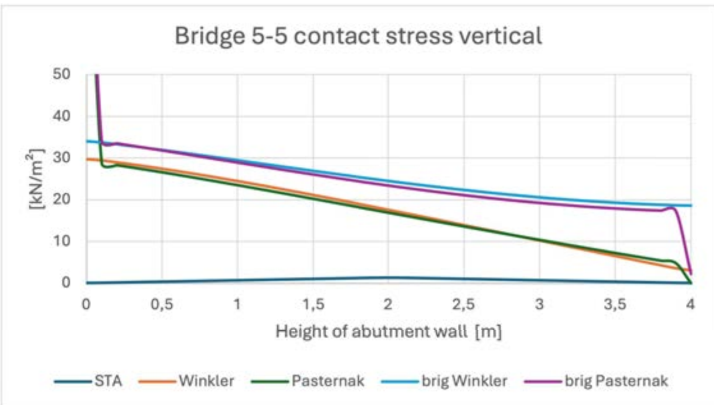

Figure 4.36: Contact stress on the abutment wall, Bridge 5-5, with an abutment wall thickness of 0.8 meters.

4.6.1 Sectional forces and deformations for Bridge 5, varying the abutment wall thickness

The deformation in the top of the abutment wall, showed that with an increased thickness of the abutment wall decreased the deformation for all the models. With the STA models having the smallest deformation while the Brigade models have the highest deformation. The increased thickness of the abutment wall enhances its rigidity, thereby minimising the contrast in deformation between its upper and lower sections. This occurs because the bridge undergoes a greater degree of translational deformation, as opposed to slimmer designs where deformation primarily affects the upper part.

Horizontal result section located in the middle A.9.6 show similar distribution of the moment M_x around the y-axis between the designs. STA being an outlier with positive moment while all the other spring methods show negative moments throughout the design. The shear forces V_x in the horizontal result section indicate that the Winkler and Pasternak method have initially negligible forces which increase in the edges of the abutment wall when the thickness increases. Brigade and STA methods share similar traits in shear forces for V_x, however they do not correlate for shear forces in the y-direction as the thickness increases the divergence of the methods.

Results from the vertical result section indicate that the largest negative moment M_y around the x-axis increase at the surface level for Pasternak and Winkler as the thickness increases while the other methods remain constant throughout the design. But the largest positive moment at the base increases for the brigade and STA methods. Winkler and Pasternak exhibit linear behavior with maximum values at the surface of the abutment wall that decreases with depth.

The shear forces V_y for the vertical result section indicate that the spring methods have larger initial forces but subsequently lowers with the depth, but STA being an outlier and showing consistent elevated forces in all depths of the abutment wall.

4.7 Bridge design 6, varying the soil stiffness against the foundation slab

Bridge 6 was a parameter study of the elastic modulus of the soil beneath the foundation slab to see the impact it would have on the results, while all other parameters were kept constant. The results yielded that the stiffness of the soil below the foundation slab have little to no impact on the results throughout the bridge design. Hence the maximum contact stress and maximum deformations in the foundation slab for Bridge 6 was plotted instead of individual presentations of the bridges seen in figure 4.37 and figure 4.38.

Changing the elastic modulus of the foundation resulted in little change to the deformations and sectional forces in the abutment wall. This is a result of the way the study has been conducted. The foundation soil characteristics do not impact the study since vertical movement is either restricted completely as for the STA, Winkler and Pasternak model, or reduced with stiff springs according to the brigade models. Vertical forces are not included into the models, meaning that the only forces affecting the foundation is a result of the structure rotating into the soil through the foundation slab.

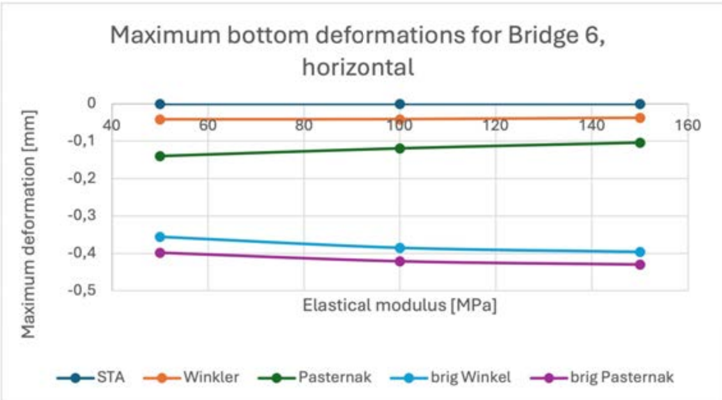

Figure 4.37: Maximum deformation in the bottom slab with varying elastic modulus for Bridge 6.

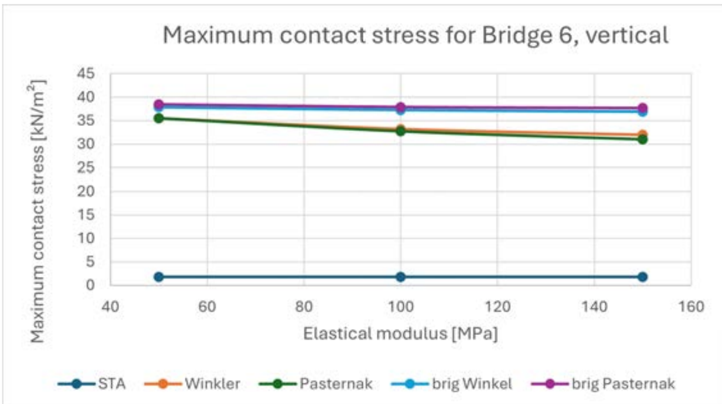

Figure 4.38: Maximum contact stress on the abutment wall with varying elastic modulus for Bridge 6.

4.8 Bridge design 7, varying the soil stiffness against the abutment wall

The elastic modulus for the backfill soil of the abutment wall was varied to see its impact on the different bridge designs. This is motivated by its great influence of the spring stiffness for the springs against the abutment wall and wing walls.

In appendix A.9.7, The sectional forces and the top deformation can be found for Bridge design 7.

As seen in. figures 4.39-4.41, increasing the elastic modulus for the abutment wall backfill has no effect on the STA models. However, for all the spring models it decreases the deformation on the top of the abutment wall when the stiffness increases.

Figure 4.39: Deformations in the bottom slab for Bridge 7-1, Elastic modulus of 20 MPa against the abutment wall.

Figure 4.40: Deformations in the bottom slab for Bridge 7-3, Elastic modulus of 50 MPa against the abutment wall.

Figure 4.41: Deformations in the bottom slab for Bridge 7-5, Elastic modulus of 80 MPa against the abutment wall.

The contact stresses for Bride design 7 are presented in figure 4.42-4.44, the increase in stiffness only effects the spring models. Leading to the contact stress on the abutment wall getting larger when the stiffness increases and the result shows that the Winkler and Pasternak models are more sensitive to this parameter change than the Brigade models.

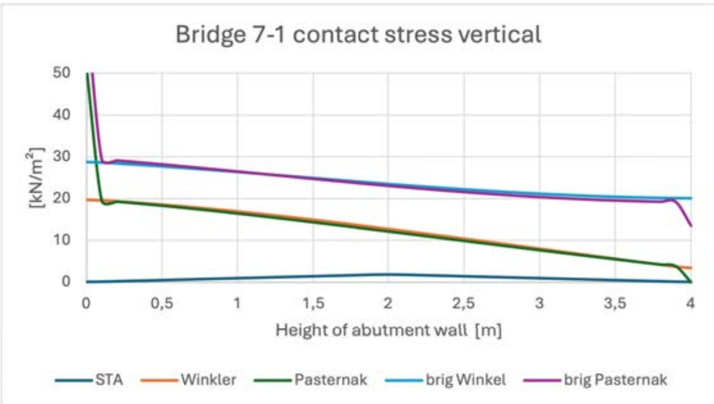

Figure 4.42: Contact stress on the abutment wall, Bridge 7-1, Elastic modulus of 20 MPa against the abutment wall.

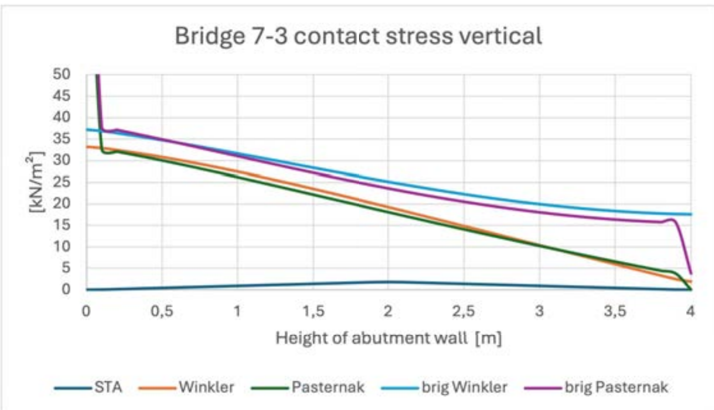

Figure 4.43: Contact stress on the abutment wall, Bridge 7-3, Elastic modulus of 50 MPa against the abutment wall.

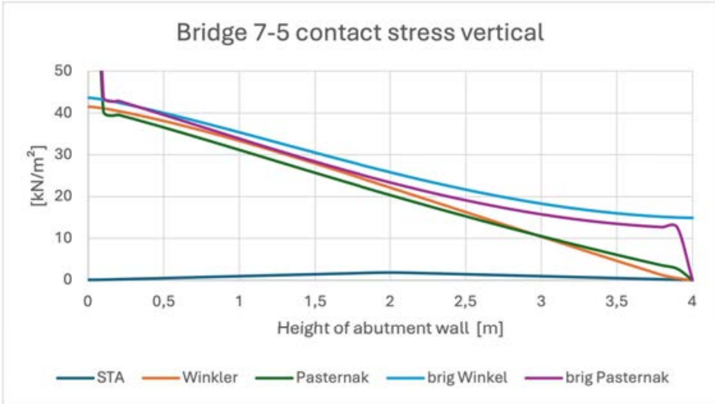

Figure 4.44: Contact stress on the abutment wall, Bridge 7-5, Elastic modulus of 80 MPa against the abutment wall.

Changing the elastic modulus of the soils for the abutment wall proved the results to be sensitive to the change in the soils. As mentioned previously in chapter 4.7, this is a result of the way the study has been conducted. The abutment wall soil holds great importance and impact the sectional forces and deformations through the structure which can be seen in the deformations from figure 4.39-4.41 and the sectional forces presented in Appendix A.9.7.

Decreasing the elastic modulus for the abutment wall increases the sectional forces, and shear forces which normally reduce drastically for spring models with depth are kept high in correlation with the STA model. The increase in sectional forces indicate the structure takes up more of the braking forces as expected.

4.8.1 Sectional forces and deformations for Bridge 7

The sectional forces of the STA model showed no effect when the stiffness was increased.

For the deformation on the bottom of the abutment wall, an increase in soil stiffness for the abutment wall, yielded to a decrease of the deformation for all the spring models. The Brigade models showed to have higher deformation than the Winkler and Pasternak models, throughout the stiffness variation.

The moment M_x for section 1 showed that an increase in soil stiffness , decreased the maximum moment where the shear spring models have the highest maximum negative moment compared to the non-shear spring models.

The shear forces for section 1, V_x and V_y, showed to have no correlation for the different bridge models, however when the stiffness increased the maximum shear force V_y for all the spring models decreased. For V_x the shear force in the middle of the abutment wall showed to correlate more for the spring models with increased soil stiffness in the abutment wall backfill.

The moment M_y for section 2, showed that a lower elasticity model for the backfill made the spring model correlate more to the STA model, especially the Brigade models.

However, when the elasticity model increased the Spring models planed of more leading to the STA model showing the highest positive moment,M_y. But the Winkler and Pasternak models always showed the highest negative moment value.

For section 2, the shear force V_y showed that the shear force increased when the stiffness increased whit all the spring models having similar shear force distribution when the elasticity modulus of the backfill is high, the Winkler and Pasternak models started to correlate more with the Brigade models. The STA model deviate strongly from the spring models.

4.9 Simulations of bridges with failure criteria

Since previous simulations do not account for plasticity in the soil, this chapter will present results from the analysis of non linear springs that yield once the passive earth pressure is exceeded. The analysis was conducted on three different Bridge designs, Bridge 1-3, Bridge 4-3 and Bridge 7-1.

The bottom deformation is presented in figures 4.45-4.47. The deformation in the bottom of the slab for all failure criteria Bridge designs showed no changes from the initial springbed bridge design which did not account for the failure criteria, see previous results for Bridge 1-3, varying the width (figure 4.2), Bridge 4-3, varying the height (figure 4.26), and Bridge 7-1, varying the the elastic modulus of the soil against the abutment wall (figure 4.39).

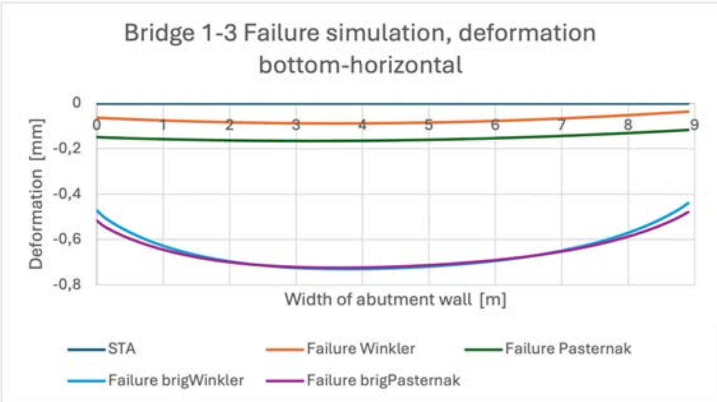

Figure 4.45: Deformations in the bottom slab for Failure simulations, Bridge 1-3.

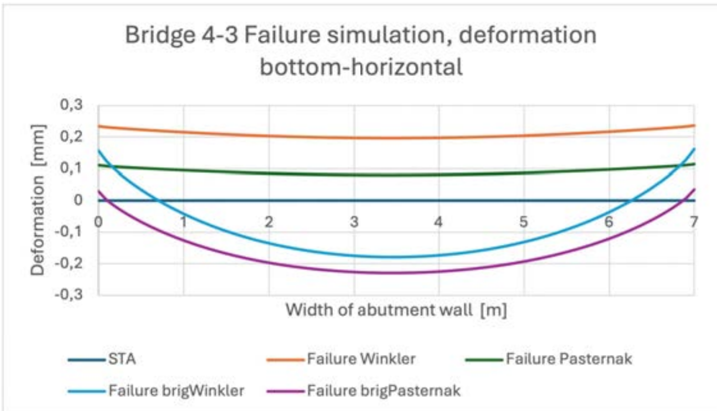

Figure 4.46: Deformations in the bottom slab for Failure simulations, Bridge 4-3.

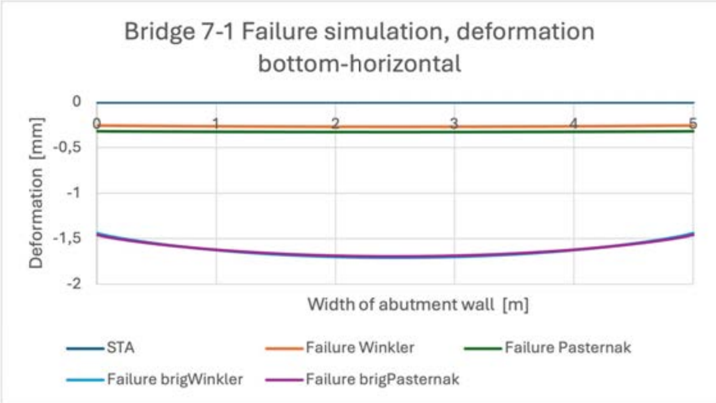

Figure 4.47: Deformations in the bottom slab for Failure simulations, Bridge 7-1.

The contact stress on the abutment wall is presented in figures 4.48-4.50. The Failure criteria models seems to only differ from the corresponding Bridge models, the first 0.5 meters of depth. Afterwards, the contact stresses from the Failure models return to the same values as there corresponding Bridge models. This rapid convergence to the corresponding models bridge 1-3 (figure 4.5), bridge 4-3 (figure 4.29), and bridge 7-1 (figure 4.42) is due to the passive earth pressure increasing quickly with depth.

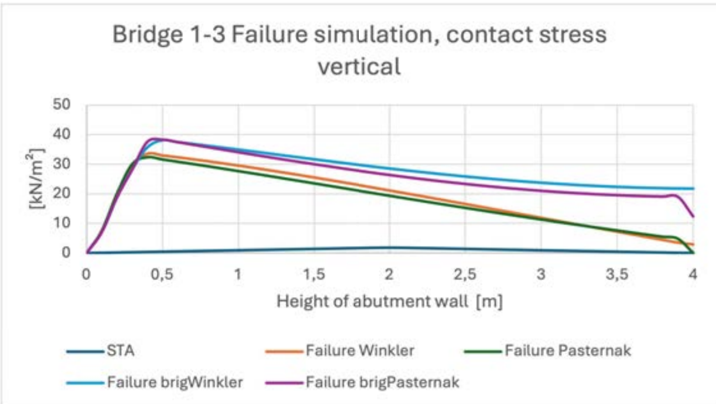

Figure 4.48: Contact stress on the abutment wall, Failure simulations, Bridge 1-3, from the width analysis.

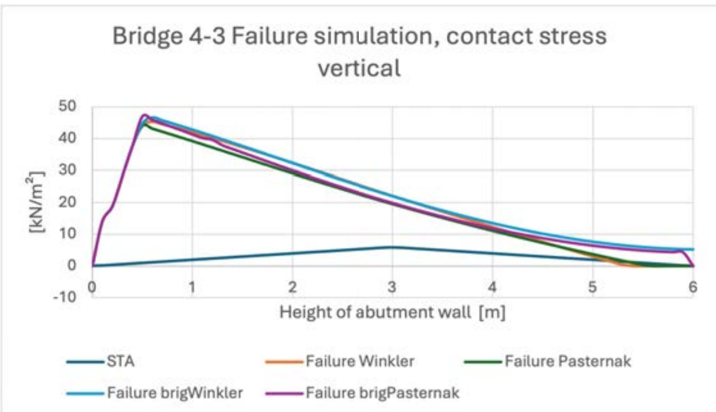

Figure 4.49: Contact stress on the abutment wall, Failure simulations, Bridge 4-3, from the height analysis.

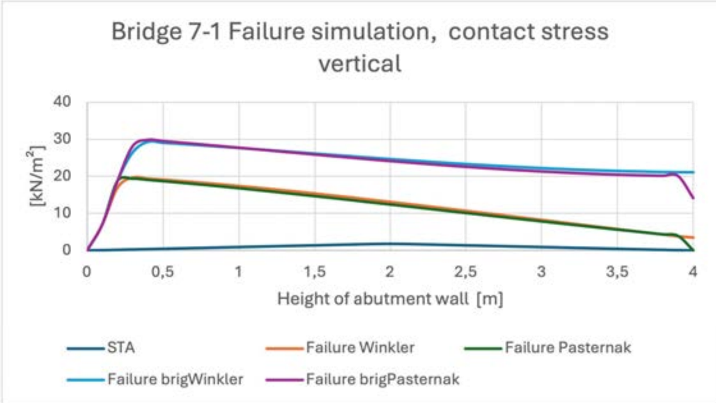

Figure 4.50: Contact stress on the abutment wall, Failure simulations, Bridge 7-1, from the analysis varying the elastic modulus of the soil against the abutment wall

4.9.1 Sectional forces and deformations for failure criteria models

Deformation in the top increases when failure criteria is considered as seen in Appendix A.9.8 figure A.159 - A.161. This is due to the limitation of forces transferred to the soil. seen in the previous corresponding models where the peak of the contact stress is at the surface of the abutment wall. The increase is however, not substantial.

When comparing the sectional forces between initial corresponding models (see appendix A.9.1, A.9.5 and A.9.7) and the failure criteria models (A.9.8), the sectional forces and deformations are nearly identical. Largest difference are the initial moments and shear forces at the surface the abutment wall experiencing slightly elevated values that do not instantly reduce with depth.

4.10 Translational analysis of the STA model

A Translational movement analysis of the foundation slab was deemed necessary since the STA method indicates negligible deformations in the top of the abutment wall during analysis of bridges experiencing rigid body motion, suggesting that the support conditions of the STA model skew results.

The results indicate that the STA model's performance is greatly influenced by the stiffness of the translational restriction. In this context, the modified version of the model exhibits larger deformations than any method using springs, and the version incorporating a spring-stiffened hinge significantly amplifies these deformations, effectively doubling even the modified version.

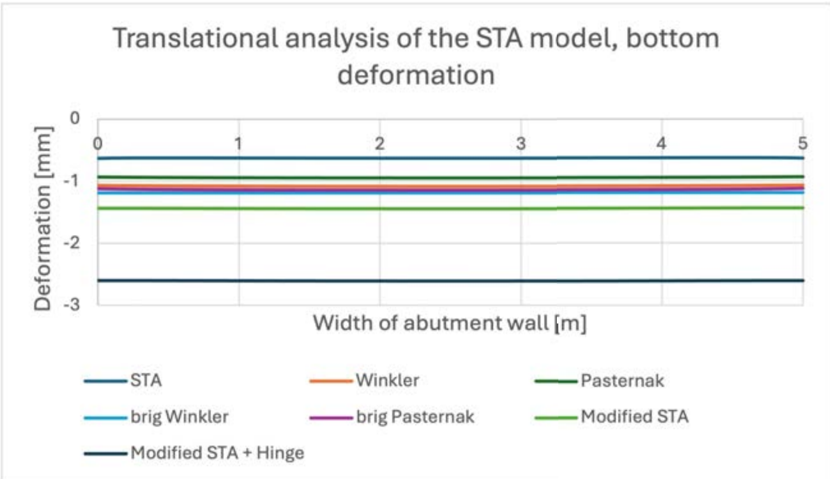

Figure 4.51: Deformations on the bottom of the slab, STA translational analysis.

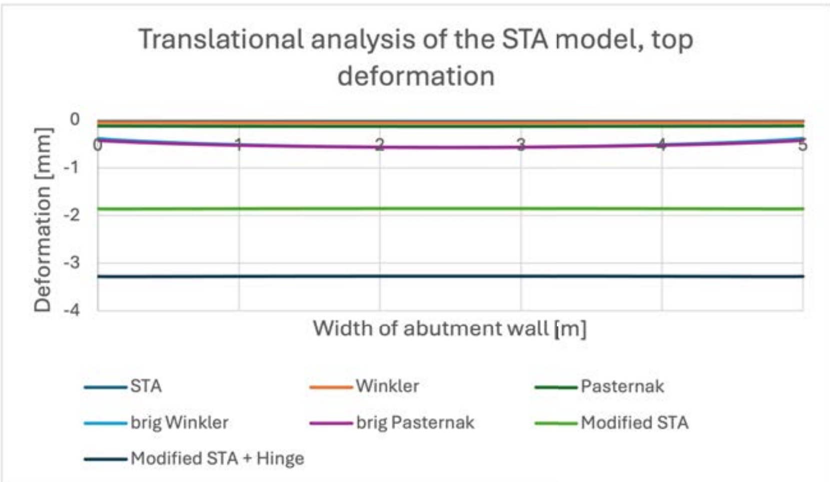

Figure 4.52: Deformations on the top of the abutment wall, STA translational analysis.

4.11 Force equilibrium process for the STA method

Iterations done for Bridge 4 presented in figure 4.53 to figure 4.55 in accordance to STA regulations. To see other bridge design iterations see Appendix A.6. The results show that an average of 4 iterations of the simulations was required to reach a relative error of 0.00%, with Bridge 4 being an outlier that had a subsequent increase of one for each increase in bridge height for the designs. Indicating that lower stiffness of the abutment wall leads to more iterations required to reach equilibrium of the STA process.

Bridge 4-1			
iteration	load [kN/m²]	Deformation [mm]	Relative error
1	2.3144	-0.771473	-
2	2.2829	-0.760963	1.38%
3	2.2833	-0.761106	-0.02%
4	2.2833	-0.761104	0.00%

Figure 4.53: Iteration processes for Bridge 4-1.

Bridge 4-3			
iteration	load [kN/m²]	Deformation [mm]	Relative error
1	6.2767	-2.09223	-
2	5.9204	-1.97345	6.02%
3	5.9406	-1.98019	-0.34%
4	5.9394	-1.97981	0.02%
5	5.9395	-1.97983	0.00%

Figure 4.54: Iteration processes for Bridge 4-3.

Bridge 4-5			
iteration	load [kN/m²]	Deformation [mm]	Relative error
0	12.6969	-4.23229	-
1	10.7432	-3.58106	18.19%
2	11.0438	-3.68127	-2.72%
3	10.9976	-3.66585	0.42%
4	11.0047	-3.66822	-0.06%
5	11.0036	-3.66785	0.01%
6	11.0037	-3.66791	0.00%

Figure 4.55: Iteration processes for Bridge 4-5.

5 Discussion

In this chapter the results from the parametric study will be discussed and evaluated, aiming to interpret the outcome of the research.

Nonlinear springs that cut-off forces in tension were used to reflect and capture the behaviour of the soil mechanics and resulted in greater computational times, since it requires iterations. Even including non-linear springs the time it took to run the simulation and get results cannot be compared to the time it takes to use the method brought forth by the Swedish Transport Authority. The force equilibrium that is calculated through manual iterations of simulations in the STA model is far slower

By including the plasticity of the soil the contact stresses at the surface of the abutment wall affects and significantly limits the translation of forces into the soil at the surface. However, the passive earth pressure increases rapidly, meaning it is confined to the surface. Beyond a depth of approximately 0.5 meters, the forces are no longer constrained by the soil's failure criterion. As seen in the results from the three models analysed in the failure criteria simulations, the sectional forces and deformations remain similar. This indicates that including the passive earth pressure springs does not significantly increase the accuracy of the model. Moreover, implementing springs that take the failure criterion into account is time consuming in RFEM. .

Modelling foundations with the Winkler method, often overshoots the deformations since the load is only distributed through the stiffness of the structure which in turn affects the accuracy of the model. However, the structure of a portal frame creates a complex interplay between the methods of modelling which affect the outcome of the deformations. Hence, it is often seen in the results shown in Appendix A.9 that the deformations at the surface of the abutment wall reflect the expected behaviour between the Winkler and Pasternak method, while the deformation in the bottom of the slab indicates that the opposite is true if the foundation slab exhibits movement in the same direction as the bridge deck. This is due to the propagation of loads in the soil. Winkler gives large initial deformations at the surface which quickly decrease with depth, while Pasternak has lower initial deformations at the surface due to the loads being distributed more because of the shear capabilities of the spring bed. This results in smaller deformations at the surface but larger deformations in the foundation slab.

When the size of the abutment wall increases, the spring stiffness decreased in accordance to the stress distribution theory applied to the spring models.The same happens for the spring stiffness applied on the slab when the slab area increases as seen in appendix A.4 table A.5.1. This has been deemed to be somewhat reasonable. If the spring stiffness did not decrease, the soil could have been too stiff leading to underestimations of the soil deformation in the RFEM models. It is challenging to see if these stiffnesses are reasonable enough for real life soil behaviour without conducting any soil deformation tests out in the field and adjust the data to the current models.

However, as mentioned it is deemed that the spring stiffness behaviour is reasonable to not exaggerate or undermine the soil deformations. According to the formulas used for deriving the spring stiffness the elastic modulus of the soil changes the stiffness of the springs linearly, meaning an increase of elasticity from 25 MPa to 50 MPa doubles the spring stiffness.

The Pasternak models have shear mechanisms which allows the soil to translate forces more accurately compared to the Winkler models. Worth noting is that full effect of the shear translation is not able to take place for the Pasternak model since the force is applied by the surface, not allowing for forces to translate over the top of the abutment wall. This means that the Pasternak model is not as effective in distributing the forces in this specific case compared to a traditional foundation model where the slab is surrounded by soil. The result of this means that the sectional forces at the surface from the Pasternak model will resemble the Winkler method and may be the cause of the steep increase in contact stresses which has been deemed a software error. The error exhibited by Pasternak methods across all shear coupled models, despite variations in different variables is reasoned to be a modelling issue when using RFEM. Because the contact stress curves for the shear models follow similar distributions as the other spring models, it is deemed to be a singular error.

Deciding on a 2:1 stress distribution to determine spring stiffness lacks a direct physical connection. It might be beneficial to conduct a study comparing different inclinations to the chosen approach with a proven model to ascertain the optimal distribution.

In bridge designs with low abutment wall stiffness, the horizontal movement in the foundation slab opposes the loading direction, meaning that it moves in the opposite direction of the bridge deck. For example, in bridge design 4 the deformation in the top of the abutment wall is constant throughout the design, however the deformation in the foundation slab changes drastically. This is due to the behaviour of the soil structure interaction, where the abutment wall lacks sufficient stiffness to remain in contact with the soil as a rigid body throughout the depth of the structure and rotates inwards causing movement away from the soil. Furthermore, the application of nonlinear springs, which possess no stiffness in the positive direction, results in significant inward deformations at the foundation slab.

The behaviour of bridges with heights exceeding four meters exhibited distinct deformation patterns, notably in the direction of horizontal deformation in the foundation slab. The analysis of Bridge 2-2, with an abutment wall height below four meters and Bridge 2, with a height above 4 meters, allowed for comparisons to determine the effect of span length variation on observed behaviours in low stiffness abutment walls. Increasing the span length for bridges above four meters led to an increase in inward movement, aligning with expectations. Interestingly however, increasing the span length resulted in a reversal of deformation direction, mimicking the behaviour of taller bridges. The expectation was that increasing the span length for bridges below 4 meters would cause Translation to be the dominant deformation. However, the phenomenon is attributed to the slimming of bridge deck when the span is increased, reducing stiffness of the structure, and allowing for rotational movement of the bridge deck to be transferred to the abutment wall through the moment stiff joint into the foundation slab. These inwards movements of the slab can also be seen in bridge designs where the height increases, since the slender abutment wall facilitates the same rotational movement as a long bridge deck does.

During the study of soil characteristics, the STA model results do not change at all due to the fact it does not include the elastic modulus for the backfill soil as seen in chapter 2.3, only the unit weight of the soil. This is a simplified approach which impacts the results and could potentially lead to an unconservative design if soft backfill material is present.

When modelling with the Brigade methods it differs from the rest of the methods, in the use of deriving the deformations in the foundation slab. The stiffness in the plane of the slab is not mentioned and it seems as this is disregarded in the theory behind the method, as seen in chapter 2.4. This lack of rotational stiffness leads to rotation which would be greatly reduced with stiffness in the y-direction seen in figure 3.15. The result of this can be seen in all bridge designs, where the deformation in the bottom slab is depicted as a convex shape for the Brigade method. Adding stiffness in the y-direction would flatten this curve and it would resemble other spring methods which include the slab due to the inherent stiffness it brings.

During simulations in which the abutment wall stiffness is considered low, the STA results show substantial deformations at the top of the abutment compared to those in spring bed models. Conversely, STA simulations with stiff abutment walls, which experiences a higher degree of rigid body motion, exhibit smaller deformations at the top of the abutment wall relative to the spring models. This occurs because the STA model fails to accurately represent the bridge when it undergoes translational movements of the structure. Since the movement of the foundation slab is completely restricted, the model underestimates the deformations during translational events. This limitation is evident in the results from the translational analysis, which indicate that the model highly depends on the stiffness of the translational restrictions. The lack of representation of translation stems from the assumption that there is no movement in the bottom slab - an assumption that is difficult to justify in practical situations. As demonstrated in other models, the foundation slab does move due to braking loads.

As mentioned, only the characteristics braking loads were applied on the bridge decks for all the models, because only the behaviour of the sectional forces, deformations and contact stresses were of relevance. Applying safety factors would not affect these behaviours only scaling the magnitude of them. Therefore, when analysing the parametric study, the behaviour of the curves in the diagrams are of utmost importance.

When comparing the contact stresses of the abutment wall and how earth pressure is calculated in different models, the STA models stand out. The calculated earth pressure in the Spring models provides a distribution that aligns reasonably well with soil mechanics theory and the load placement. By allowing movement of the bottom slab, a more realistic behaviour of the bridge is obtained compared to an actual portal frame bridge structure.

In contrast, the STA models exhibit a triangular distribution with maximum contact stress at the middle of the abutment wall and zero stress at the top of the wall and bottom of the wall, without any reduction in contact stresses due to soil depth. To argue that the STA model is more conservative would not be entirely accurate when studying the different sectional forces in Appendix A.9. While the STA model does not always yield the highest values, it often simplifies the distribution, resulting in the linear distributions for the entire section, making it a conservative design approach. However, a major downside to this approach is the potential hindrance of structural optimization when attempting to conserve material to reduce the environmental footprint and material costs of a structure.

The lack of consideration to ground water has a huge impact on all the spring models when calculating the stress distribution with the 2-1 method. It also affects the STA models where the unit weight of the soil will change. It will for all methods lead to a reduced earth pressure if the groundwater level is present at a depth between the surface and z max. This is due to the buoyant force from the ground water. If the ground water level is present on a depth that will affect the stress distribution, this should be considered and calculated for when deriving the stress distribution in the soil, to get the right settlements for the spring stiffness equations.

By using RFEM it has been easy to implement the various methods since the user manual explains how to implement spring stiffnesses and Pasternak shear coefficients and the user interface facilitates the use of springs on surfaces in a simple yet efficient way. However, the exact way the calculations of the Pasternak hypothesis are not presented in the manual and it might be optimal to study this further since the shear coupling stiffness impacts the results. RFEM easily allowed for the geometry of the bridge to be parameterized in the software which eased the analysis of the various bridges.

6 Conclusion

A conclusion that can be drawn from this thesis is that the reasoning behind the Swedish Transport Authority method consists of simplifications when modelling the physical behaviour of the bridge models. Specifically, the Swedish Transport Authority assumes that the foundation slab experiences no movement, coupled with determining the maximum earth pressure at the centre of the abutment wall through an iterative force equilibrium process.

The spring models provide a more adequate earth pressure distribution which reflects the physical behaviour of the structure, including movement at the bottom slab. This is reflected in the sectional forces, with a reduction in moment and shear forces along the depth of the structure. The STA models has very little decline in forces along the depth compared to the spring models which indicates the Swedish Transport Authority underestimates the soil structure interaction. The incorporation of shear springs appears to only impact the deformations, but not having any significant effect on the sectional forces. A more adequate earth pressure distribution as indicated by the spring models, taking the soil plasticity into account, would be the following: steep incline from 0 to maximum contact forces roughly 0.5 meters below the surface, then gradually decreasing contact forces with depth until it reaches a minimum value by the foundation slab (see figure 6.1).

No correlation was discovered between the variation of parameters and the sectional forces. However, some noticeable trends in the behaviour of the bridge were observed when varying the parameters. The performance of the spring bridge models was primarily influenced by the folowing key parameters, the stiffness of the abutment wall, the contact area between the soil backfill and the abutment wall. Additionally, the stiffness of the backfill soil itself was also a critical factor in determining the overall behaviour of the sectional forces.

All the models have different stages that may be somewhat time consuming, regarding the computational time effort. The spring models need a calculation to derive the correct stiffnesses. The STA model is time consuming due to its nature of being an iterative process. Not accounting for the soil's failure criteria does not significantly reduce accuracy of corresponding models and could be used as a method to reduce the computational efforts of the spring models.

Overall this master thesis aimed to initiate further discussions regarding the need for updating the Swedish Transport Authority's regulations concerning increased earth pressure. The findings reveal discrepancies in the model's representation and ability to accurately illustrate the magnitude of earth pressure compared to alternative methods, highlighting the necessity for reconsideration and refinement of current practices.

Below are some key points from the parametric study.

- The stiffness of the abutment wall and bridge deck, both affects the structural behaviour in regard to deformations, contact stresses and sectional forces.
- A closed cross-section of the bridge resulted in a rigid body motion of the structure.
- The elastic modulus variation had no significant impact on the soil under the foundation, but varying it in the soil against the abutment wall, the stiffness in all spring models were affected.
- Considering passive earth pressure failure, the deformations and sectional forces were similar to the simplified models.

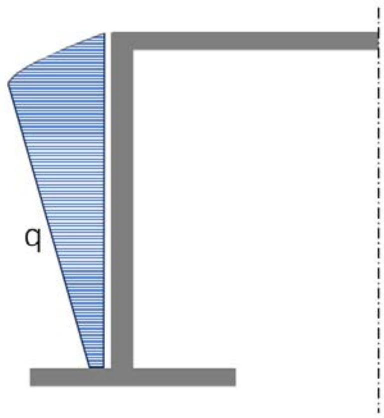

Figure 6.1: Schematic of the earth pressure distribution derived from spring models.

7 Further studies

During the progression of this work, several important questions have emerged in the subject area that could be interesting for further studies.

- Compare the results from the thesis with a soil continuum model.
- The impact of soil layers with different unit weights and elastic modulus.
- Compare the already existing spring models with soil testing to replicate realistic soil conditions.
- Run the same tests but implement vertical forces such as self-weight and other vertical loads that are present on a bridge deck and together with this add the effect of thermal loading.
- Add different models of the wing walls to study its impact.
- The Stress distribution method could be further optimised by changing the inclination i =1/2, with real life soil testing.

Bibliography

[1] Martin P Burke Jr. "Integral Bridges: Attributes and Limitations". In: (1993). ISSN: 0361-1981.

[2] Trafikverket. "Bro och broliknande konstruktion, Byggande". Version 2. In: (2021), p. 191.

[3] John S Horvath. *Soil-Structure Interaction Research Project "A Practical Subgrade Model for Improved Soil-Structure Interaction Analysis: Parameter Assessment"*. Manhattan College School of Engineering Civil and Environmental Engineering Department, 2011.

[4] Baban Bapir, Lars Abrahamczyk, Torsten Wichtmann, and Luis Felipe Prada-Sarmiento. "Soil-structure interaction: A state-of-the-art review of modeling techniques and studies on seismic response of building structures". In: *Frontiers in Built Environment* 9 (2023), pp. 1–17.

[5] E Yandzio A R Biddle D C Iles. *Integral Steel Bridges: Design Guidance*. 2007.

[6] Lundmark Tore Collin Peter. "Towards a better built environment - innovation, sustainability, information technology; Competitive Swedish Composite Bridges". In: *Symposium Towards a Better Built Environment - Innovation, Sustainability, Information Technology* (2002).

[7] Jaromir Krizek. "Integral Bridges Soil-Structure Interaction". PhD thesis. Czech Technical University in Prague, 2011.

[8] *Modern Earth Buildings Materials, Engineering, Constructions and Applications*. Woodhead Publishing, 2012.

[9] Ola Dahlblom and Erika Tudisco. *Course literature in Foundation Engineering*. Geotechical Engineering, LTH, Lund university, 2019.

[10] Ian F Collins. "Elastic/plastic models for soils and sands". In: *International journal of Mechanical Sciences* 47 (2004), pp. 493–508.

[11] Ola Dahlblom. *Kompendium i Geoteknik*. Instutitionen för byggvetenskaper, LTH, Lunds universitet, 2021.

[12] Abolfazl Eslami, Sara Moshfeghi, Hossein MolaAbasi, and Mohammad M. Eslami. *Piezocone and Cone Penetration Test (CPTu and CPT) Applications in Foundation Engineering*. Butterworth-Heinemann, 2020.

[13] John S Horvath. *Soil-structure interaction research project basic SSI concepts and applications overview*. Manhattan College School of Engineering Center for Geotechnology, 2002.

[14] David A Dillard, Bikramjit Mukherjee, Preetika Karnal, Romesh C Batra, and Joelle Frechette. "A review of Winkler's foundation and its profound influence on adhesion and soft matter applications". In: *Soft Matter* 14 (2018), pp. 3669–3683.

[15] Dlubal. *RFEM 5 Spatial Models Calculated According to Finite Element Method*. Dlubal Software, 2020.

[16] Hideaki Tanahashi. “Pasternak Model Formulation of Elastic Displacements in the Case of a Rigid Circular Foundation”. In: *Journal of Asien architecture and building and building engineering* 6.1 (2007), pp. 167–173.

[17] Arnold D Kerr. “Elastic and Viscoelastic Foundation Models”. In: *Journal of Applied Mechanics* (1964), pp. 491–498.

[18] Landsbygds och infrastrukturdepartementet RSIB US. *Förordning (2010:185) med instruktion för Trafikverket*. Sveriges riksdag, 2010.

[19] Trafikverket. “Bro och broliknande konstruktion, Bärighetsberäkning”. Version 1. In: (2022), p. 160.

[20] Scanscot Technology AB. *BRIGADE/Standard*. Scanscot, 2022.

[21] Niels Ottosen and Hans Petersson. *Introduction to the finite element method*. England: Pearson Education Limited, 1992.

[22] S.S. Quek G.R. Liu. *The Finite Element Method: A Practical Course*. Elsevier Ltd, 2014, pp. 13–41.

[23] Trafikverket. “Geokonstruktion, Dimensionering och utformning”. Version 1. In: (2022), p. 180.

[24] Tord Isaksson and Annika Mårtensson. *Byggkonstruktion Regel- och Formelsamling*. Studentlitteratur AB, 2020.

Appendix A

Appendix

A.1 STA material backfill values

Table A.1: characteristic values of elasticity modulus for backfill materials [23].

Material/Jordart	**Elasticitetsmodul [MPa]**	
	Löst Lagrad	**Fast Lagrad**
Färstärkningslagermaterial	-	50
Makadamballast	-	50
Underballast	-	50
Krossad sprängsten	-	50
Sorterad sprängsten	-	50
Sprängsten	-	50
Grovkornig mineraljord	10	30
Grus	10	40
Grusig morän	10	40
Sand	5	20
Sandig morän	5	20
Silt	2	10
Siltig morän	2	10

A.2 Weight and earth pressure coefficients

Table A.2: Weight and earth pressure coefficients [19].

Material	Tunghet		Koefficienter för jordtryck		
	över grund-vattenytan	under grund-vattenytan	vilo-jordtryck K_o	aktivt jordtryck K_a	passivt jordtryck K_p
Krossad sprängsten	18	11	0,34	0,17	5,83
Förstärkningslager-material	22	12	0,29	0,22	4,60
Sprängsten	17	10	0,29	0,17	5,83
Grus	19	12	0,40	0,25	4,02
Sand	18	11	0,43	0,27	3,70
Lättklinker	5	0	0,43	0,27	-
Cellplast	1	0	0,14	0,05	-

The calculations was performed using the following equation:

$$\Delta\sigma_H = \sigma_v(z) \cdot (K_p - K_o) \quad \text{(A.1)}$$

The coefficients used where approximated from table A.3. A soil unit weight of 20 kN/m^3, Passive earth pressure coefficient K_p=5.0 and a resting earth pressure K_o=0.3. The passive earth pressure was only calculated to a depth of 1 meter.

Table A.3: The value of the passive earth pressure for the centre of each element (element size 0.1 meters).

Depth [m]	Pressure [kN/m^3]
0.05	≈ 0
0.15	14.1
0.25	23.5
0.35	32.9
0.45	42.3
0.55	51.7
0.65	61.1
0.75	70.5
0.85	79.9
0.95	89.3
1.05	98.7

A.3 Braking loads

The formula presented in chapter 2.5:

$$Q_lk = 0.6a_{Q1}(2Q_{1k}) + 0.1a_{q1}q_{1k}w_1L_f \tag{A.2}$$

$$180a_{Qi}(kN) \leq Q_{lk} \leq 900 \text{ [kN]} \tag{A.3}$$

Is used for each notional lane and creates the following equations for lane one to lane three. Past lane three the coefficients are 0 hence why the maximum notional lane loads is set to three lanes:

$$Q_{1k} = 0.6 \cdot 0.9 \cdot 2 \cdot 300 + 0.1 \cdot 0.8 \cdot 9 \cdot 3 \cdot L_f = 324 + 2.16 \cdot L_f \text{ [kN]} \tag{A.4}$$

$$Q_{2k} = 0.6 \cdot 0.9 \cdot 2 \cdot 200 + 0.1 \cdot 1.0 \cdot 2.5 \cdot 3 \cdot L_f = 216 + 0.75 \cdot L_f \text{ [kN]} \tag{A.5}$$

$$Q_{3k} = 0.60 \cdot 2 \cdot 100 + 0.1 \cdot 1.0 \cdot 2.5 \cdot 3 \cdot L_f = 0.75 \cdot L_f \text{ [kN]} \tag{A.6}$$

Worth noting is that this is the load per axle, however in this thesis the loads are set as point loads in 4 nodes meaning that the applied load will be the following (equation A.7):

$$P_{i,k} = \frac{Q_{lk}}{2} \tag{A.7}$$

The applied point loads are presented in the table below and only the point loads for each notional lanes that fits the width of the structure is derived.

Table A.4: The applied braking point loads for each bridge model.

Braking loads				
	Span	Point Load 1 [kN]	Point Load 2 [kN]	Point Load 3 [kN]
Bridge 1-1	5	167	-	-
Bridge 1-3	5	167	110	2
Bridge 1-5	5	167	110	2
Bridge 2-1	5	167	110	-
Bridge 2-3	15	176	114	-
Bridge 2-5	25	186	117	-
Bridge 2-2-1	5	167	110	-
Bridge 2-2-3	15	176	114	-
Bridge 2-2-5	25	186	117	-
Bridge 3-1	8	170	111	-
Bridge 3-3	8	170	111	-
Bridge 3-5	8	170	111	-
Bridge 4-1	5	167	110	-
Bridge 4-3	5	167	110	-
Bridge 4-5	5	167	110	-
Bridge 5-1	5	167	-	-
Bridge 5-3	5	167	-	-
Bridge 5-5	5	167	-	-
Bridge 6-1	5	167	-	-
Bridge 6-3	5	167	-	-
Bridge 6-5	5	167	-	-
Bridge 7-1	5	167	-	-
Bridge 7-3	5	167	-	-
Bridge 7-5	5	167	-	-

A.4 Derivation of main springs

The equation which derives uniformly spring stiffness based on stress distribution in the soil for the slab (equation A.8):

$$\Delta\sigma_z = \frac{q \cdot b \cdot l}{(b + 2 \cdot iz)(l + 2 \cdot iz)} \tag{A.8}$$

Assumes linear 1:2 distribution according to figure A.1 below. The equation for the

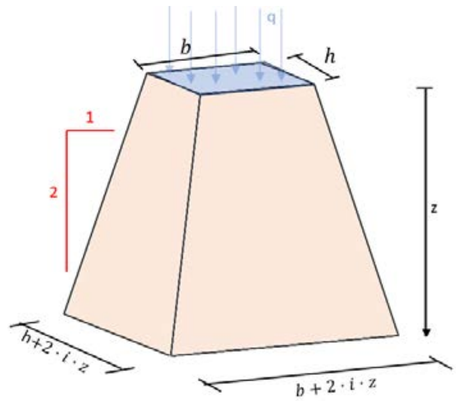

Figure A.1: Illustration of the 2-1 method used in equation A.8.

abutment wall needs a modified version of equation A.8 to restrict stress distribution beyond the surface of the soil as seen in figure A.2 below.

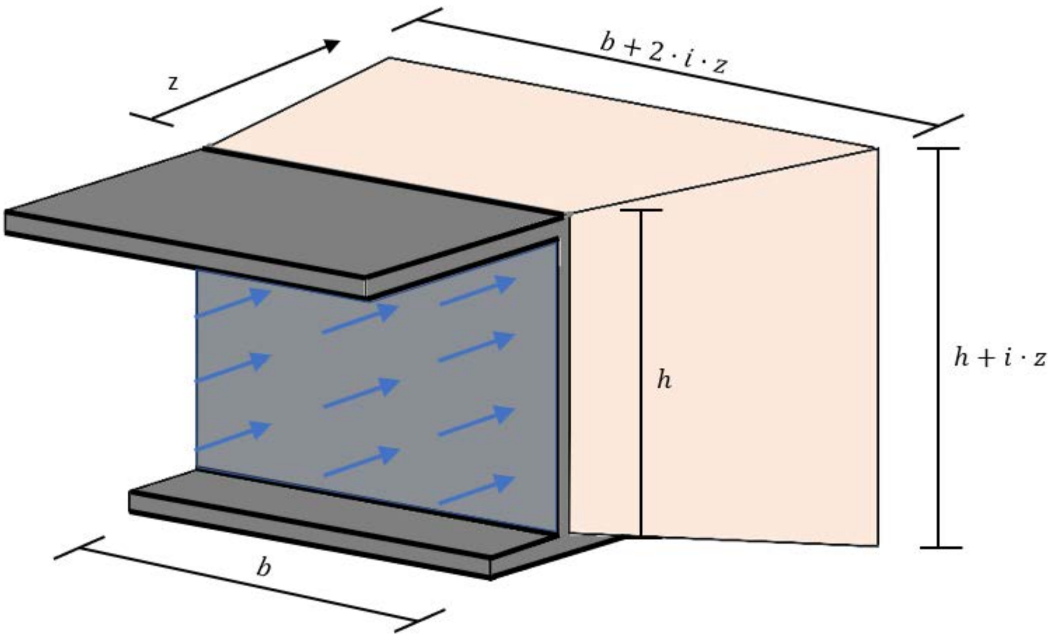

Figure A.2: stress propagation through the soil, accounting for the surface.

Which creates the following equation (equation A.9):

$$\Delta\sigma_z = \frac{q \cdot b \cdot l}{(b + 2 \cdot iz)(l + iz)} \tag{A.9}$$

The settlements, δ in the soil was then calculated with the following formula (equation A.10):

$$\delta = \int_0^z \varepsilon_z dz = \int_0^z \frac{\Delta\sigma_z}{E} dz \tag{A.10}$$

The Young´s Modulus used in the thesis was set to a constant for the slab and abutment wall E_1 =50MPa, E_2 =100MPa. And a soil depth of z =2m for both instances as seen in figure 3.2. The spring stiffness k_w was then calculated as equation A.11 where P =1N.

$$k_w = \frac{P}{\delta} \tag{A.11}$$

When deriving the main springs for the abutment wall the wing walls are considered, which adds a constant length onto the walls of 4.24 meters due to their 45-degree angle regardless of bridge design. The process was repeated for each design. The spring stiffness for each bridge model is presented in table A.5.

Table A.5: The spring stiffness used for the Winkler and Pasternak models.

	Slab			Abutment wall			
	base [m]	length [m]	spring stiffness [k	base [m]	l0 [m]	length [m]	Spring stiffness [kN/m³]
Bridge 1-1	2	5	84110	4	5	9.24	30830
Bridge 1-3	2	9	78970	4	9	13.24	30000
Bridge 1-5	2	14	76580	4	14	18.24	29460
Bridge 2-1	3	7	73400	6	7	11.24	29310
Bridge 2-3	3	7	73400	6	7	11.24	29310
Bridge 2-5	3	7	73400	6	7	11.24	29310
Bridge 2-2-1	3	7	73400	4	7	11.24	30340
Bridge 2-2-3	3	7	73400	4	7	11.24	30340
Bridge 2-2-5	3	7	73400	4	7	11.24	30340
Bridge 3-1	2	7	80832	5	7	11.24	29722
Bridge 3-3	3.5	7	71189	5	7	11.24	29722
Bridge 3-5	5	7	63388	5	7	11.24	29722
Bridge 4-1	2	7	80832	4	7	11.24	30339
Bridge 4-3	2	7	80832	6	7	11.24	29306
Bridge 4-5	2	7	80832	8	7	11.24	28781
Bridge 5-1	2	5	84110	4	5	9.24	30830
Bridge 5-3	2	5	84110	4	5	9.24	30830
Bridge 5-5	2	5	84110	4	5	9.24	30830
Bridge 6-1	2	5	42055	4	5	0.00	30830
Bridge 6-3	2	5	84110	4	5	0.00	30830
Bridge 6-5	2	5	126165	4	5	0.00	30830
Bridge 7-1	2	5	84110	4	5	9.24	12331
Bridge 7-3	2	5	84110	4	5	9.24	30830
Bridge 7-5	2	5	84110	4	5	9.24	49325

A.5 Model verification

A.5.1 Verification of maximum deflection of the bridge deck

The following calculations were conducted for Bridge 1-1 to compare the maximum deflection of the bridge deck with the RFEM models in figures A.5 - A.9.

Table A.6: Bridge model 1-1 properties.

Variable	**Value**
Bridge deck thickness, t	0.75 [m]
Bridge deck width, b	5 [m]
Span length of bridge deck, L	5 [m]
Youngs modules for concrete quality C40/C50, E_c	35 [GPa]
Density of concrete quality C40/50, ρ_c	2500 [kg/m^3]

The self-weight of the bridge deck and the moment of inertia, I_y was calculated in accordance with equation A.12 and A.13. The self-weight was calculated as a uniformed distributed load, q_c.

$$q_c = \rho_c \cdot t \cdot g \cdot b = 2500 \cdot 0.75 \cdot 10 \cdot 5 = 62.5 \text{ [kN/m]} \tag{A.12}$$

$$I_y = \frac{b \cdot t^3}{12} = \frac{5 \cdot 0.75^3}{12} = 0.1758 \text{ [m}^4\text{]} \tag{A.13}$$

The two different elementary cases was calculated below in equation A.14 and A.15.

Case I, deflection u_I of a simply supported beam [24].

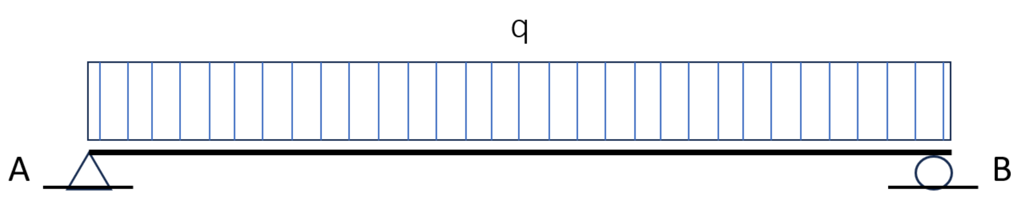

Figure A.3: Simply supported beam.

$$u_I = \frac{5 \cdot q_c \cdot L^4}{384 E I_y} = 0.083 \text{ [mm]} \tag{A.14}$$

Case II, deflection u_{II} of a fixed beam [24].

$$u_{II} = \frac{q_c \cdot L^4}{384 E I_y} = 0.017 \text{ [mm]} \tag{A.15}$$

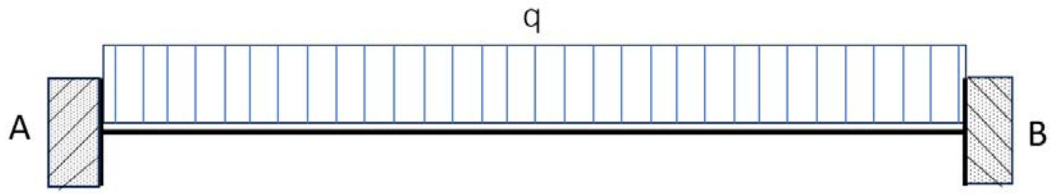

Figure A.4: Fixed beam.

Table A.7: Deformations of bridge deck for Bridge 1-1 from equation A.14,A.15 and figures A.5 - A.9.

Case I, u_I [mm]	**Case II, u_{II}[mm]**	**STA , [mm]**	**Winkler [mm]**	**Pasternak [mm]**	**Brigade Winkler [mm]**	**Brigade Pasternak [mm]**
0.083	0.017	0.083	0.067	0.068	0.074	0.074

As seen in table A.7, the Bridge decks has similar but not the same maximum deformation for Case II compared to the RFEM models. This is a direct cause due to the deformation of the abutment walls which in theory means that the end supports of the bridge deck are not fully fixed with no vertical movement as the elementary cases are. The springs on the foundation plate allows slip for all the spring models, allowing the structure to move inwards. This results in the bridge deck being pushed upwards, reducing the deformation of the Bridge deck. This slip inwards can be seen in figure A.10 depicting this for the Winkler model in comparison to the STA model, which does not slip inwards A.11.

It is therefore assumed that the deflection from the RFEM models is reasonable, hence they lie between elementary Case I and Case II.

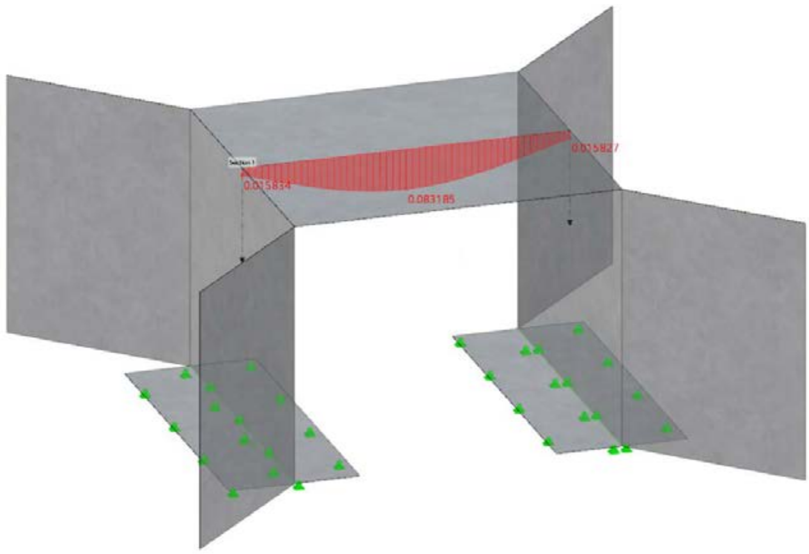

Figure A.5: Deflection of Bridge model 1-1 (STA) [mm], with self weight.

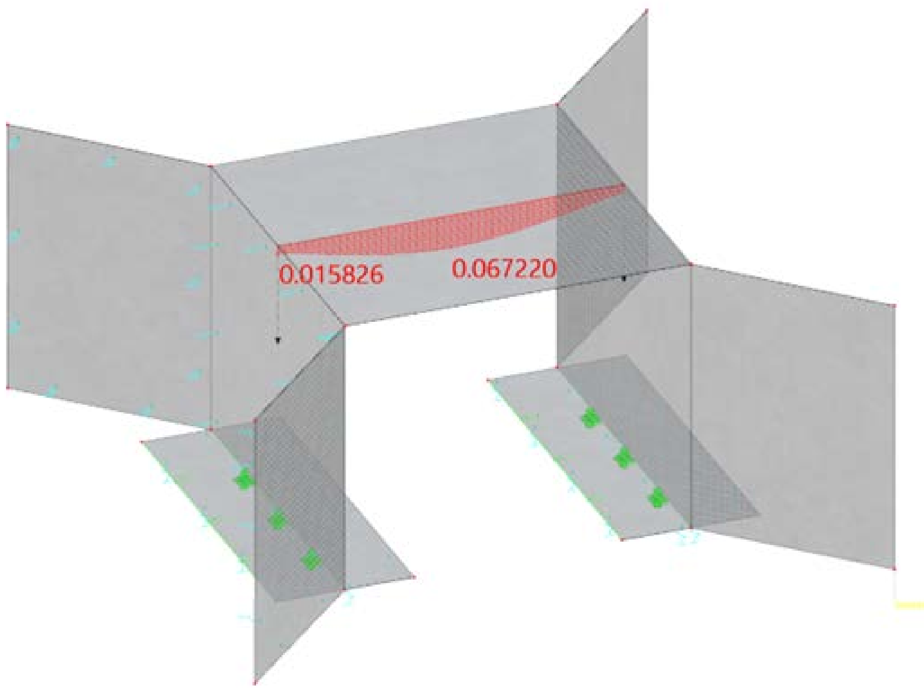

Figure A.6: Deflection of Bridge model 1-1 (Winkler) [mm], with self weight.

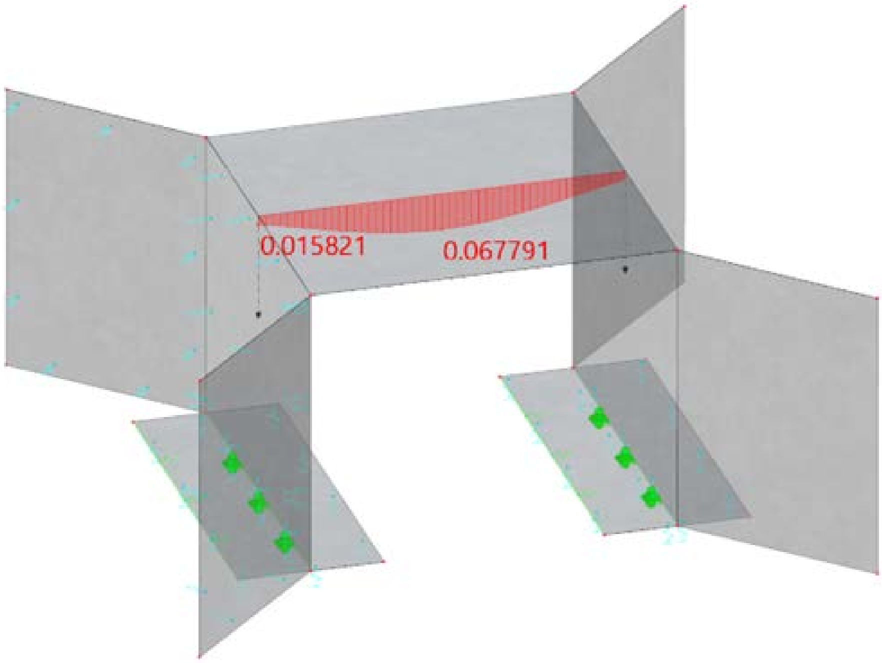

Figure A.7: Deflection of Bridge model 1-1 (Pasternak) [mm], with self weight.

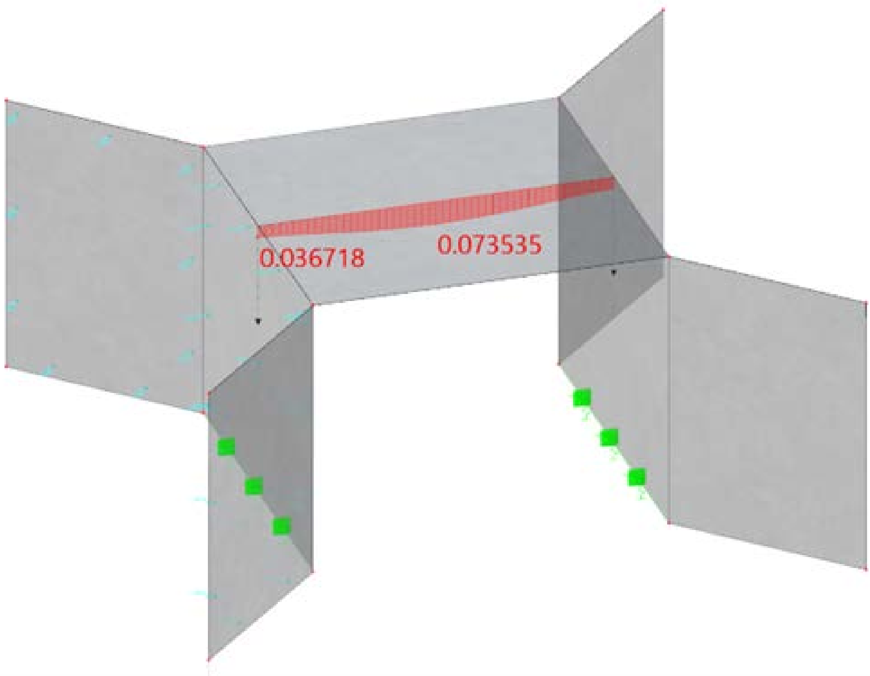

Figure A.8: Deflection of Bridge model 1-1 (Brigade Winkler) [mm], with self weight.

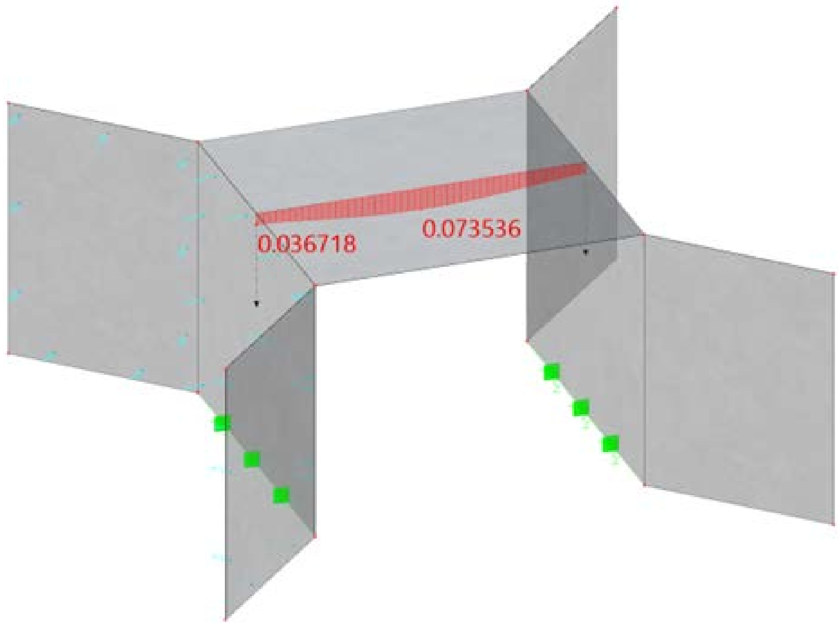

Figure A.9: Deflection of Bridge model 1-1 (Brigade Pasternak) [mm], with self weight.

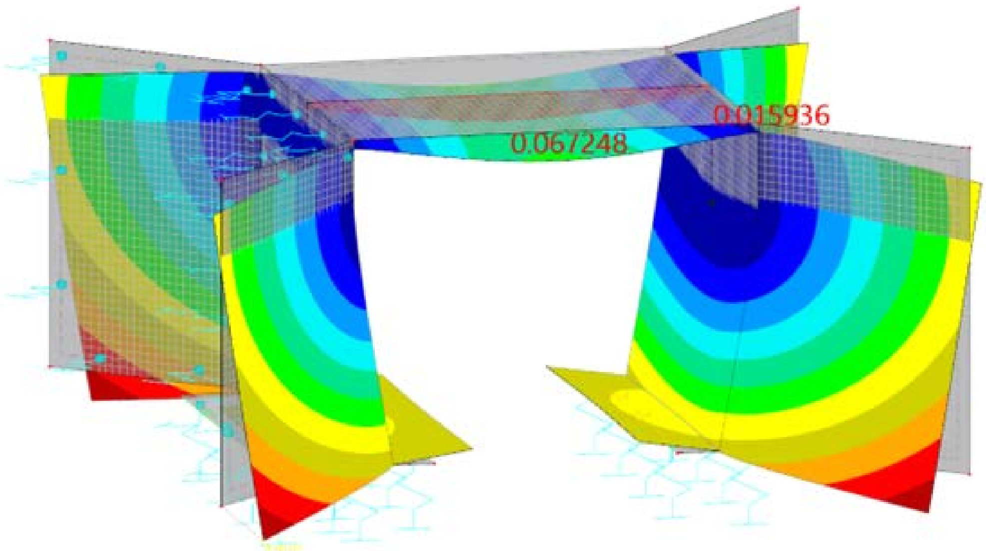

Figure A.10: Deflection direction of Bridge model 1-1 (Winkler) [mm], with self weight.

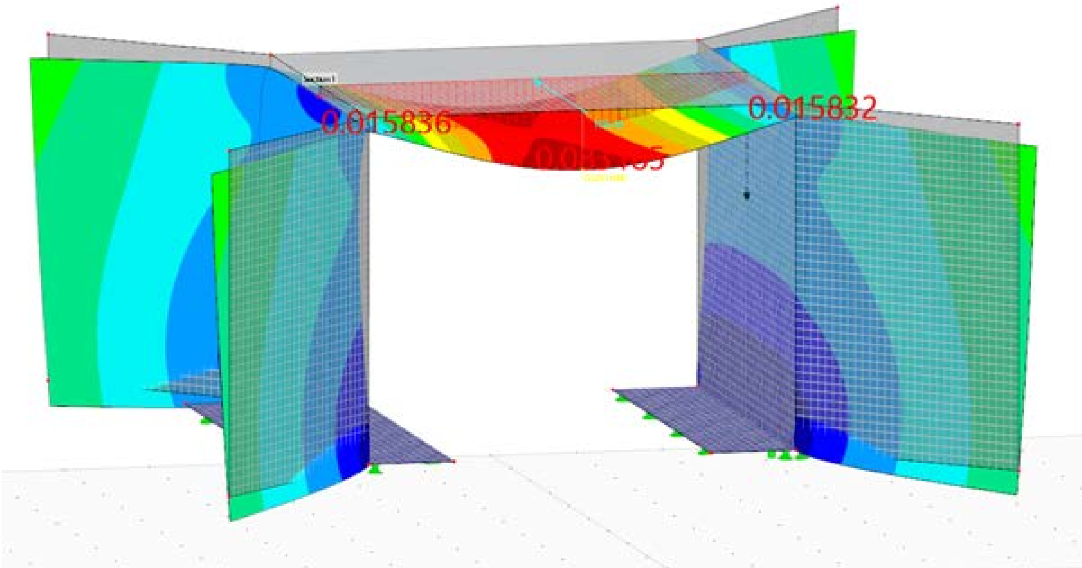

Figure A.11: Deflection direction of Bridge model 1-1 (STA) [mm], with self weight.

A.5.2 Verification of moment distribution curve of the bridge deck

The moment distribution curve as seen in figures A.12-A.16 was compared with the moment distribution from the elementary cases, Case I (simply supported) and Case II (fixed beam) [24]. It showed that the moments from the RFEM models had similar distribution curves as for Case II. Indicating that the bridge deck acts more as a fixed beam than a simply supported one.

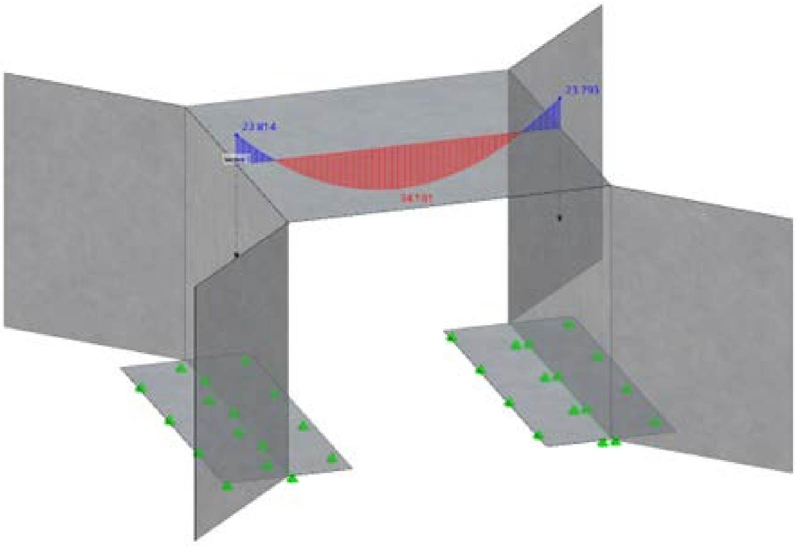

Figure A.12: Moment distribution of Bridge model 1-1 (STA) [kNm/m], due to self weight on the bridge deck.

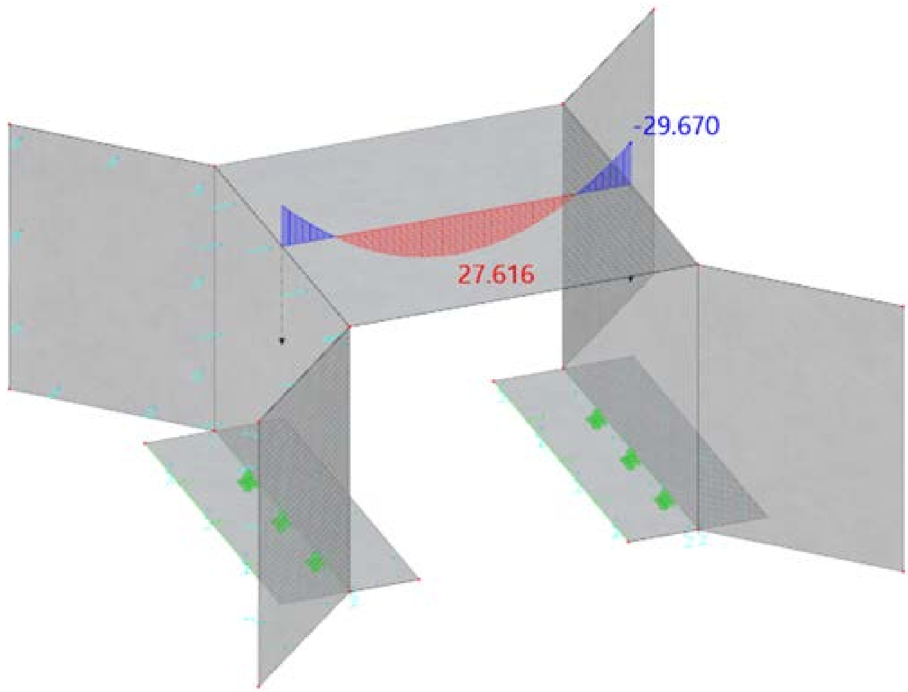

Figure A.13: Moment distribution of Bridge model 1-1 (Winkler) [kNm/m], due to self weight on the bridge deck.

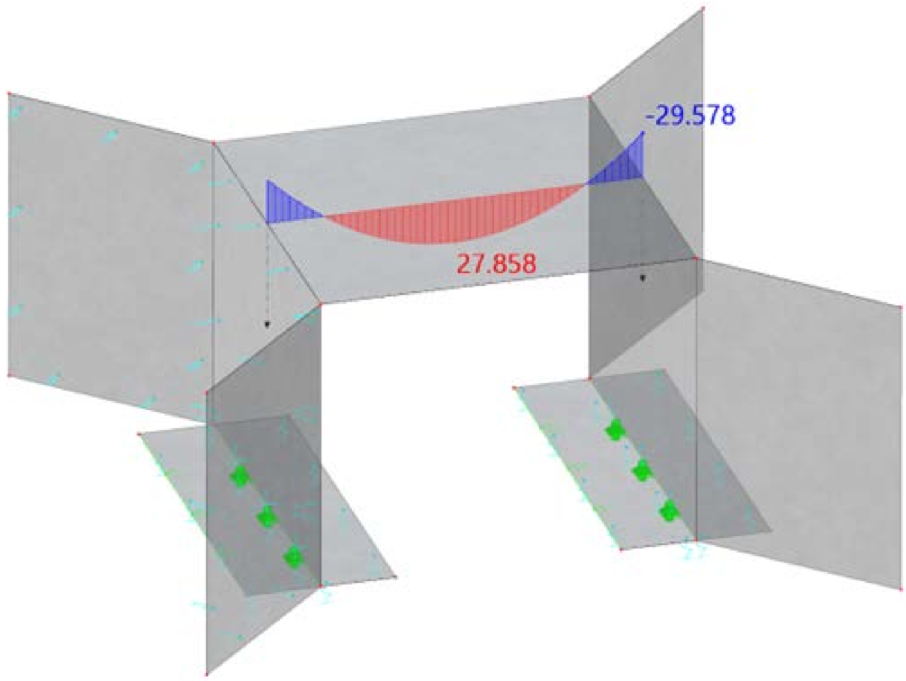

Figure A.14: Moment distribution of Bridge model 1-1 (Pasternak) [kNm/m], due to self weight on the bridge deck.

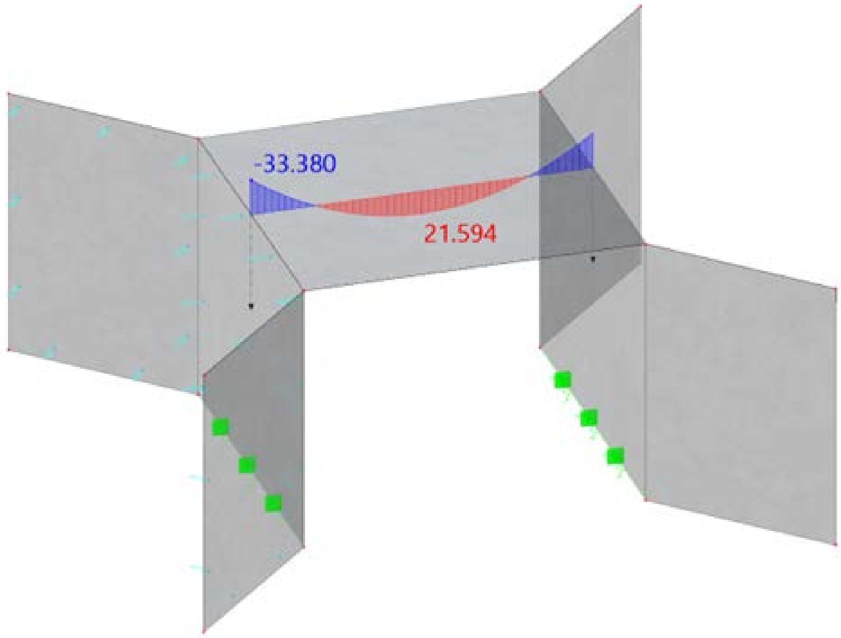

Figure A.15: Moment distribution of Bridge model 1-1 (Brigade Winkler) [kNm/m], due to self weight on the bridge deck.

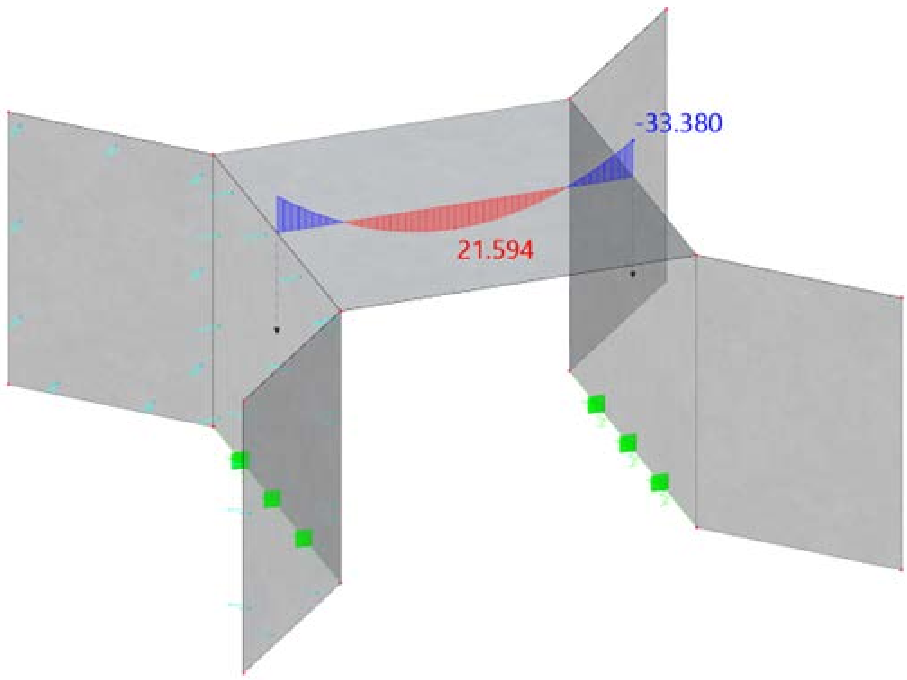

Figure A.16: Moment distribution of Bridge model 1-1 (Brigade Pasternak) [kNm/m], due to self weight on the bridge deck.

A.6 Earth pressure from the STA model

The results from the iterative process explained in chapter 3.1.4 are presented in table A.11 for each bridge design.

Table A.8: Increased earth pressure from the STA model derived from the horizontal deformation in the bridge deck for Bridge 1 and Bridge 2

Bridge 1-1			
iteration	load [kN/m^2]	Deformation [mm]	Relative error
1	1.8954	-0.631785	-
2	1.8699	-0.623312	1.36%
3	1.8703	-0.623426	-0.02%
4	1.8703	-0.623424	0.00%

Bridge 2-1			
iteration	load [kN/m^2]	Deformation [mm]	Relative error
§	6.2745	-2.09149	-
1	5.9184	-1.97281	6.02%
2	5.9386	-1.97954	-0.34%
3	5.9375	-1.97916	0.02%
4	5.9375	-1.97918	0.00%

Bridge 1-3			
iteration	load [kN/m^2]	Deformation [mm]	Relative error
1	1.8178	-0.605921	-
2	1.7928	-0.597598	1.39%
3	1.7931	-0.597712	-0.02%
4	1.7931	-0.597711	0.00%

Bridge 2-3			
iteration	load [kN/m^2]	Deformation [mm]	Relative error
1	8.2586	-2.75285	-
2	7.6987	-2.56622	7.27%
3	7.7366	-2.57887	-0.49%
4	7.7340	-2.57801	0.03%
5	7.7342	-2.57807	0.00%

Bridge 1-5			
iteration	load [kN/m^2]	Deformation [mm]	Relative error
1	1.1771	-0.392361	-
2	1.1607	-0.386914	1.41%
3	1.1610	-0.38699	-0.02%
4	1.1610	-0.386988	0.00%

Bridge 2-5			
iteration	load [kN/m^2]	Deformation [mm]	Relative error
1	9.8297	-3.27656	-
2	9.0884	-3.02948	8.16%
3	9.1443	-3.04811	-0.61%
4	9.1401	-3.04671	0.05%
5	9.1404	-3.04681	0.00%

Table A.9: Increased earth pressure from the STA model derived from the horizontal deformation in the bridge deck for Bridge 2-2 and Bridge 3

Bridge 2-2-1			
iteration	load [kN/m²]	Deformation [mm]	Relative error
0	2.2948	-0.76493	-
1	2.2635	-0.754515	1.38%
2	2.2640	-0.754657	-0.02%
3	2.2640	-0.754654	0.00%

Bridge 3-1			
iteration	load [kN/m²]	Deformation [mm]	Relative error
1	4.4348	-1.47828	-
2	4.2929	-1.43097	3.31%
3	4.2974	-1.43248	-0.11%
4	4.2973	-1.43243	0.00%

Bridge 2-2-3			
iteration	load [kN/m²]	Deformation [mm]	Relative error
1	3.1307	-1.04355	-
2	3.0782	-1.02606	1.70%
3	3.0791	-1.02635	-0.03%
4	3.0791	-1.02635	0.00%

Bridge 3-3			
iteration	load [kN/m²]	Deformation [mm]	Relative error
1	4.4331	-1.47771	-
2	4.2913	-1.43043	3.31%
3	4.2959	-1.43195	-0.11%
4	4.2957	-1.4319	0.00%

Bridge 2-2-5			
iteration	load [kN/m²]	Deformation [mm]	Relative error
1	3.7713	-1.25709	-
2	3.7000	-1.23334	1.93%
3	3.7014	-1.23379	-0.04%
4	3.7013	-1.23378	0.00%

Bridge 3-5			
iteration	load [kN/m²]	Deformation [mm]	Relative error
1	4.7880	-1.59601	-
2	4.6190	-1.53967	3.66%
3	4.6250	-1.54166	-0.13%
4	4.6248	-1.54159	0.00%

Table A.10: Increased earth pressure from the STA model derived from the horizontal deformation in the bridge deck for Bridge 4 and Bridge 5

Bridge 4-1			
iteration	load [kN/m²]	Deformation [mm]	Relative error
1	2.3144	-0.771473	-
2	2.2829	-0.760963	1.38%
3	2.2833	-0.761106	-0.02%
4	2.2833	-0.761104	0.00%

Bridge 4-3			
iteration	load [kN/m²]	Deformation [mm]	Relative error
1	6.2767	-2.09223	-
2	5.9204	-1.97345	6.02%
3	5.9406	-1.98019	-0.34%
4	5.9394	-1.97981	0.02%
5	5.9395	-1.97983	0.00%

Bridge 4-5			
iteration	load [kN/m²]	Deformation [mm]	Relative error
0	12.6969	-4.23229	-
1	10.7432	-3.58106	18.19%
2	11.0438	-3.68127	-2.72%
3	10.9976	-3.66585	0.42%
4	11.0047	-3.66822	-0.06%
5	11.0036	-3.66785	0.01%
6	11.0037	-3.66791	0.00%

Bridge 5-1			
iteration	load [kN/m²]	Deformation [mm]	Relative error
1	3.1919	-1.06395	-
2	3.1181	-1.03937	2.36%
3	3.1198	-1.03994	-0.05%
4	3.1198	-1.03992	0.00%

Bridge 5-3			
iteration	load [kN/m²]	Deformation [mm]	Relative error
1	1.8954	-0.631785	-
2	1.8699	-0.623312	1.36%
3	1.8703	-0.623426	-0.02%
4	1.8703	-0.623424	0.00%

Bridge 5-5			
iteration	load [kN/m²]	Deformation [mm]	Relative error
1	1.3297	-0.443235	-
2	1.3174	-0.439139	0.93%
3	1.3175	-0.439177	-0.01%
4	1.3175	-0.439177	0.00%

Table A.11: Increased earth pressure from the STA model derived from the horizontal deformation in the bridge deck for Bridge 6 and Bridge 7

Bridge 6-1			
iteration	load [kN/m²]	Deformation [mm]	Relative error
1	1.8954	-0.631785	-
2	1.8699	-0.623312	1.36%
3	1.8703	-0.623426	-0.02%
4	1.8703	-0.623424	0.00%

Bridge 6-3			
iteration	load [kN/m²]	Deformation [mm]	Relative error
1	1.8954	-0.631785	-
2	1.8699	-0.623312	1.36%
3	1.8703	-0.623426	-0.02%
4	1.8703	-0.623424	0.00%

Bridge 6-5			
iteration	load [kN/m²]	Deformation [mm]	Relative error
1	1.8954	-0.631785	-
2	1.8699	-0.623312	1.36%
3	1.8703	-0.623426	-0.02%
4	1.8703	-0.623424	0.00%

Bridge 7-1			
iteration	load [kN/m²]	Deformation [mm]	Relative error
1	1.8954	-0.631785	-
2	1.8699	-0.623312	1.36%
3	1.8703	-0.623426	-0.02%
4	1.8703	-0.623424	0.00%

Bridge 7-3			
iteration	load [kN/m²]	Deformation [mm]	Relative error
1	1.8954	-0.631785	-
2	1.8699	-0.623312	1.36%
3	1.8703	-0.623426	-0.02%
4	1.8703	-0.623424	0.00%

Bridge 7-5			
iteration	load [kN/m²]	Deformation [mm]	Relative error
1	1.8954	-0.631785	-
2	1.8699	-0.623312	1.36%
3	1.8703	-0.623426	-0.02%
4	1.8703	-0.623424	0.00%

A.7 Derivation of Brigade springs

Derivation of the rotational springs $k_{\theta t}$ and $k_{\theta l}$is done with the following equation:

$$k_{\theta t} = \frac{E_k \cdot B^2 \cdot L}{5} \text{ [kNm/rad]} \tag{A.16}$$

$$k_{\theta l} = \frac{E_k \cdot B \cdot L^2}{5} \text{ [kNm/rad]} \tag{A.17}$$

The springs are equivalent to the rotational axis of the slab shown in figure A.17 below.

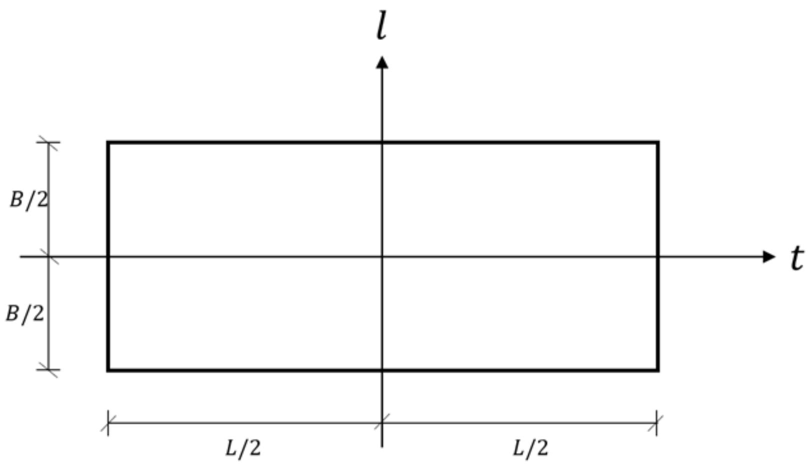

Figure A.17: rotational axis for the springs.

Young's modulus of E_k =100MPa was used in each bridge design. Deriving the vertical line spring k_z is done by the use of parameters derived in equation A.16 and equation A.17 and presented in the formula below.

$$k_z = 0.5(\frac{k_{\theta t}}{I_t} + \frac{k_{\theta l}}{I_l}) \text{ [kNm/rad]} \tag{A.18}$$

The moment of inertia and the footprint of the slab is added to the equation and the stiffness for each bridge is presented in table A.12.

Table A.12: Brigade spring stiffness.

	Brigade Slab Springs				
	base [m]	length [m]	k0t [kNm/rad]	k0l [kNm/rad]	kz kN/m
Bridge 1-1	2	5	4.00E+06	1.00E+07	8.40E+06
Bridge 1-3	2	9	7.20E+06	3.24E+07	1.32E+07
Bridge 1-5	2	14	1.12E+07	7.84E+07	1.92E+07
Bridge 2-1	3	7	1.26E+07	2.94E+07	1.20E+07
Bridge 2-3	3	7	1.26E+07	2.94E+07	1.20E+07
Bridge 2-5	3	7	1.26E+07	2.94E+07	1.20E+07
Bridge 2-2-1	3	7	1.26E+07	2.94E+07	1.20E+07
Bridge 2-2-3	3	7	1.26E+07	2.94E+07	1.20E+07
Bridge 2-2-5	3	7	1.26E+07	2.94E+07	1.20E+07
Bridge 3-1	2	7	5.60E+06	1.96E+07	1.08E+07
Bridge 3-3	3.5	7	1.72E+07	3.43E+07	1.26E+07
Bridge 3-5	5	7	2.24E+07	3.92E+07	1.32E+07
Bridge 4-1	2	7	5.60E+06	1.96E+07	1.08E+07
Bridge 4-3	2	7	5.60E+06	1.96E+07	1.08E+07
Bridge 4-5	2	7	5.60E+06	1.96E+07	1.08E+07
Bridge 5-1	2	5	4.00E+06	1.00E+07	8.40E+06
Bridge 5-3	2	5	4.00E+06	1.00E+07	8.40E+06
Bridge 5-5	2	5	4.00E+06	1.00E+07	8.40E+06
Bridge 6-1	2	5	2.00E+06	5.00E+06	4.20E+06
Bridge 6-3	2	5	4.00E+06	1.00E+07	8.40E+06
Bridge 6-5	2	5	6.00E+06	1.50E+07	1.26E+07
Bridge 7-1	2	5	4.00E+06	1.00E+07	8.40E+06
Bridge 7-3	2	5	4.00E+06	1.00E+07	8.40E+06
Bridge 7-5	2	5	4.00E+06	1.00E+07	8.40E+06

A.8 Bridge designs

In this chapter the various Bridge design models are presented. Not that the dimensions can also been seen in tables 3.1 -3.8.

A.8.1 Bridge 1

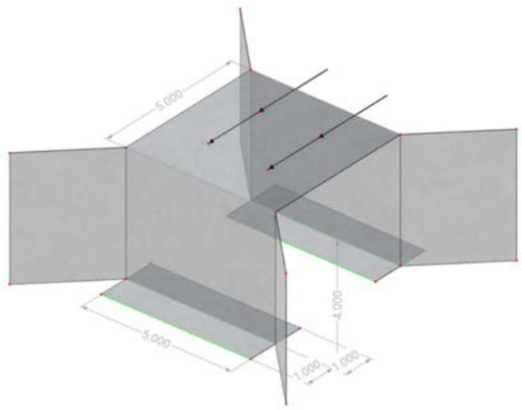

Figure A.18: Bridge design for Bridge 1-1.

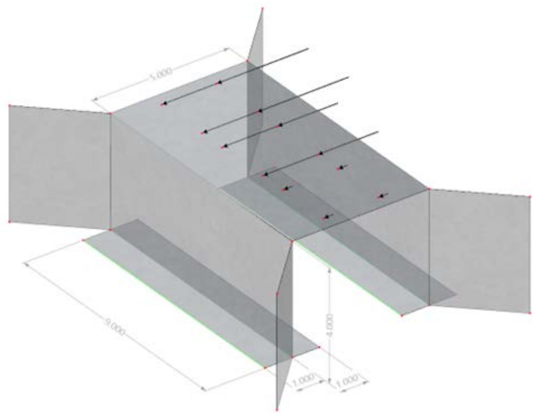

Figure A.19: Bridge design for Bridge 1-3.

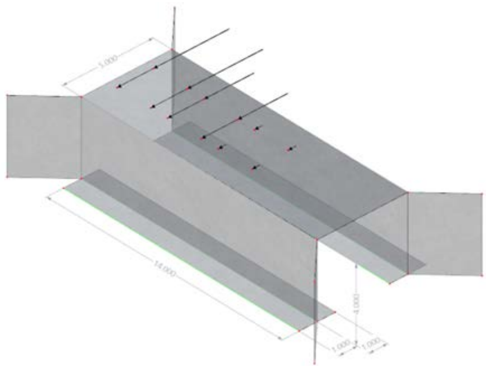

Figure A.20: Bridge design for Bridge 1-5.

A.8.2 Bridge 2

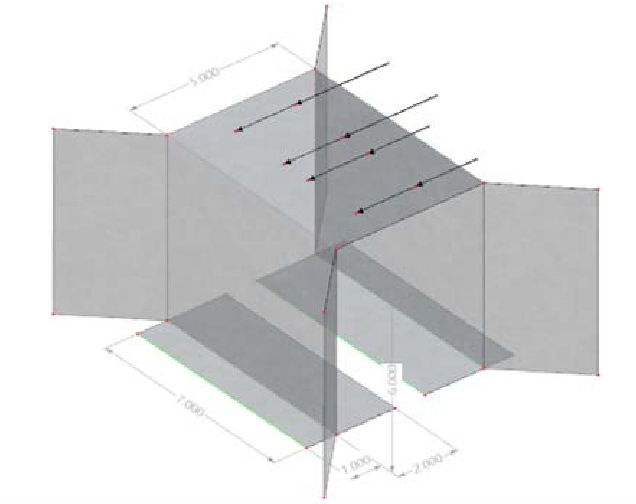

Figure A.21: Bridge design for Bridge 2-1.

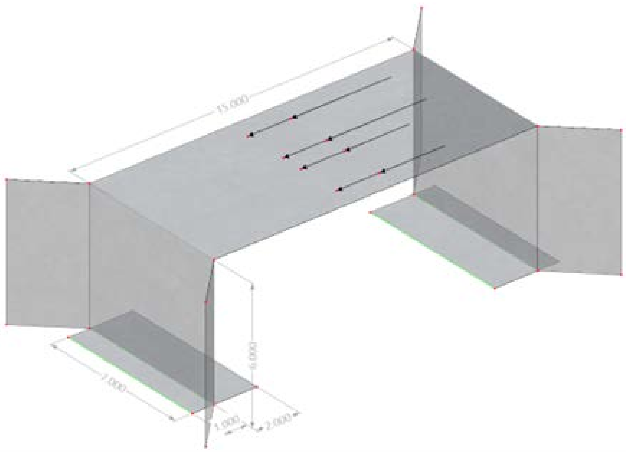

Figure A.22: Bridge design for Bridge 2-3.

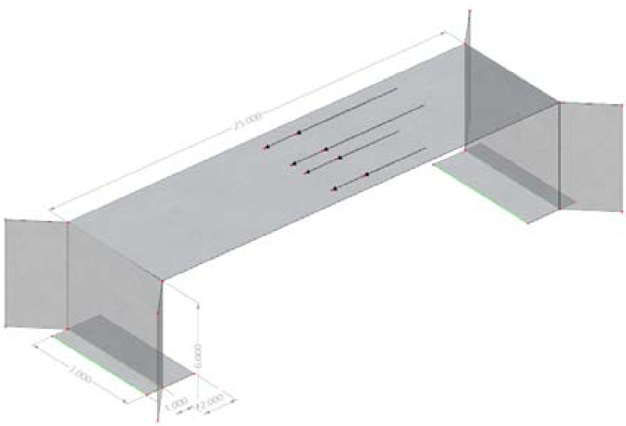

Figure A.23: Bridge design for Bridge 2-5.

A.8.3 Bridge 2-2

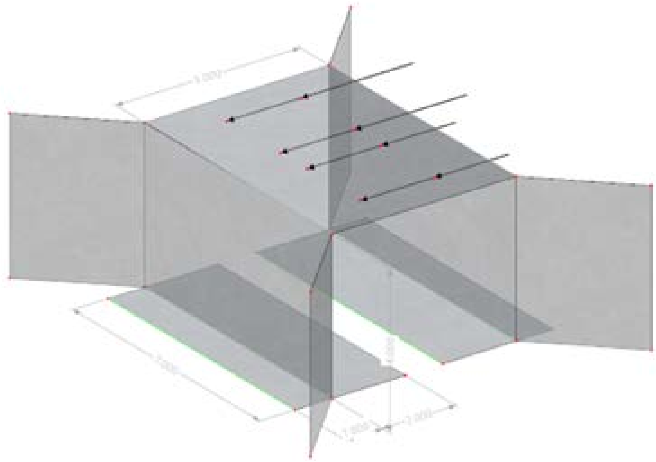

Figure A.24: Bridge design for Bridge 2-2-1.

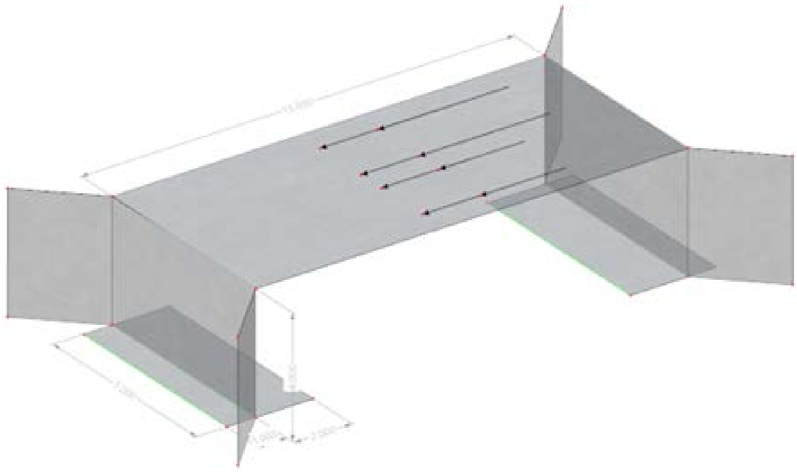

Figure A.25: Bridge design for Bridge 2-2-3.

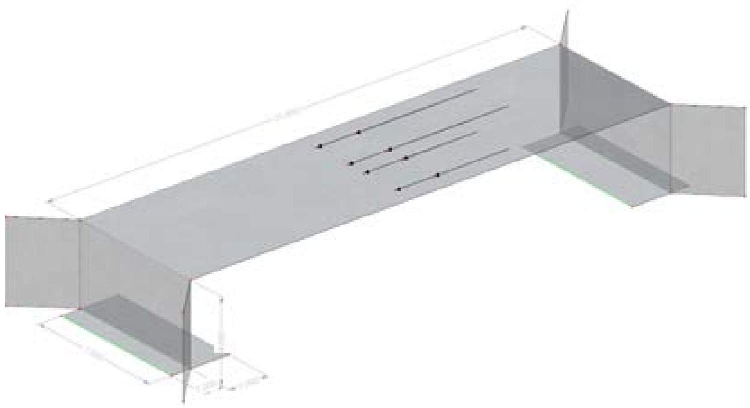

Figure A.26: Bridge design for Bridge 2-2-5.

A.8.4 Bridge 3

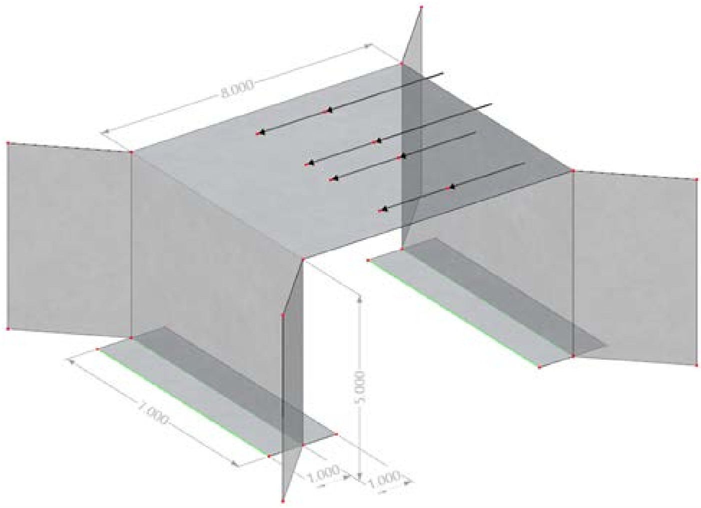

Figure A.27: Bridge design for Bridge 3-1.

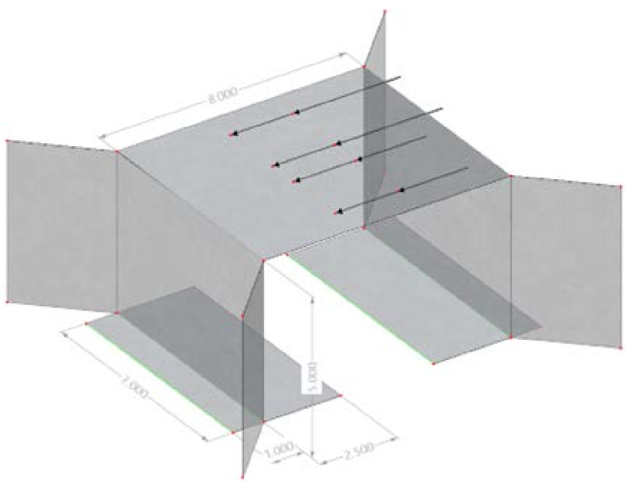

Figure A.28: Bridge design for Bridge 3-3.

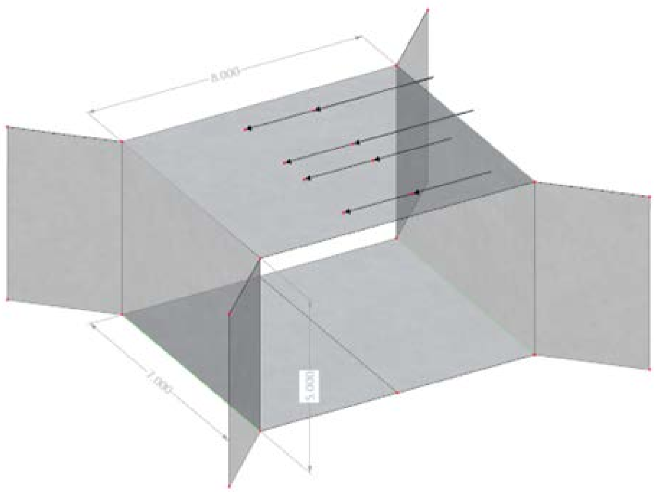

Figure A.29: Bridge design for Bridge 3-5.

A.8.5 Bridge 4

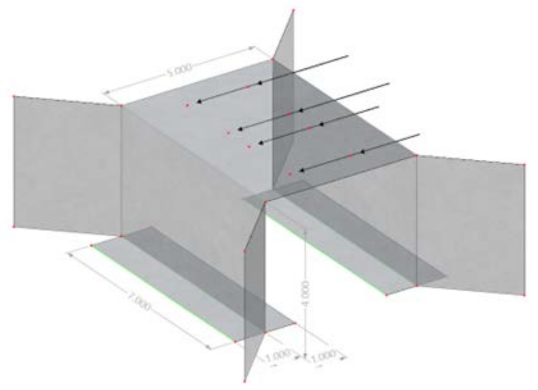

Figure A.30: Bridge design for Bridge 4-1.

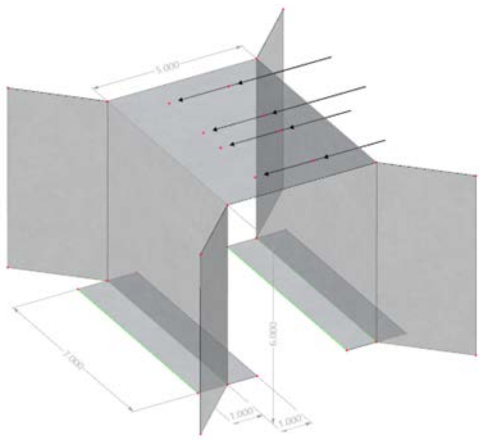

Figure A.31: Bridge design for Bridge 4-3.

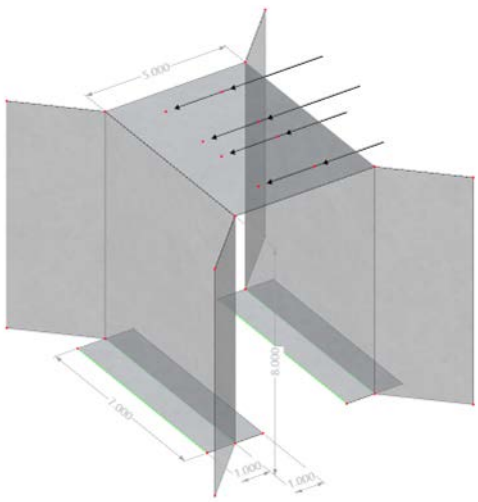

Figure A.32: Bridge design for Bridge 4-5.

A.8.6 Bridge 5, 6 and 7

The Bridge design for all these models are of the same geometry as for Bridge 1-1 (figure A.18). For Bridge 5, the thickness of the abutment wall varies, please see table 3.6. While the soil properties varies for Bridge 6 and Bridge 7, please see table 3.7 and table 3.8.

A.9 Sectional forces and deformations

A.9.1 Bridge 1

Horizontal deformation on the top of the abutment wall

Figure A.33: Top horizontal deformation on the abutment wall for Bridge 1-1.

Figure A.34: Top horizontal deformation on the abutment wall for Bridge 1-3.

Figure A.35: Top horizontal deformation on the abutment wall for Bridge 1-5.

Moments in horizontal result section 1

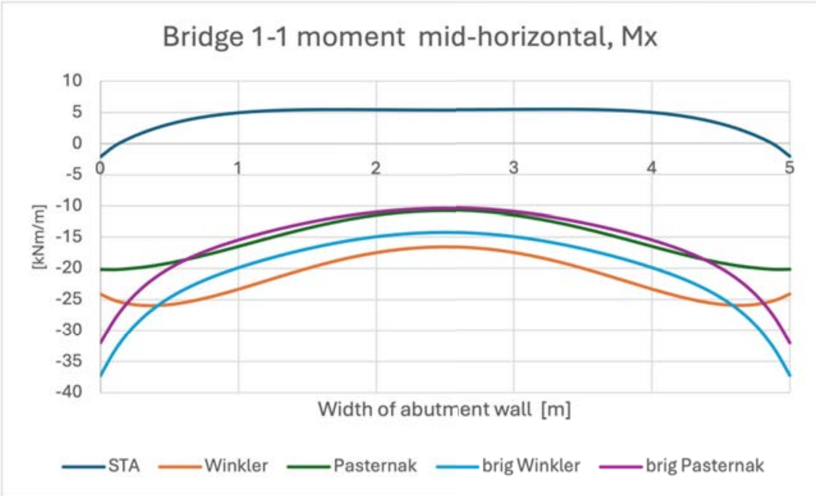

Figure A.36: Moment M_x, in horizontal result section 1, Bridge 1-1.

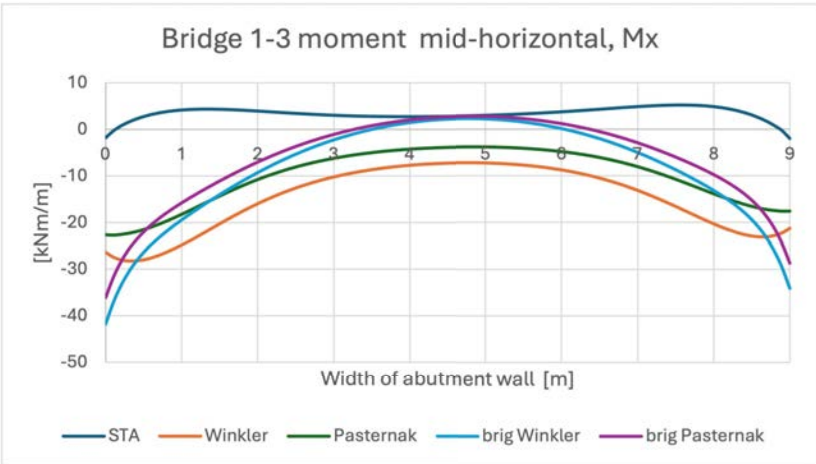

Figure A.37: Moment M_x, in horizontal result section 1, Bridge 1-3.

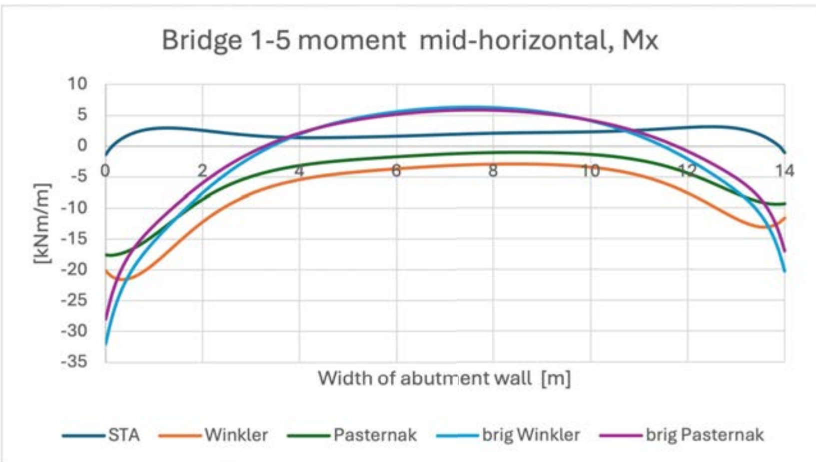

Figure A.38: Moment M_x, in horizontal result section 1, Bridge 1-5.

Shear forces in horizontal result section 1

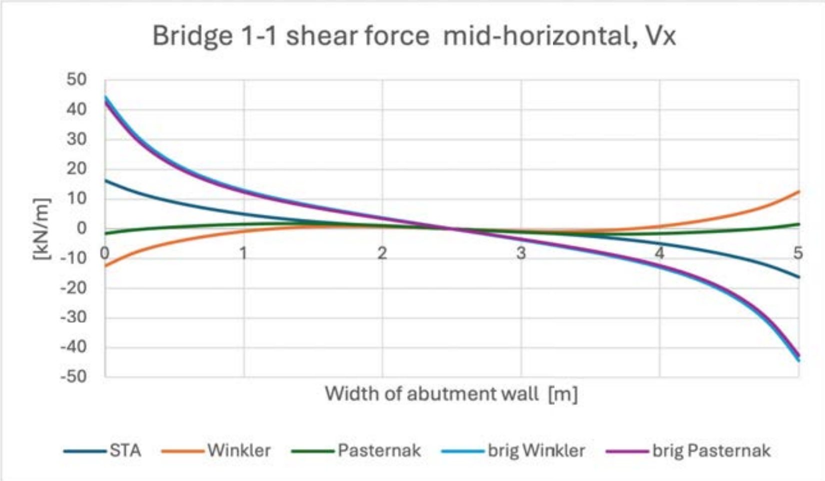

Figure A.39: Shear force V_x, in horizontal result section 1, Bridge 1-1.

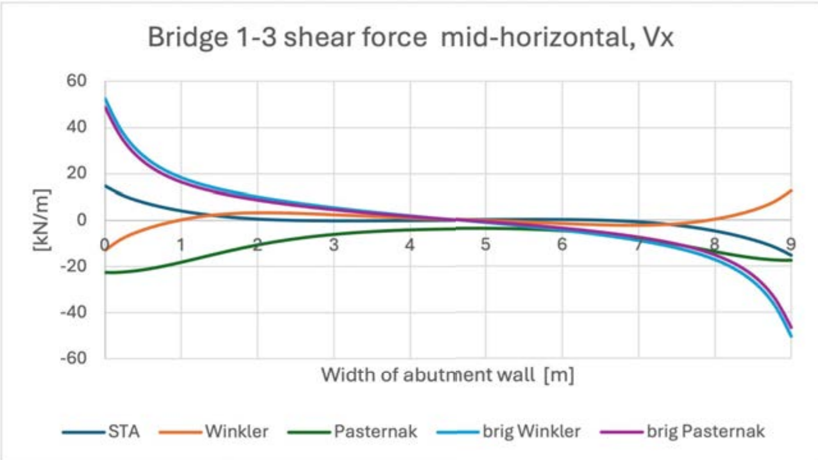

Figure A.40: Shear force V_x, in horizontal result section 1, Bridge 1-3.

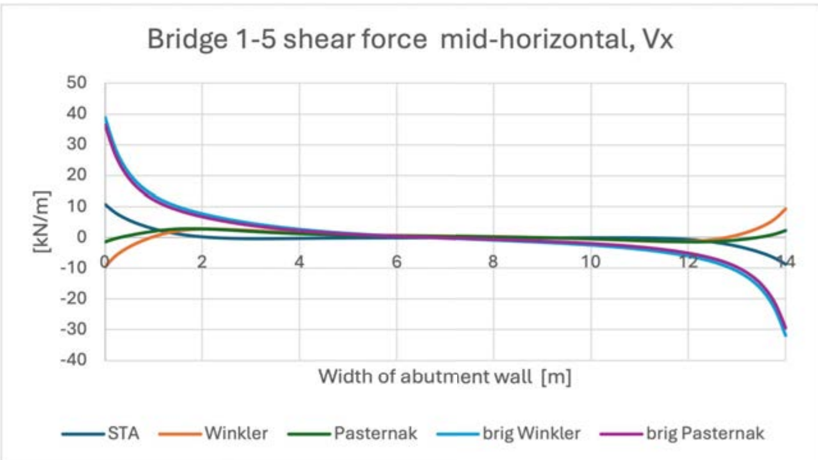

Figure A.41: Shear force V_x, in horizontal result section 1, Bridge 1-5.

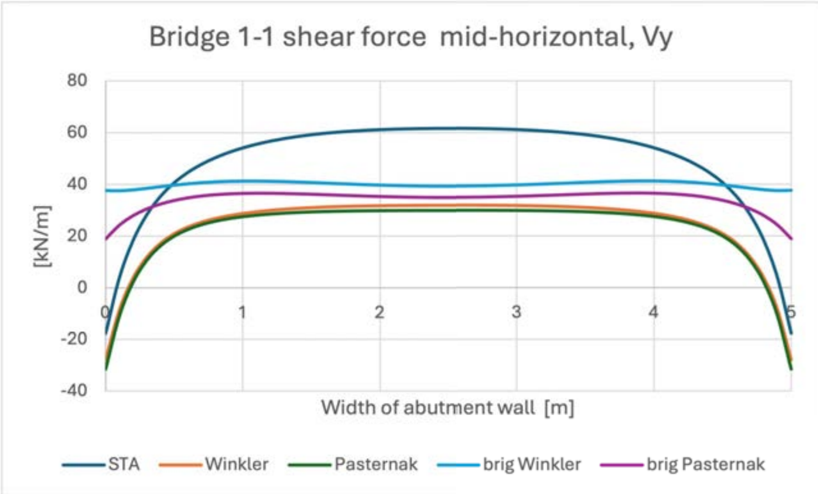

Figure A.42: Shear force V_y, in horizontal result section 1, Bridge 1-1.

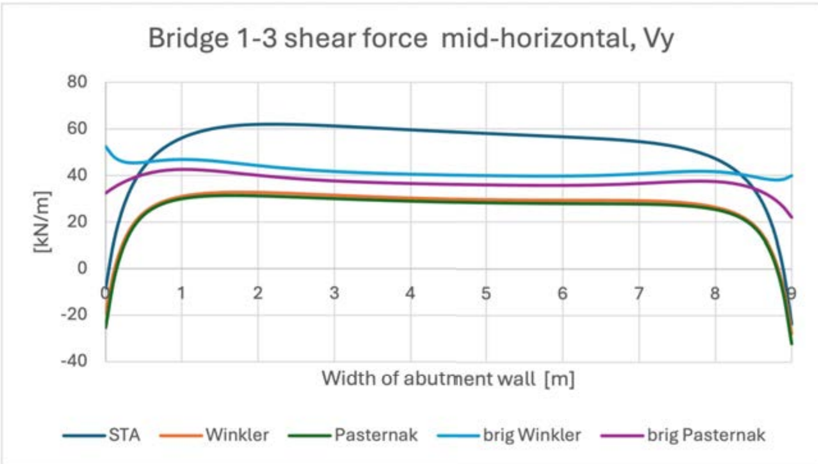

Figure A.43: Shear force V_y, in horizontal result section 1, Bridge 1-3.

Figure A.44: Shear force V_y, in horizontal result section 1, Bridge 1-5.

Moments in horizontal result section 2

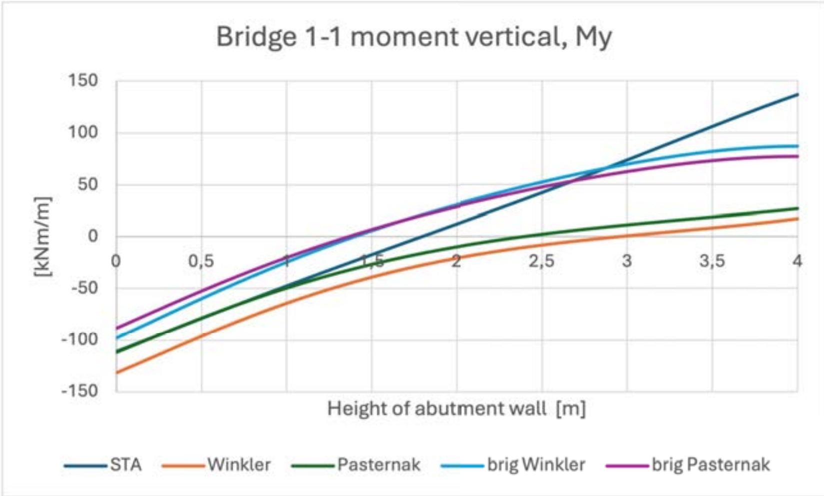

Figure A.45: Moment M_y, in horizontal result section 2, Bridge 1-1.

Figure A.46: Moment M_y, in horizontal result section 2, Bridge 1-3.

Figure A.47: Moment M_y, in horizontal result section 2, Bridge 1-5.

Shear forces in horizontal result section 2

Figure A.48: Shear force V_y, in horizontal result section 2, Bridge 1-1.

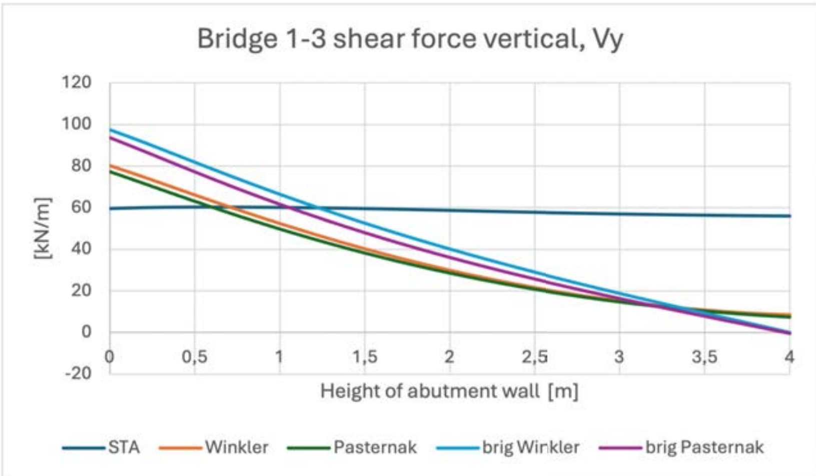

Figure A.49: Shear force V_y, in horizontal result section 2, Bridge 1-3.

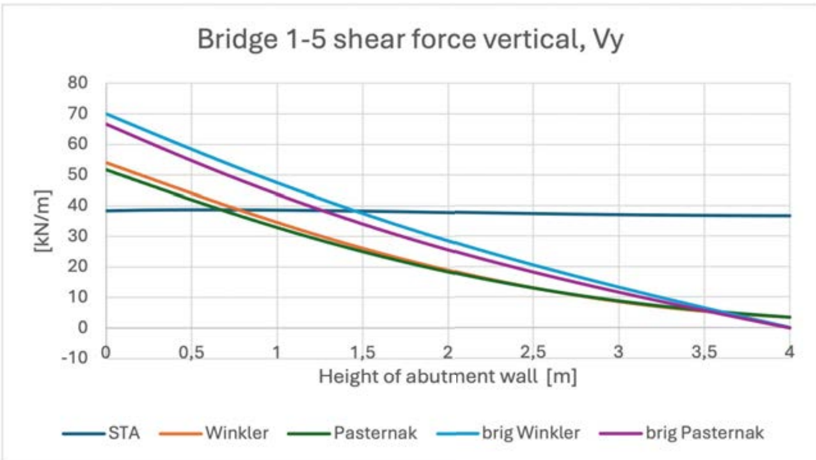

Figure A.50: Shear force V_y, in horizontal result section 2, Bridge 1-5.

A.9.2 Bridge 2

Horizontal deformation on the top of the abutment wall

Figure A.51: Top horizontal deformation on the abutment wall for Bridge 2-1.

Figure A.52: Top horizontal deformation on the abutment wall for Bridge 2-3

Figure A.53: Top horizontal deformation on the abutment wall for Bridge 2-5

Moments in horizontal result section 1

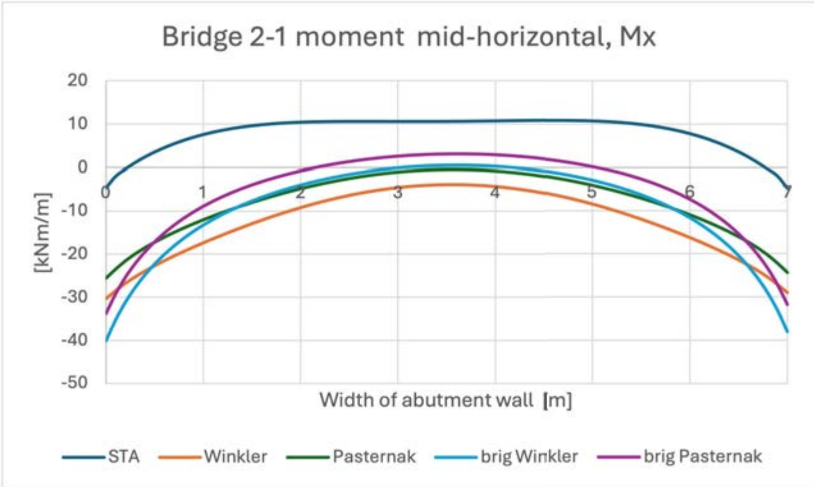

Figure A.54: Moment M_x, in horizontal result section 1, Bridge 2-1.

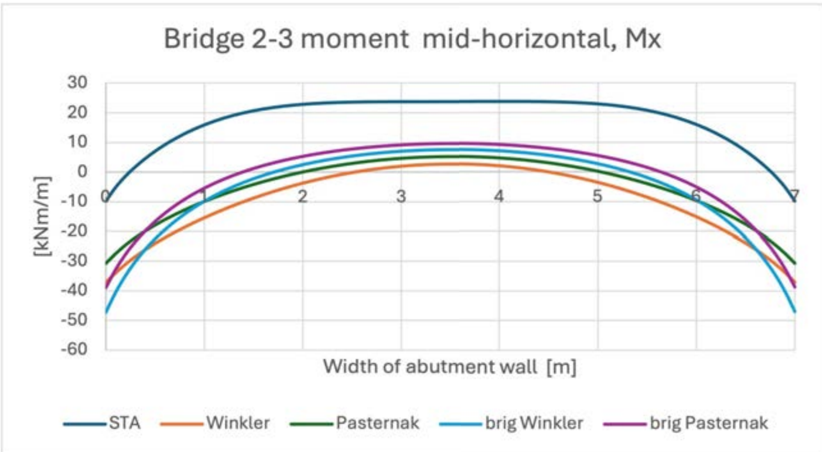

Figure A.55: Moment M_x, in horizontal result section 1, Bridge 2-3.

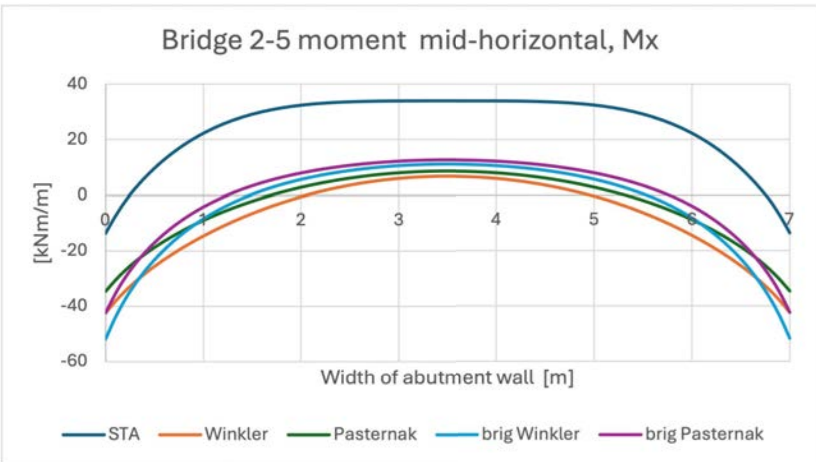

Figure A.56: Moment M_x, in horizontal result section 1, Bridge 2-5.

Shear forces in horizontal result section 1

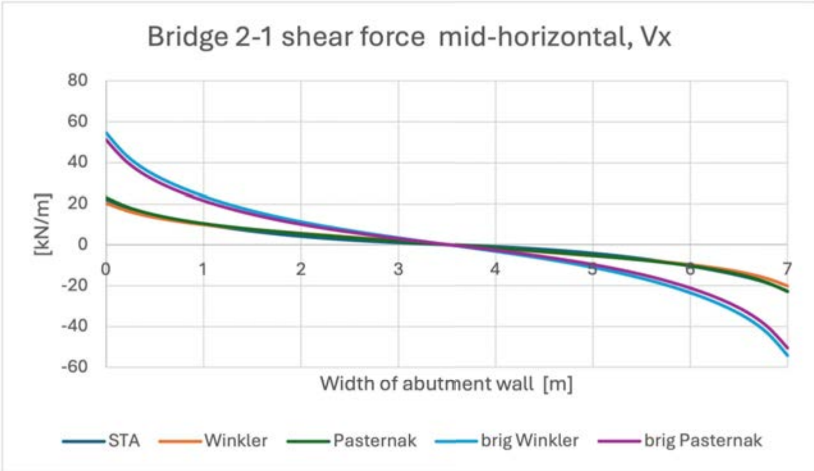

Figure A.57: Shear force V_x, in horizontal result section 1, Bridge 2-1.

Figure A.58: Shear force V_x, in horizontal result section 1, Bridge 2-3.

Figure A.59: Shear force V_x, in horizontal result section 1, Bridge 2-5.

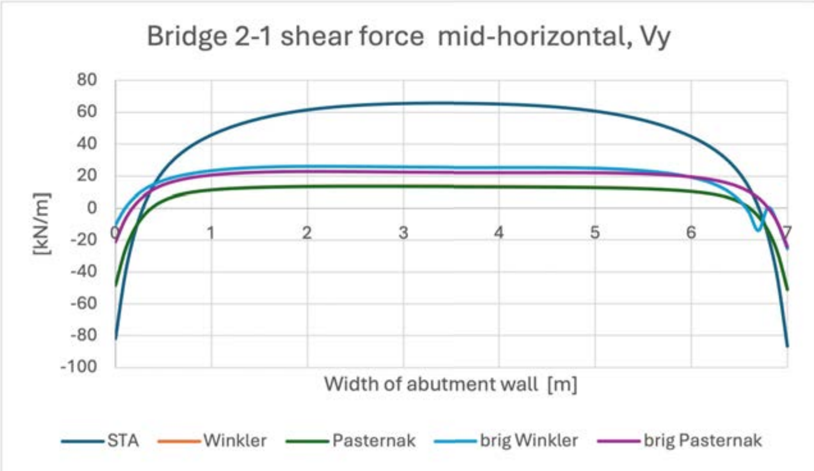

Figure A.60: Shear force V_y, in horizontal result section 1, Bridge 2-1.

Figure A.61: Shear force V_y, in horizontal result section 1, Bridge 2-3.

Figure A.62: Shear force V_y, in horizontal result section 1, Bridge 2-5.

Moments in horizontal result section 2

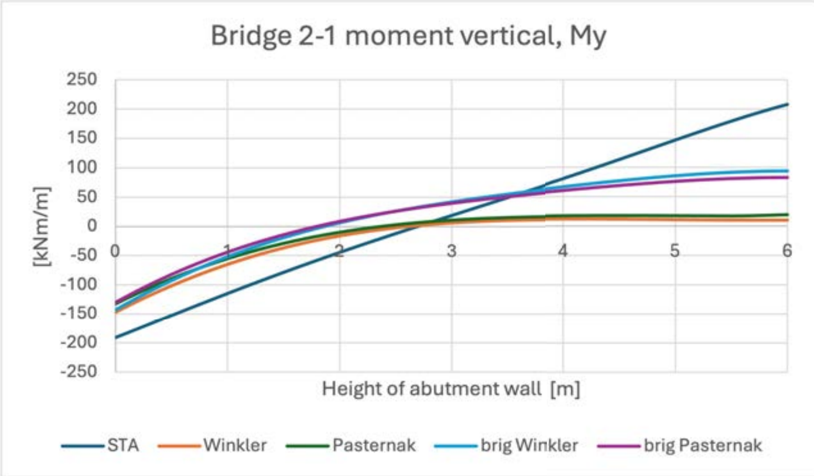

Figure A.63: Moment M_y, in horizontal result section 2, Bridge 2-1.

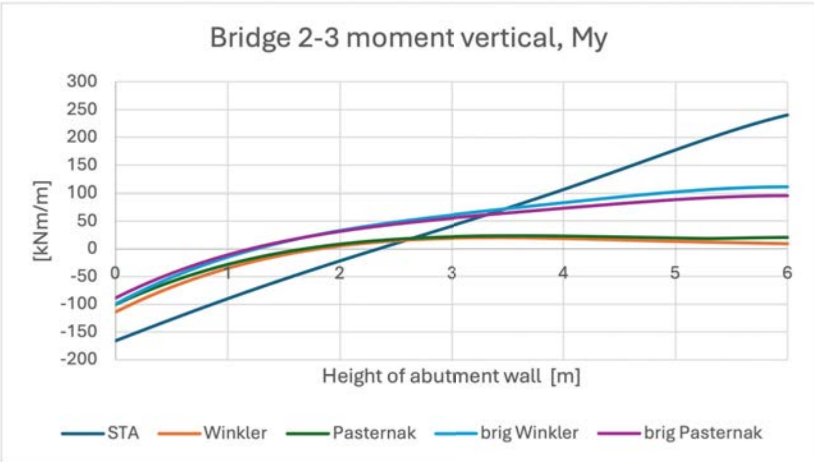

Figure A.64: Moment M_y, in horizontal result section 2, Bridge 2-3.

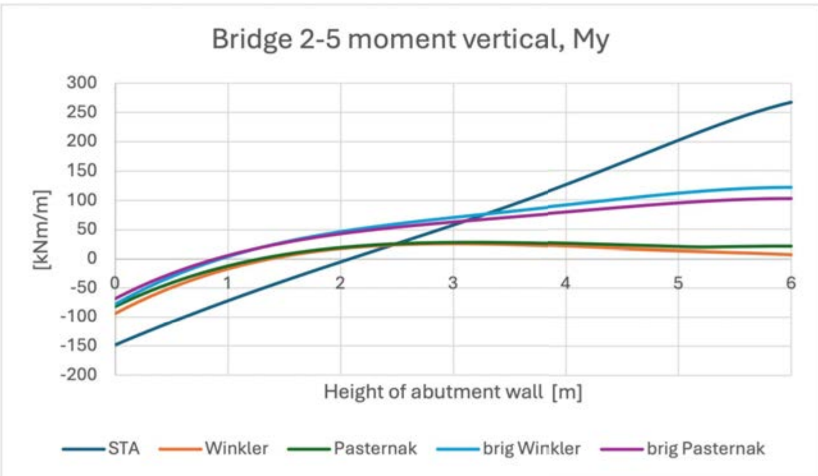

Figure A.65: Moment M_y, in horizontal result section 2, Bridge 2-5.

Shear forces in horizontal result section 2

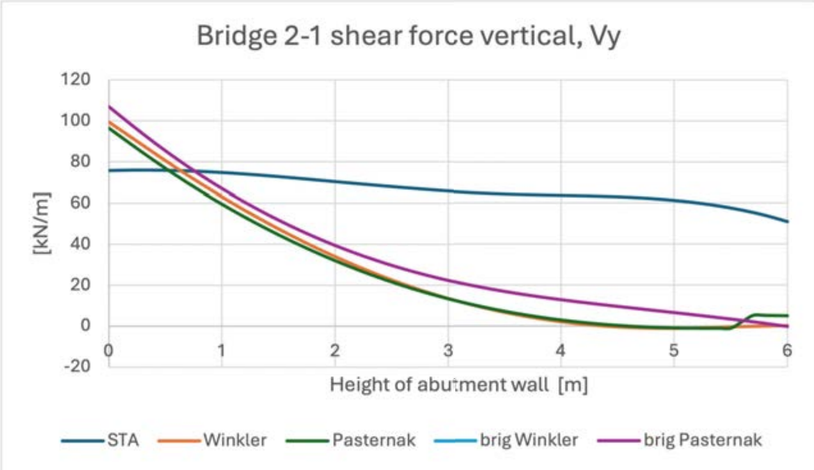

Figure A.66: Shear force V_y, in horizontal result section 2, Bridge 2-1.

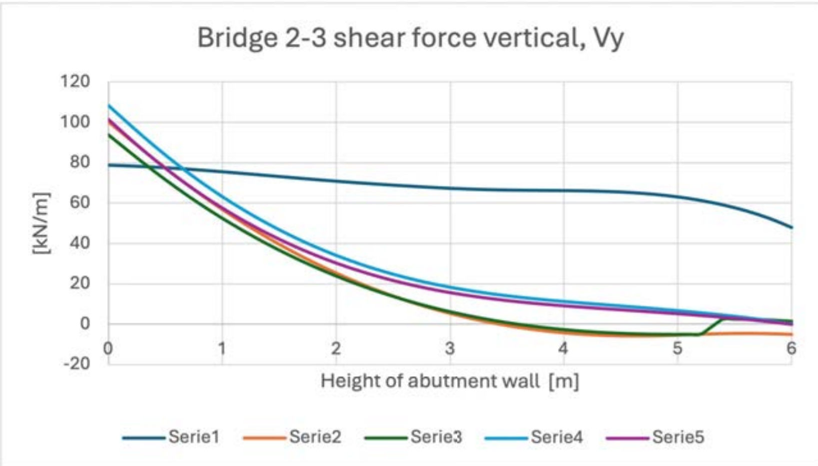

Figure A.67: Shear force V_y, in horizontal result section 2, Bridge 2-3.

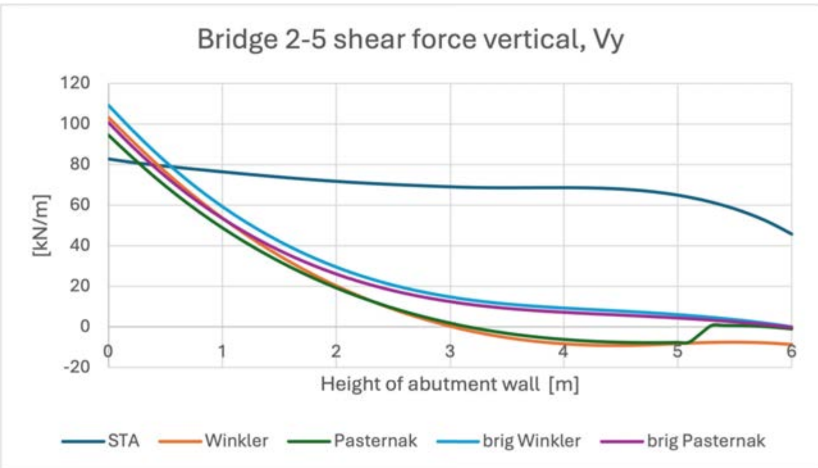

Figure A.68: Shear force V_y, in horizontal result section 2, Bridge 2-5.

A.9.3 Bridge 2.2

Horizontal deformation on the top of the abutment wall

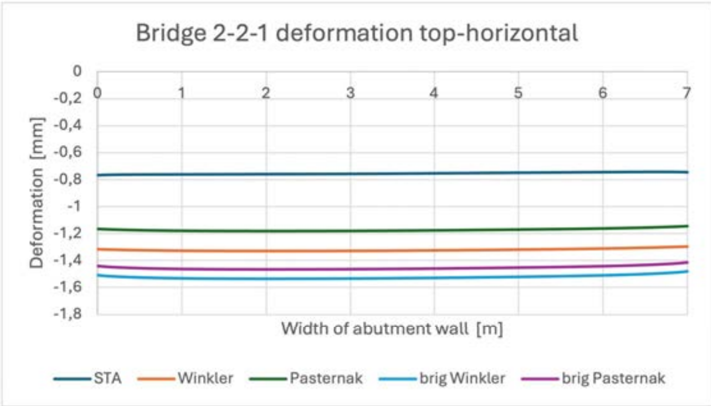

Figure A.69: Top horizontal deformation on the abutment wall for Bridge 2-2-1.

Figure A.70: Top horizontal deformation on the abutment wall for Bridge 2-2-3.

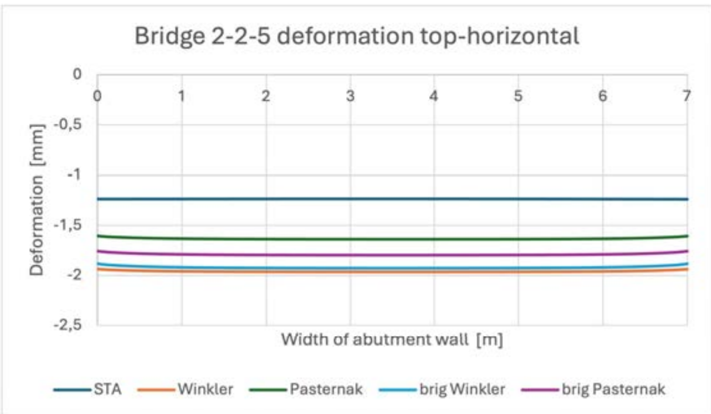

Figure A.71: Top horizontal deformation on the abutment wall for Bridge 2-2-5.

Moments in horizontal result section 1

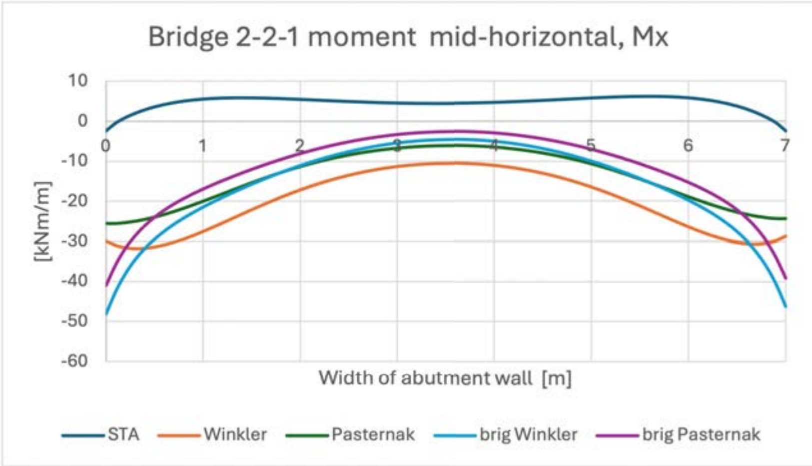

Figure A.72: Moment M_x, in horizontal result section 1, Bridge 2-2-1.

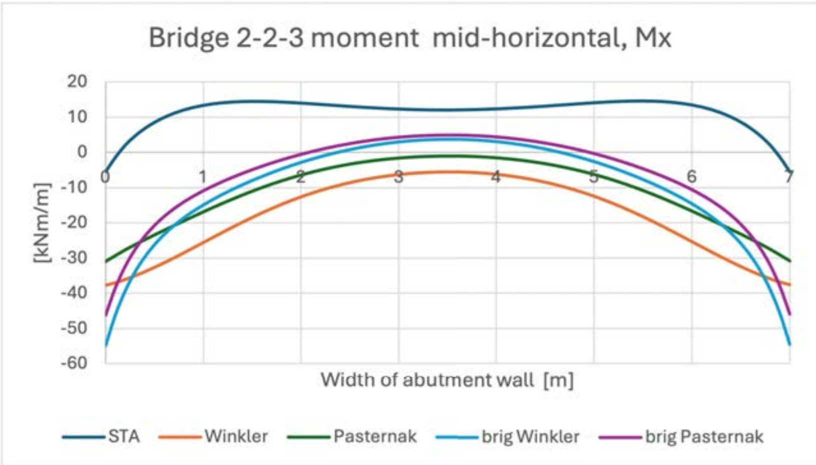

Figure A.73: Moment M_x, in horizontal result section 1, Bridge 2-2-3.

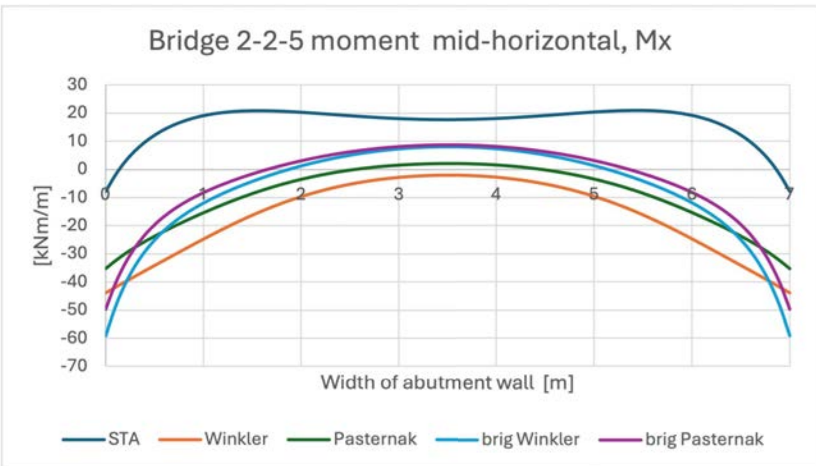

Figure A.74: Moment M_x, in horizontal result section 1, Bridge 2-2-5.

Shear forces in horizontal result section 1

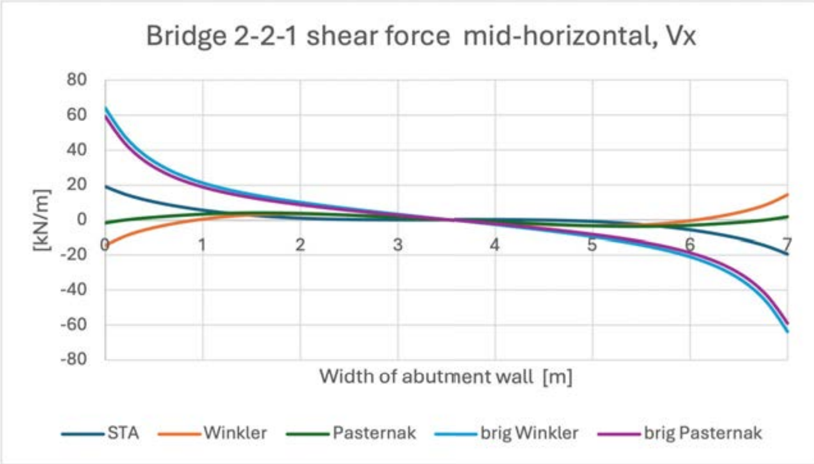

Figure A.75: Shear force V_x, in horizontal result section 1, Bridge 2-2-1.

Figure A.76: Shear force V_x, in horizontal result section 1, Bridge 2-2-3.

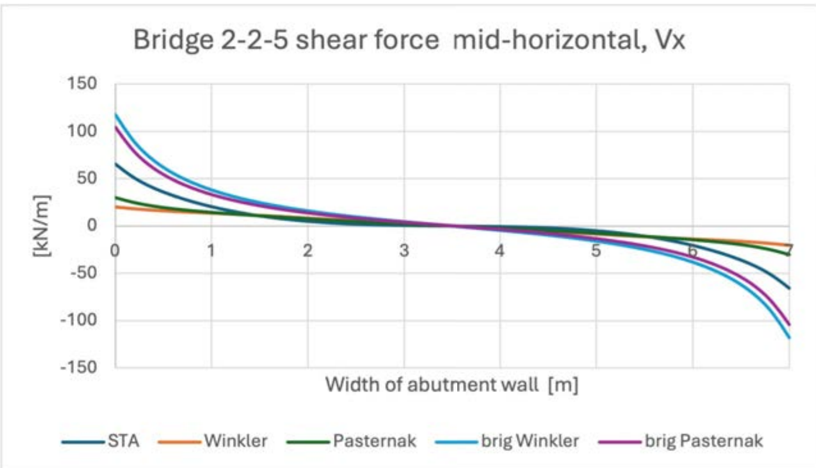

Figure A.77: Shear force V_x, in horizontal result section 1, Bridge 2-2-5.

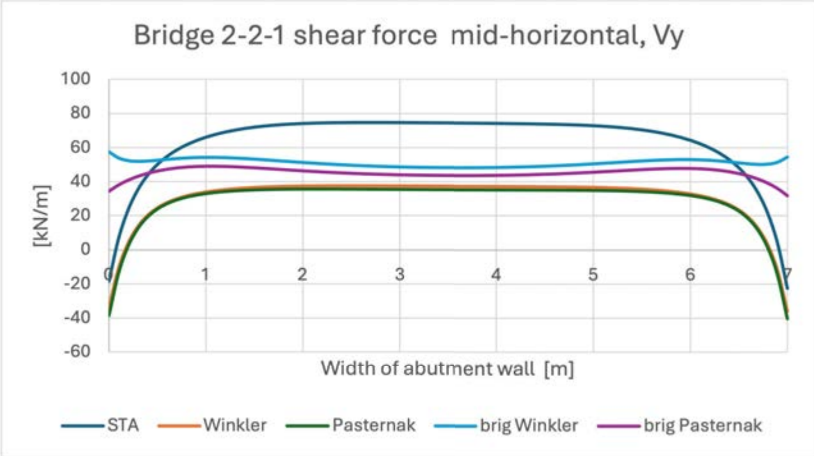

Figure A.78: Shear force V_y, in horizontal result section 1, Bridge 2-2-1.

Figure A.79: Shear force V_y, in horizontal result section 1, Bridge 2-2-3.

Figure A.80: Shear force V_y, in horizontal result section 1, Bridge 2-2-5.

Moments in horizontal result section 2

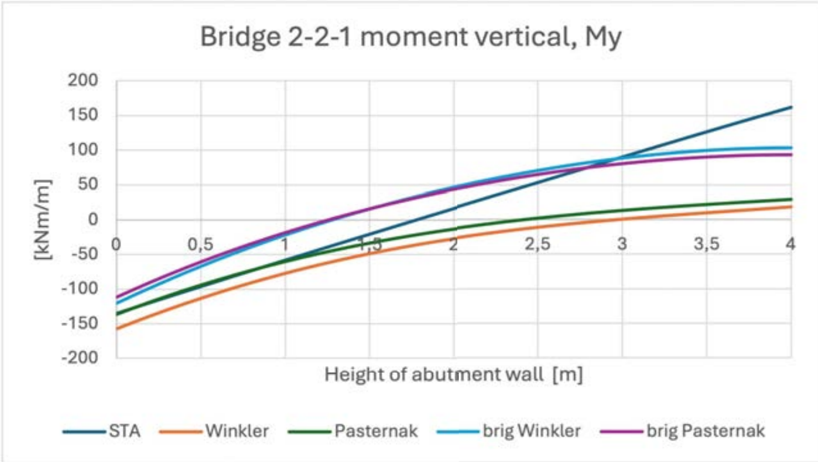

Figure A.81: Moment M_y, in horizontal result section 2, Bridge 2-2-1.

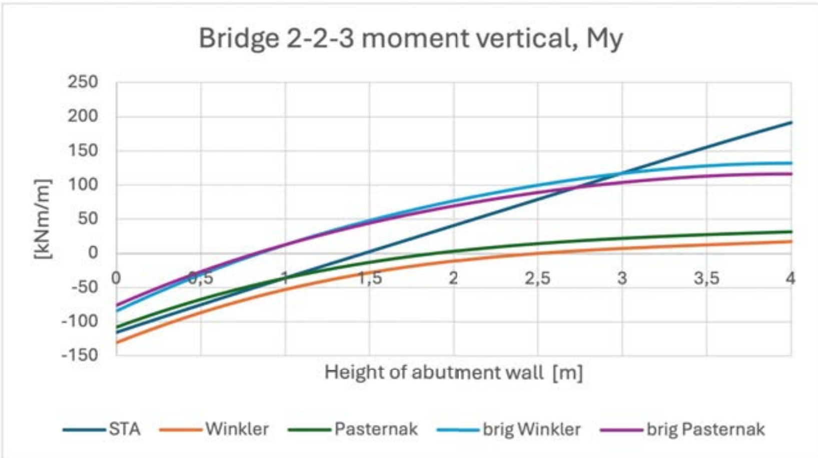

Figure A.82: Moment M_y, in horizontal result section 2, Bridge 2-2-3.

Figure A.83: Moment M_y, in horizontal result section 2, Bridge 2-2-5.

Shear forces in horizontal result section 2

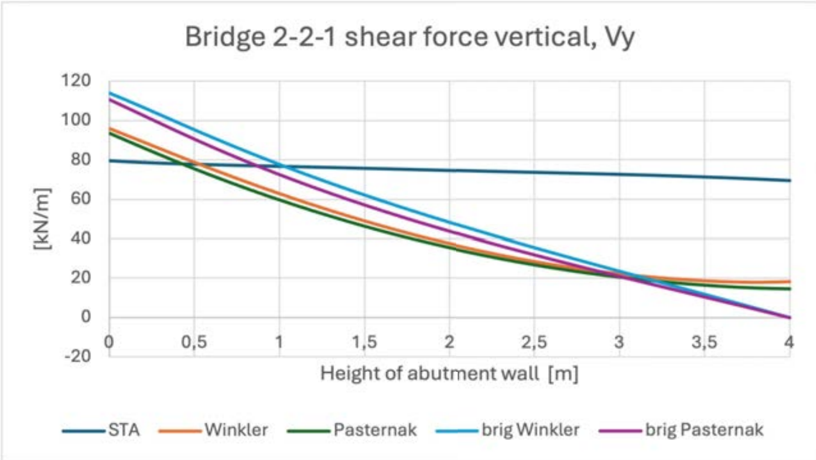

Figure A.84: Shear force V_y, in horizontal result section 2, Bridge 2-2-1.

Figure A.85: Shear force V_y, in horizontal result section 2, Bridge 2-2-3.

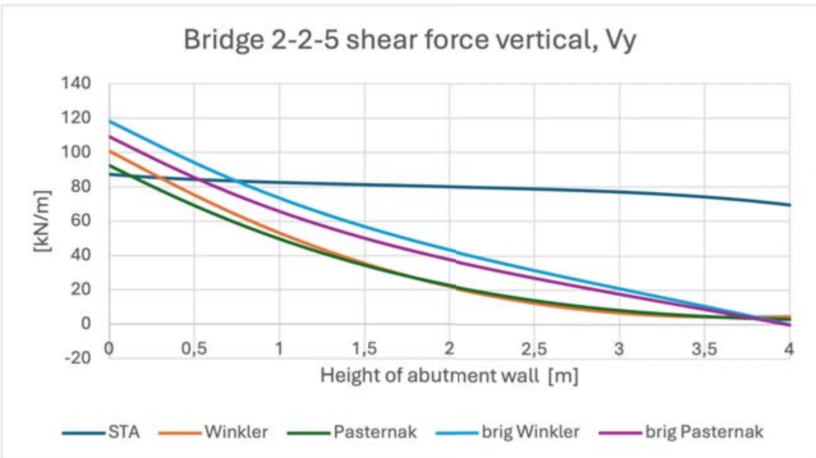

Figure A.86: Shear force V_y, in horizontal result section 2, Bridge 2-2-5.

A.9.4 Bridge 3

Horizontal deformation on the top of the abutment wall

Figure A.87: Top horizontal deformation on the abutment wall for Bridge 3-1.

Figure A.88: Top horizontal deformation on the abutment wall for Bridge 3-3.

Figure A.89: Top horizontal deformation on the abutment wall for Bridge 3-5.

Moments in horizontal result section 1

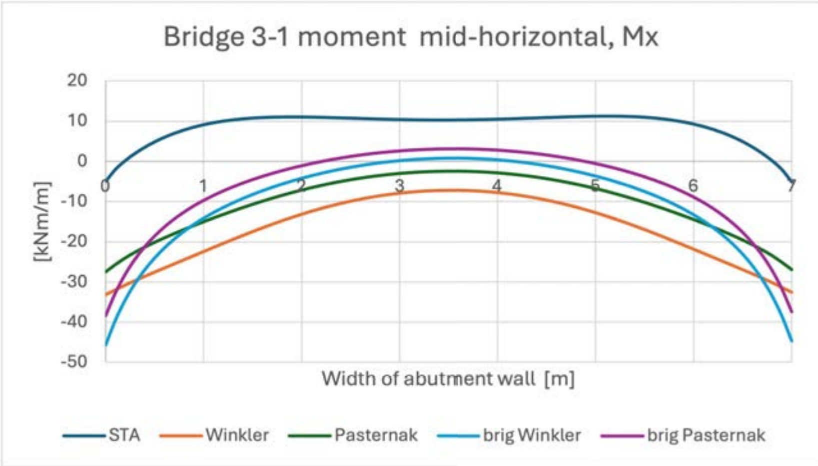

Figure A.90: Moment M_x, in horizontal result section 1, Bridge 3-1.

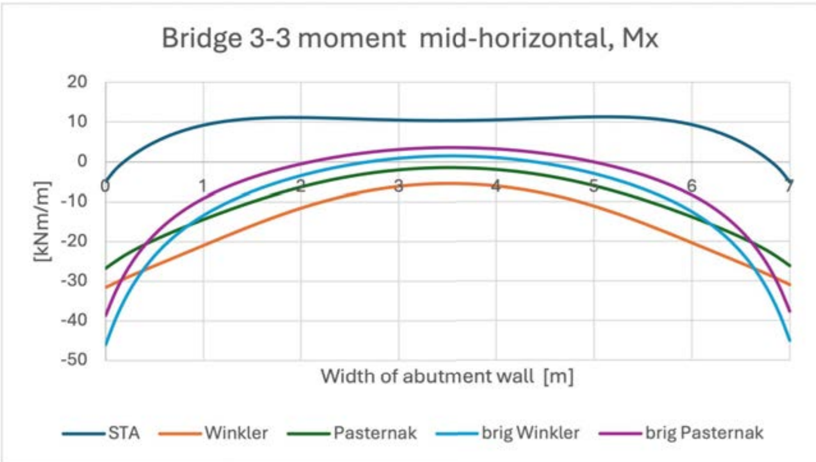

Figure A.91: Moment M_x, in horizontal result section 1, Bridge 3-3.

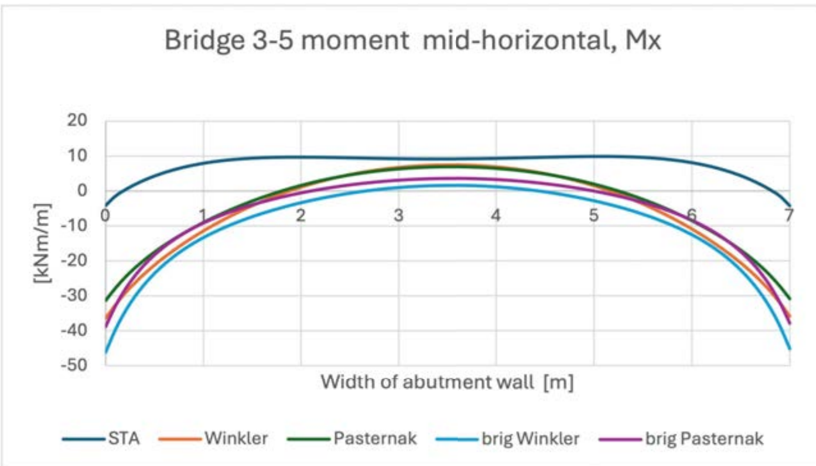

Figure A.92: Moment M_x, in horizontal result section 1, Bridge 3-5.

Shear forces in horizontal result section 1

Figure A.93: Shear force V_x, in horizontal result section 1, Bridge 3-1.

Figure A.94: Shear force V_x, in horizontal result section 1, Bridge 3-3.

Figure A.95: Shear force V_x, in horizontal result section 1, Bridge 3-5.

Figure A.96: Shear force V_y, in horizontal result section 1, Bridge 3-1.

Figure A.97: Shear force V_y, in horizontal result section 1, Bridge 3-3.

Figure A.98: Shear force V_y, in horizontal result section 1, Bridge 3-5.

Moments in horizontal result section 2

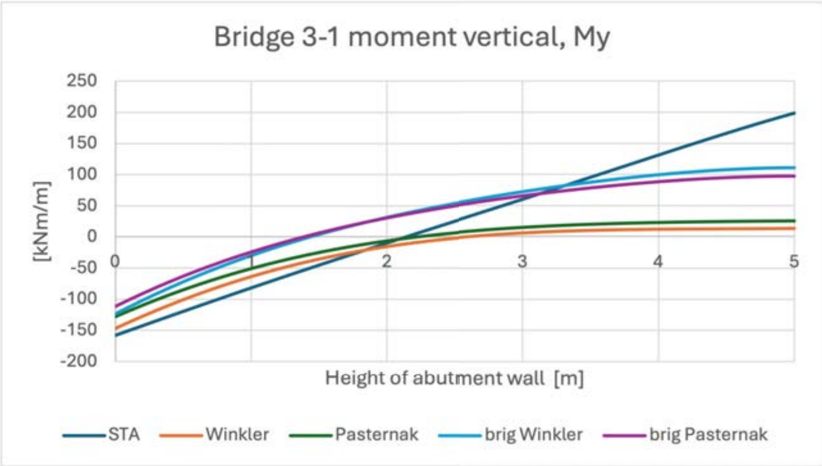

Figure A.99: Moment M_y, in horizontal result section 2, Bridge 3-1.

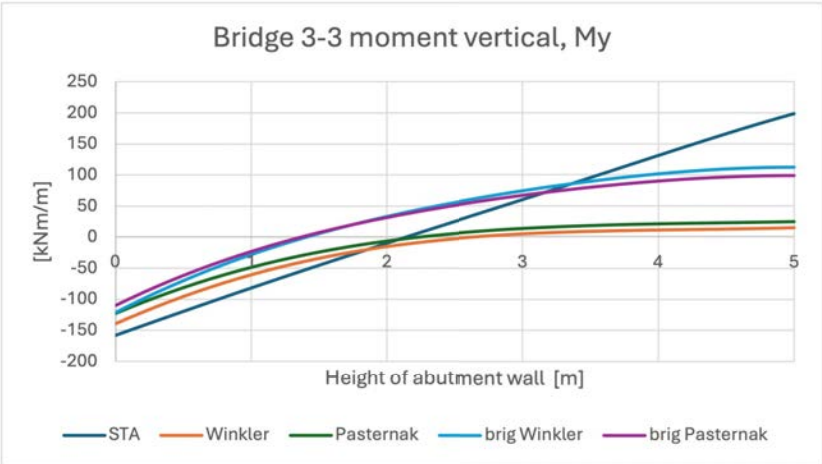

Figure A.100: Moment M_y, in horizontal result section 2, Bridge 3-3.

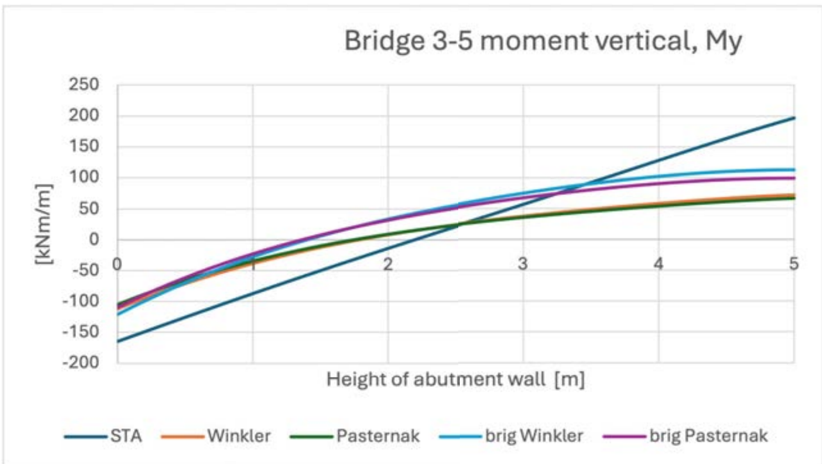

Figure A.101: Moment M_y, in horizontal result section 2, Bridge 3-5.

Shear forces in horizontal result section 2

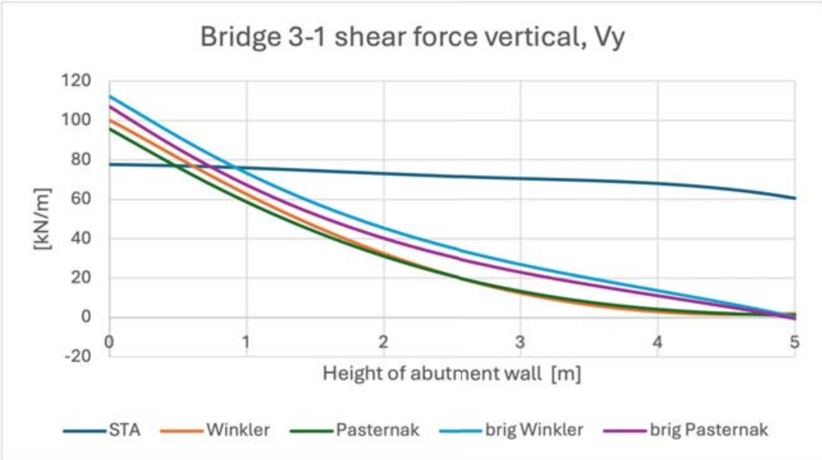

Figure A.102: Shear force V_y, in horizontal result section 2, Bridge 3-1.

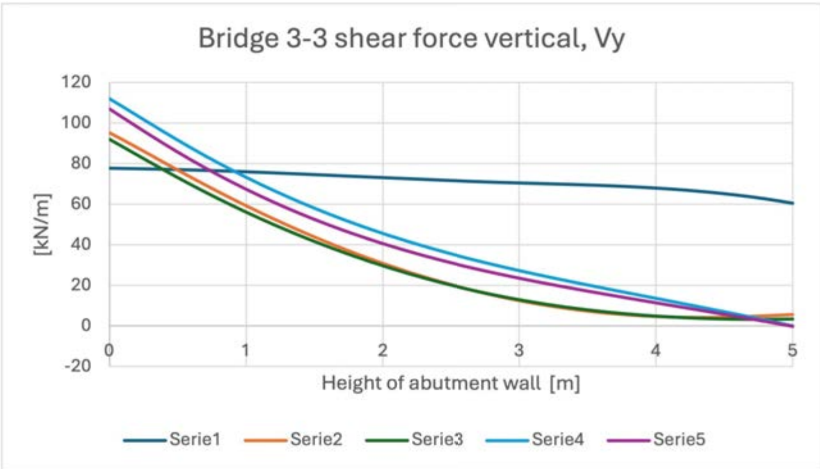

Figure A.103: Shear force V_y, in horizontal result section 2, Bridge 3-3.

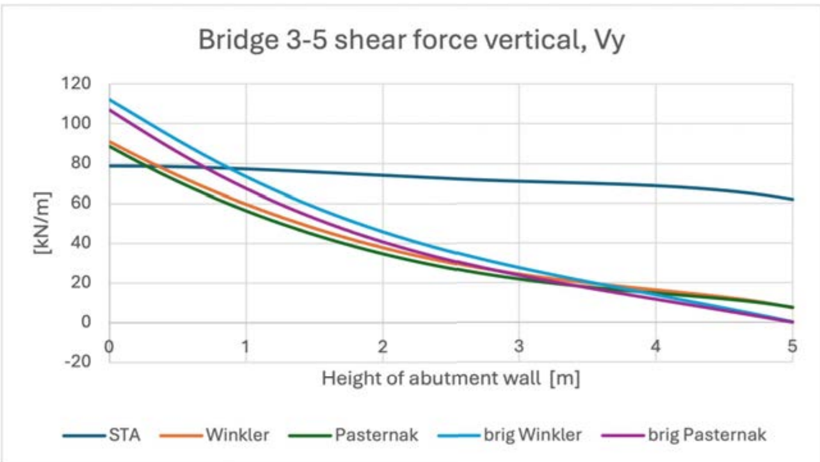

Figure A.104: Shear force V_y, in horizontal result section 2, Bridge 3-5.

A.9.5 Bridge 4

Horizontal deformation on the top of the abutment wall

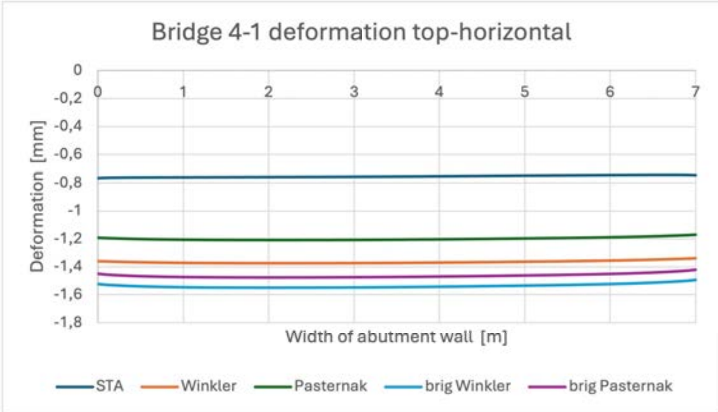

Figure A.105: Top horizontal deformation on the abutment wall for Bridge 4-1.

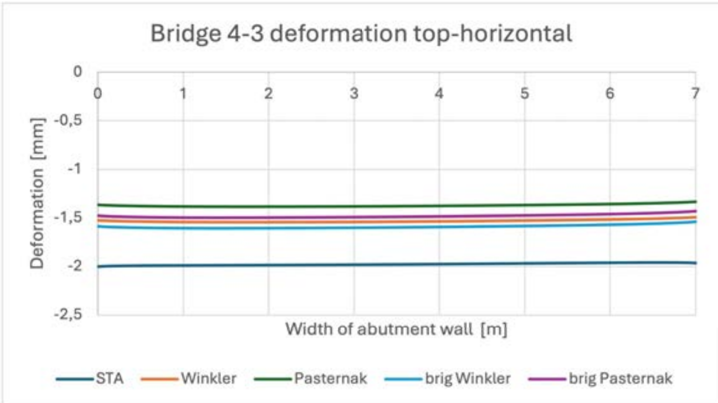

Figure A.106: Top horizontal deformation on the abutment wall for Bridge 4-3.

Figure A.107: Top horizontal deformation on the abutment wall for Bridge 4-5.

Moments in horizontal result section 1

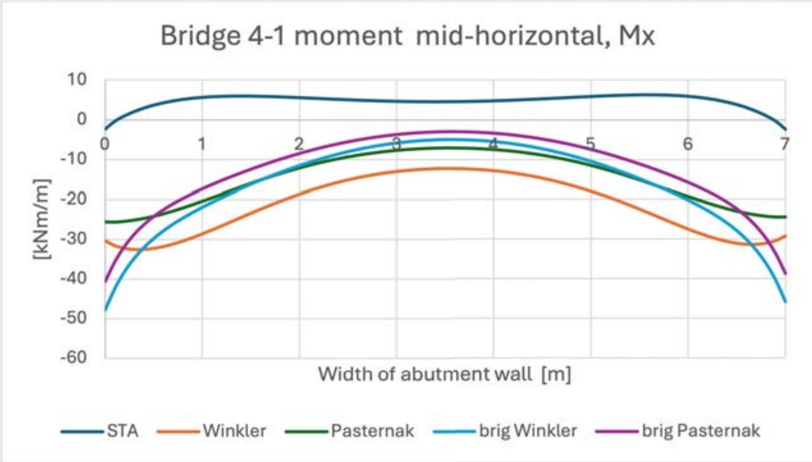

Figure A.108: Moment M_x, in horizontal result section 1, Bridge 4-1.

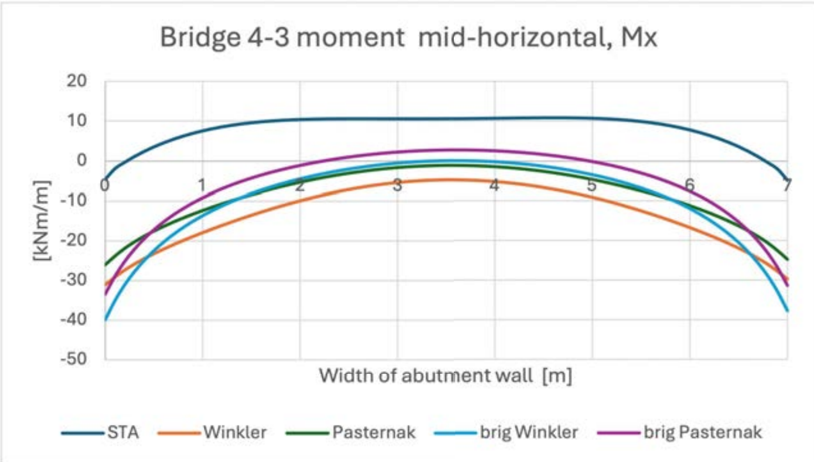

Figure A.109: Moment M_x, in horizontal result section 1, Bridge 4-3.

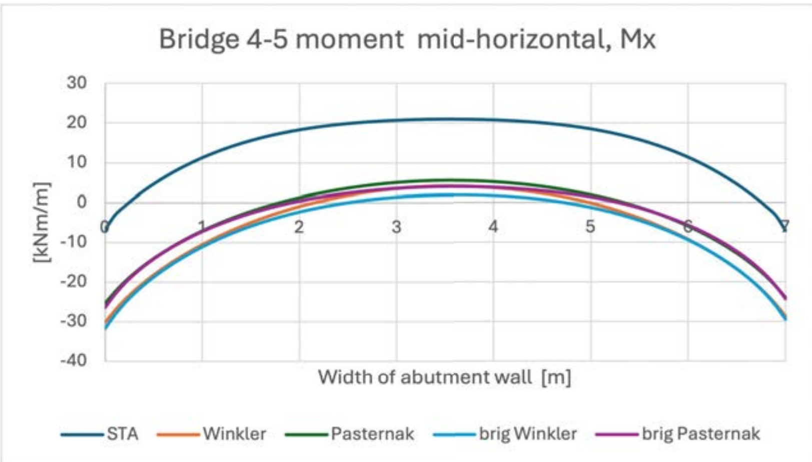

Figure A.110: Moment M_x, in horizontal result section 1, Bridge 4-5.

Shear forces in horizontal result section 1

Figure A.111: Shear force V_x, in horizontal result section 1, Bridge 4-1.

Figure A.112: Shear force V_x, in horizontal result section 1, Bridge 4-3.

Figure A.113: Shear force V_x, in horizontal result section 1, Bridge 4-5.

Figure A.114: Shear force V_y, in horizontal result section 1, Bridge 4-1.

Figure A.115: Shear force V_y, in horizontal result section 1, Bridge 4-3.

Figure A.116: Shear force V_y, in horizontal result section 1, Bridge 4-5.

Moments in horizontal result section 2

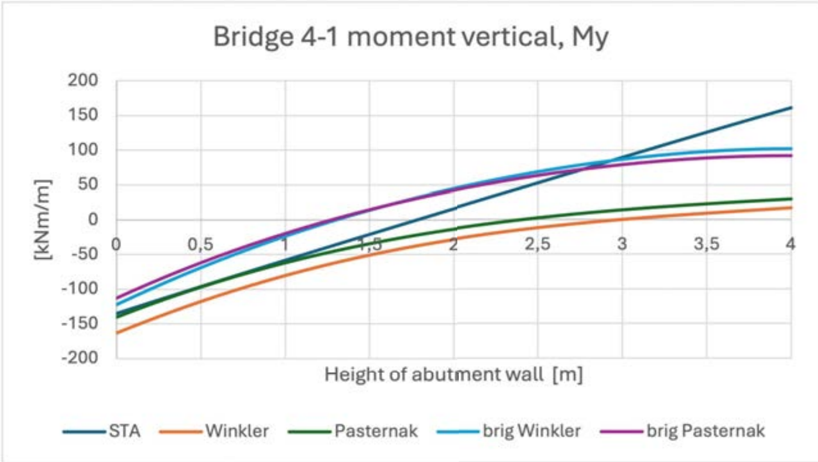

Figure A.117: Moment M_y, in horizontal result section 2, Bridge 4-1.

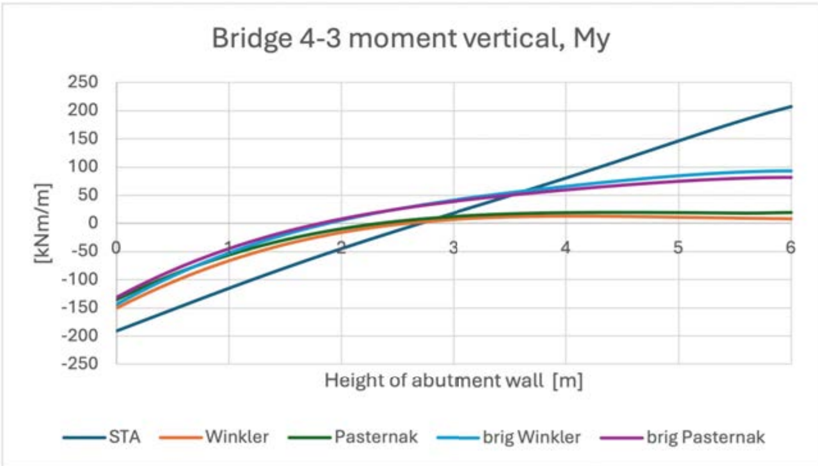

Figure A.118: Moment M_y, in horizontal result section 2, Bridge 4-3.

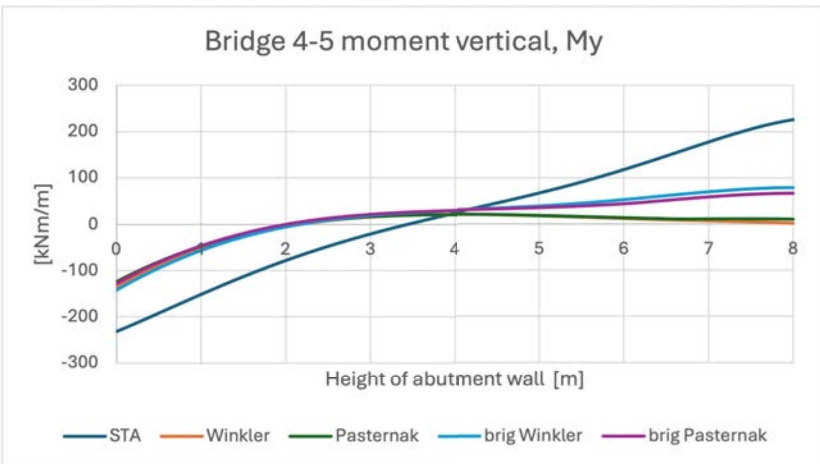

Figure A.119: Moment M_y, in horizontal result section 2, Bridge 4-5.

Shear forces in horizontal result section 2

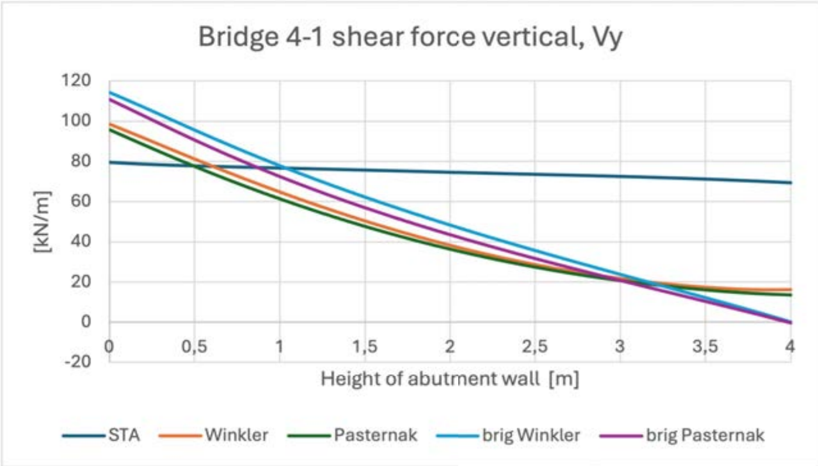

Figure A.120: Shear force V_y, in horizontal result section 2, Bridge 4-1.

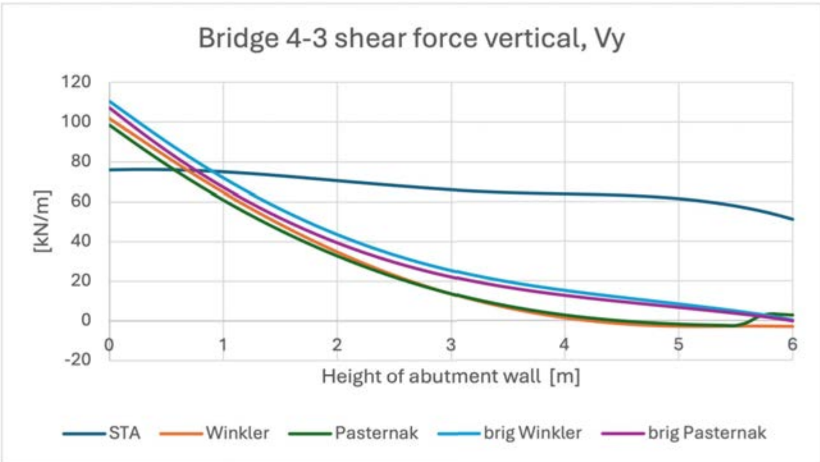

Figure A.121: Shear force V_y, in horizontal result section 2, Bridge 4-3.

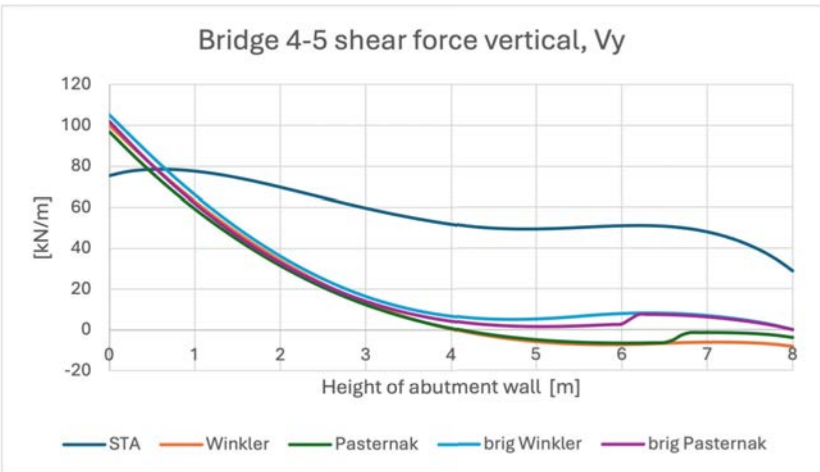

Figure A.122: Shear force V_y, in horizontal result section 2, Bridge 4-5.

A.9.6 Bridge 5

Horizontal deformation on the top of the abutment wall

Figure A.123: Top horizontal deformation on the abutment wall for Bridge 5-1.

Figure A.124: Top horizontal deformation on the abutment wall for Bridge 5-3.

Figure A.125: Top horizontal deformation on the abutment wall for Bridge 5-5.

Moments in horizontal result section 1

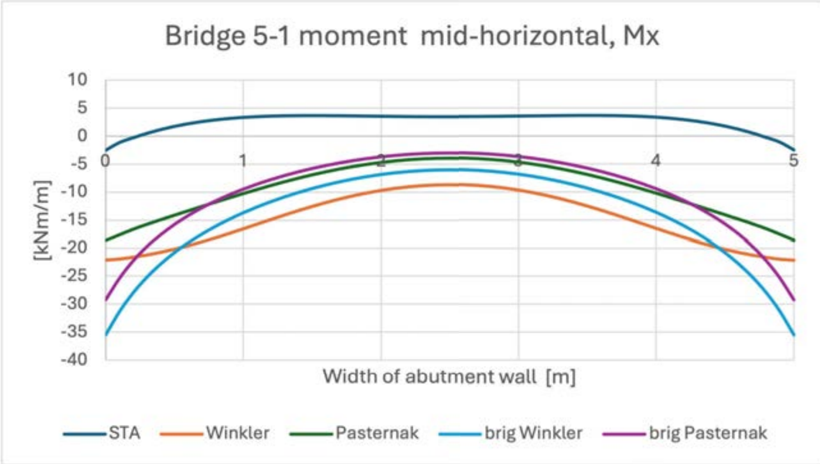

Figure A.126: Moment M_x, in horizontal result section 1, Bridge 5-1.

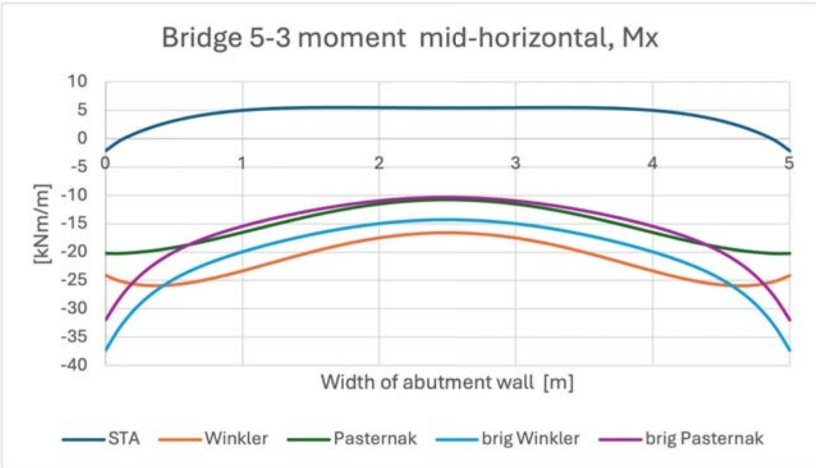

Figure A.127: Moment M_x, in horizontal result section 1, Bridge 5-3.

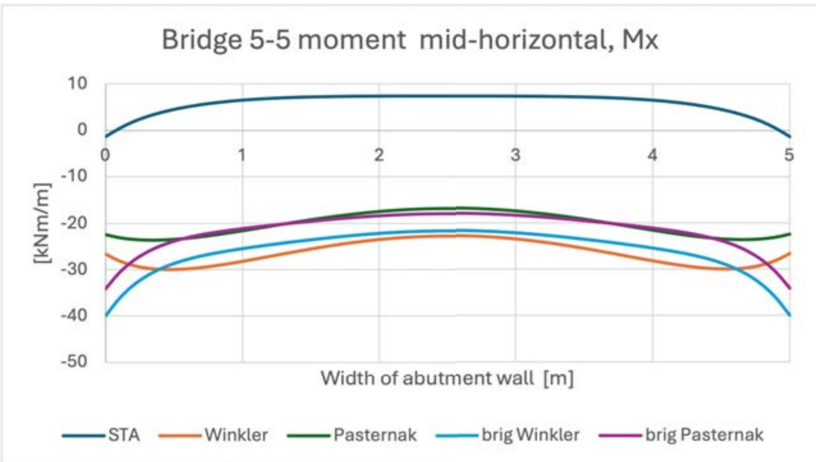

Figure A.128: Moment M_x, in horizontal result section 1, Bridge 5-5.

Shear forces in horizontal result section 1

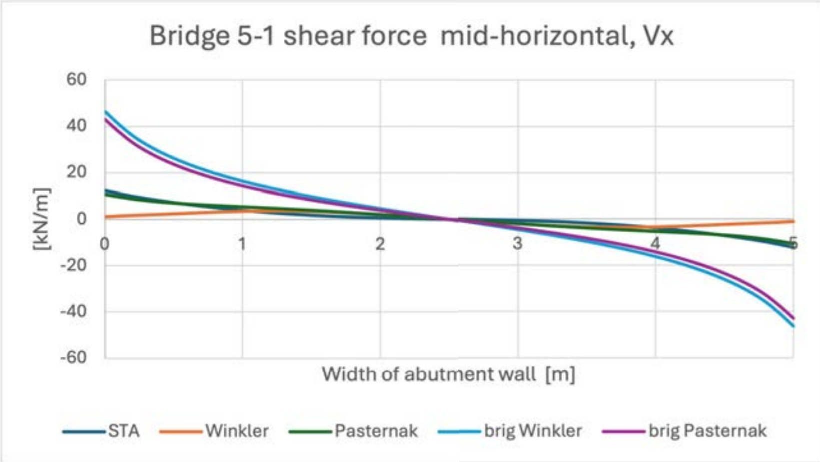

Figure A.129: Shear force V_x, in horizontal result section 1, Bridge 5-1.

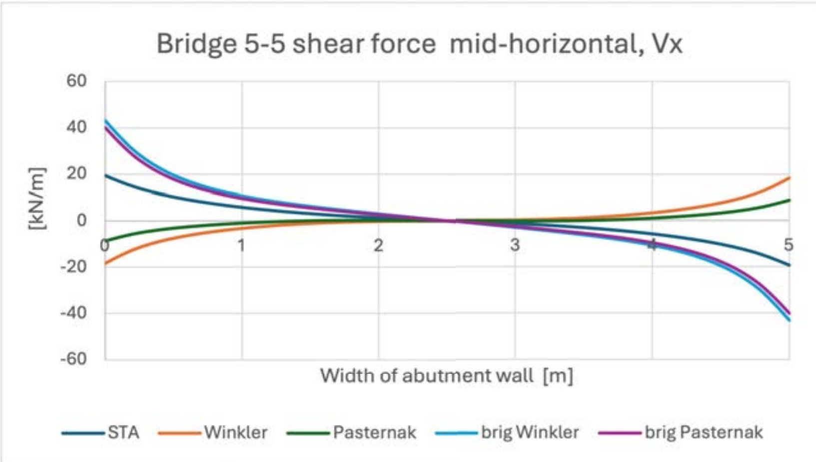

Figure A.130: Shear force V_x, in horizontal result section 1, Bridge 5-3.

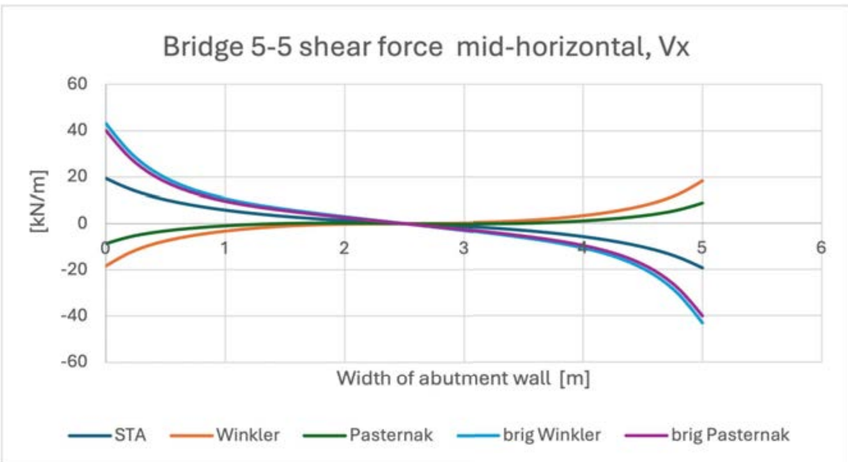

Figure A.131: Shear force V_x, in horizontal result section 1, Bridge 5-5.

Figure A.132: Shear force V_y, in horizontal result section 1, Bridge 5-1.

Figure A.133: Shear force V_y, in horizontal result section 1, Bridge 5-3.

Figure A.134: Shear force V_y, in horizontal result section 1, Bridge 5-5.

Moments in horizontal result section 2

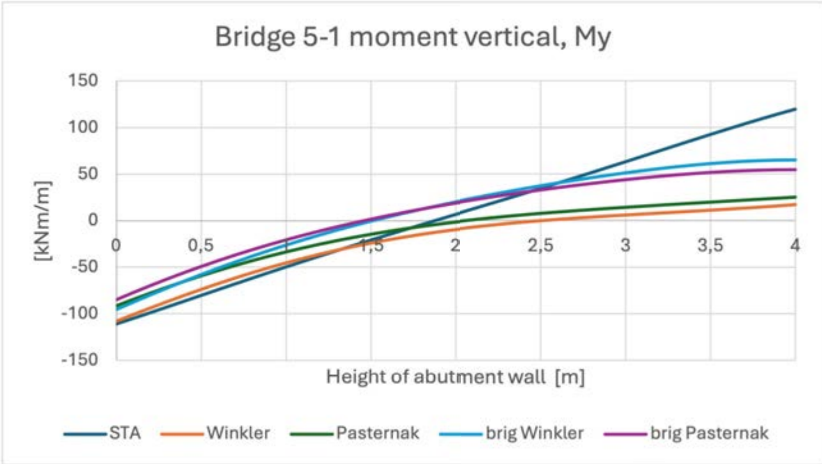

Figure A.135: Moment M_y, in horizontal result section 2, Bridge 5-1.

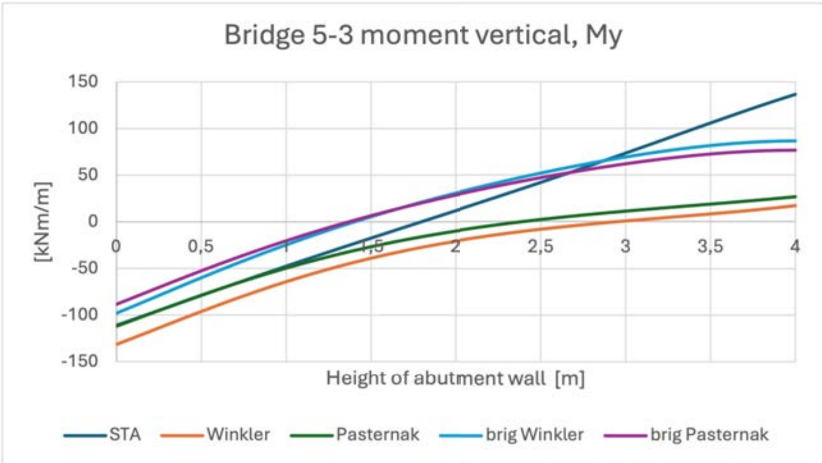

Figure A.136: Moment M_y, in horizontal result section 2, Bridge 5-3.

Figure A.137: Moment M_y, in horizontal result section 2, Bridge 5-5.

Shear forces in horizontal result section 2

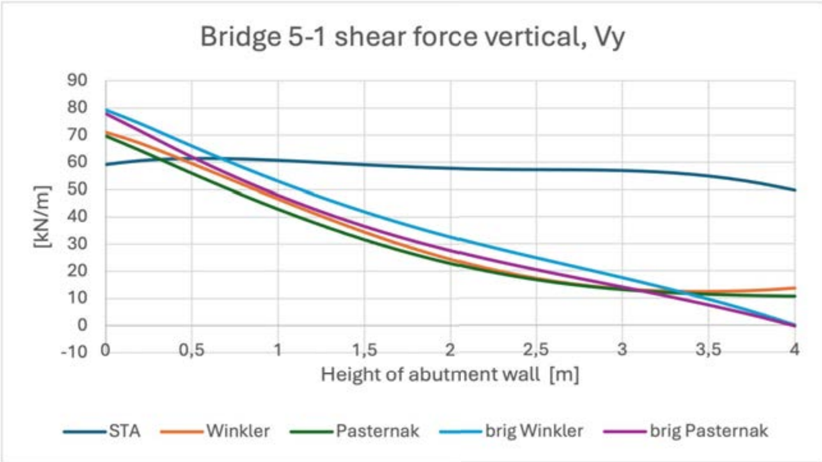

Figure A.138: Shear force V_y, in horizontal result section 2, Bridge 5-1.

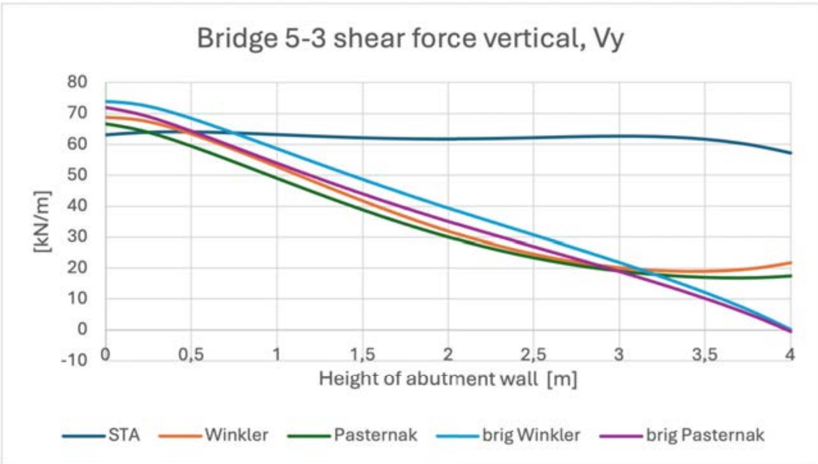

Figure A.139: Shear force V_y, in horizontal result section 2, Bridge 5-3.

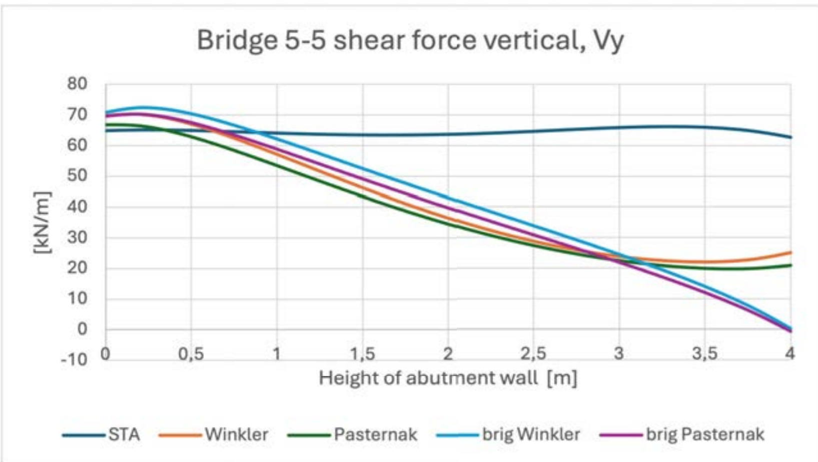

Figure A.140: Shear force V_y, in horizontal result section 2, Bridge 5-5.

A.9.7 Bridge 7

Horizontal deformation on the top of the abutment wall

Figure A.141: Top horizontal deformation on the abutment wall for Bridge 7-1.

Figure A.142: Top horizontal deformation on the abutment wall for Bridge 7-3.

Figure A.143: Top horizontal deformation on the abutment wall for Bridge 7-5.

Moments in horizontal result section 1

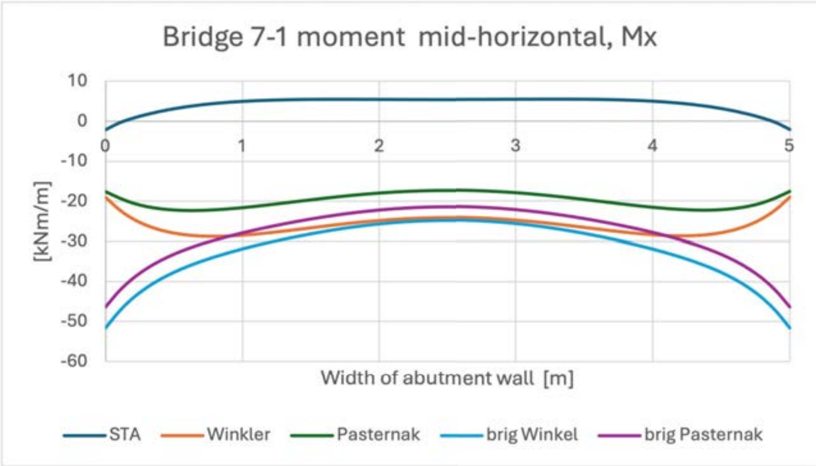

Figure A.144: Moment M_x, in horizontal result section 1, Bridge 7-1.

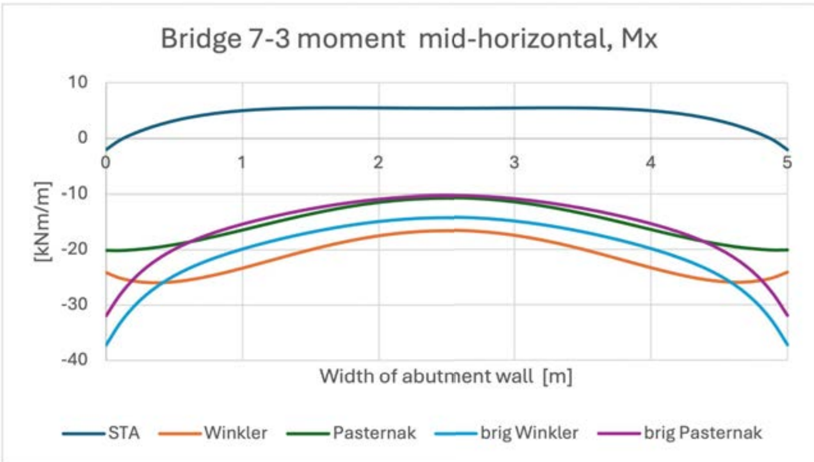

Figure A.145: Moment M_x, in horizontal result section 1, Bridge 7-3.

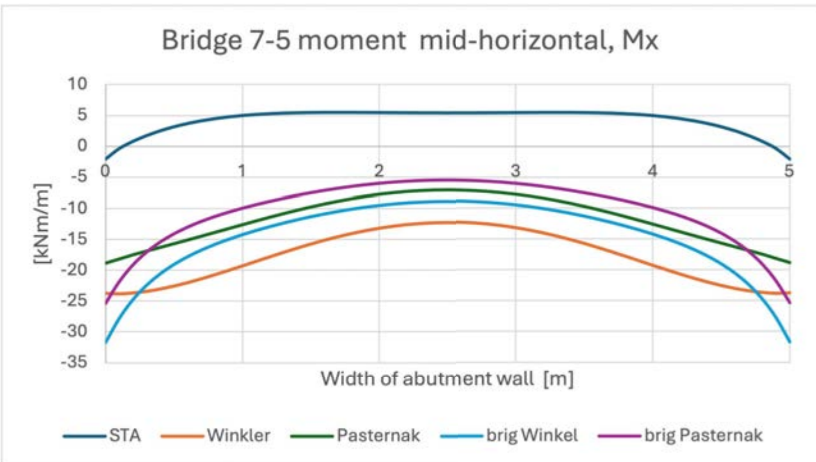

Figure A.146: Moment M_x, in horizontal result section 1, Bridge 7-5.

Shear forces in horizontal result section 1

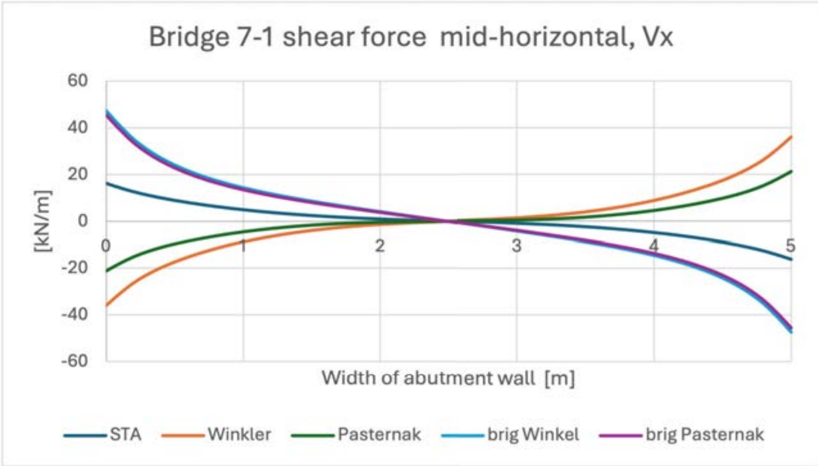

Figure A.147: Shear force V_x, in horizontal result section 1, Bridge 7-1.

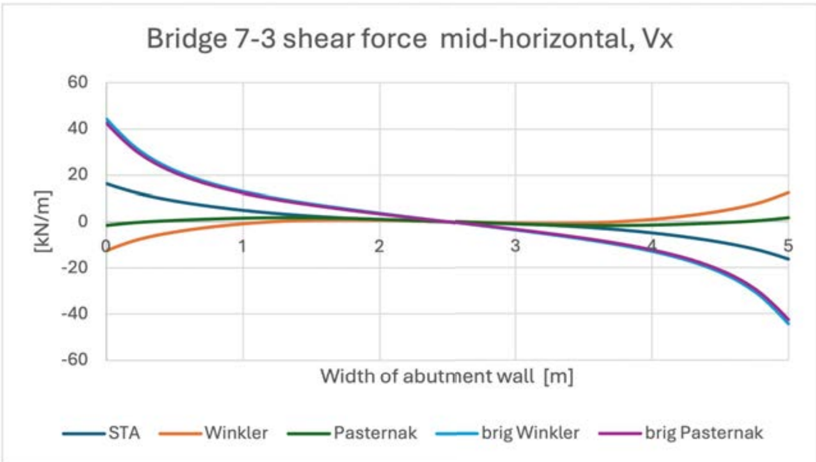

Figure A.148: Shear force V_x, in horizontal result section 1, Bridge 7-3.

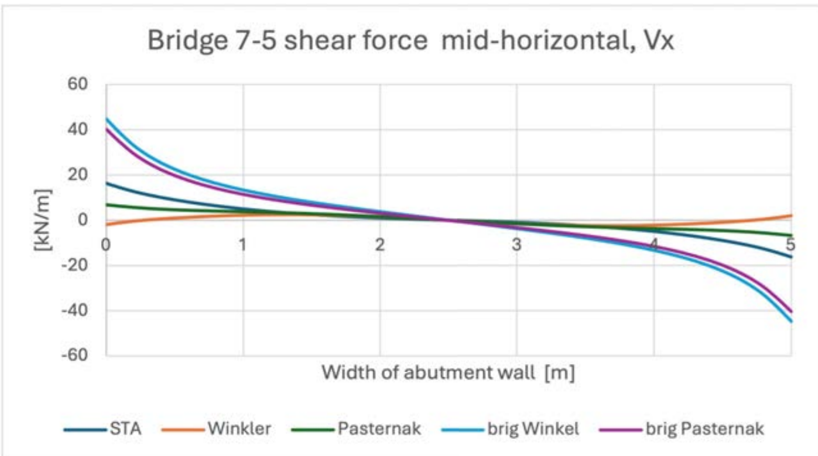

Figure A.149: Shear force V_x, in horizontal result section 1, Bridge 7-5.

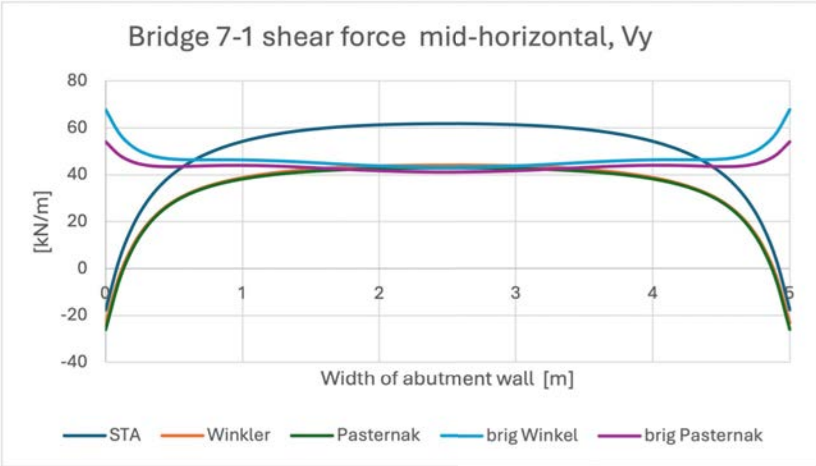

Figure A.150: Shear force V_y, in horizontal result section 1, Bridge 7-1.

Figure A.151: Shear force V_y, in horizontal result section 1, Bridge 7-3.

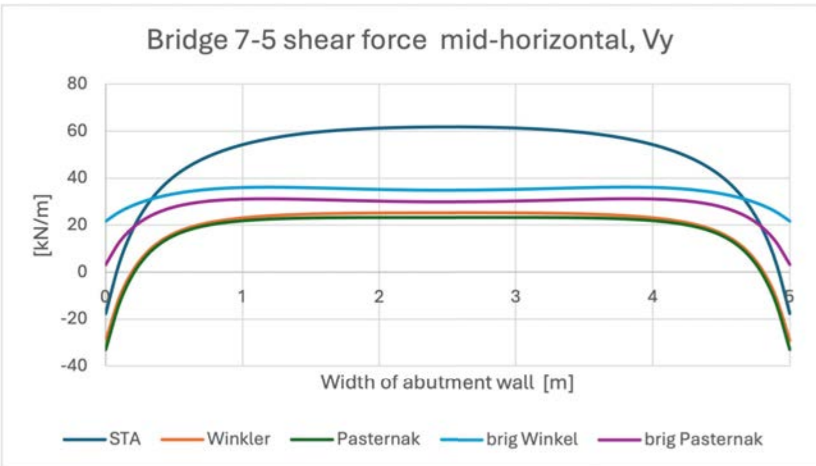

Figure A.152: Shear force V_y, in horizontal result section 1, Bridge 5-5.

Moments in horizontal result section 2

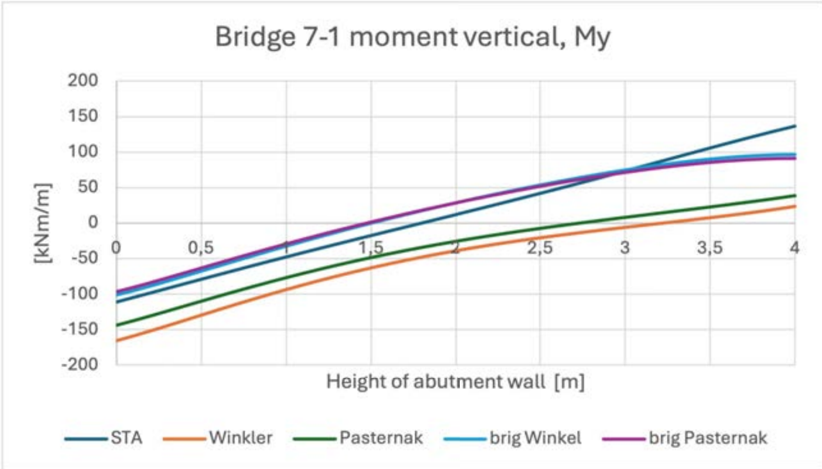

Figure A.153: Moment M_y, in horizontal result section 2, Bridge 7-1.

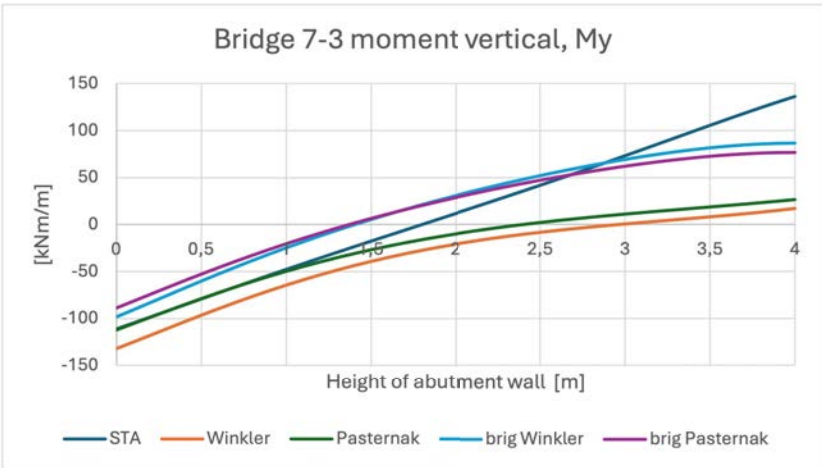

Figure A.154: Moment M_y, in horizontal result section 2, Bridge 7-3.

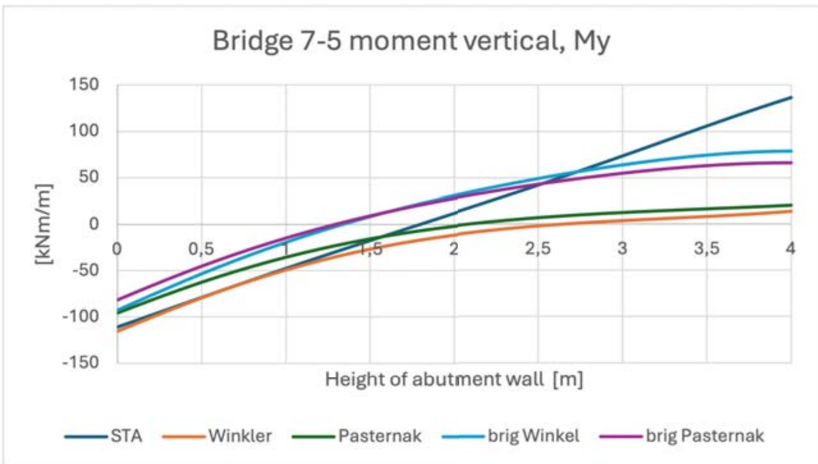

Figure A.155: Moment M_y, in horizontal result section 2, Bridge 7-5.

Shear forces in horizontal result section 2

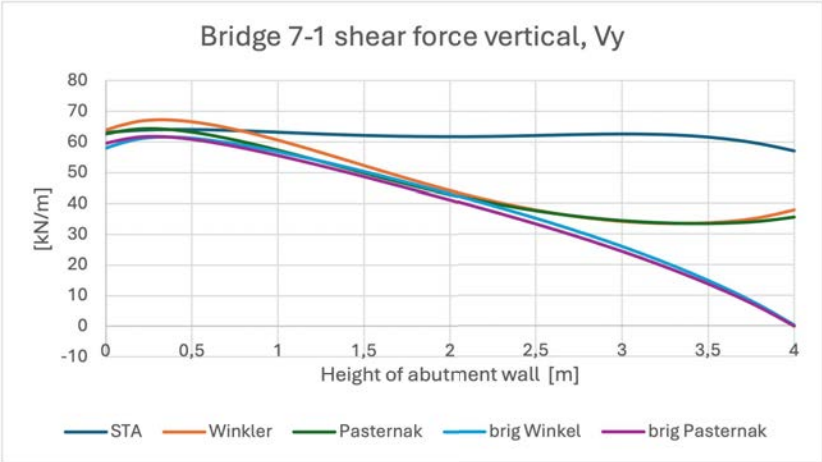

Figure A.156: Shear force V_y, in horizontal result section 2, Bridge 7-1.

Figure A.157: Shear force V_y, in horizontal result section 2, Bridge 7-3.

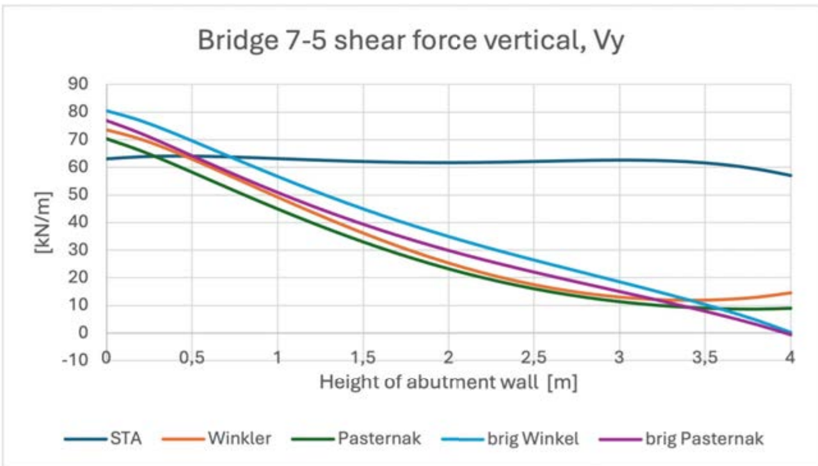

Figure A.158: Shear force V_y, in horizontal result section 2, Bridge 7-5.

A.9.8 Failure simulations

Horizontal deformation on the top of the abutment wall

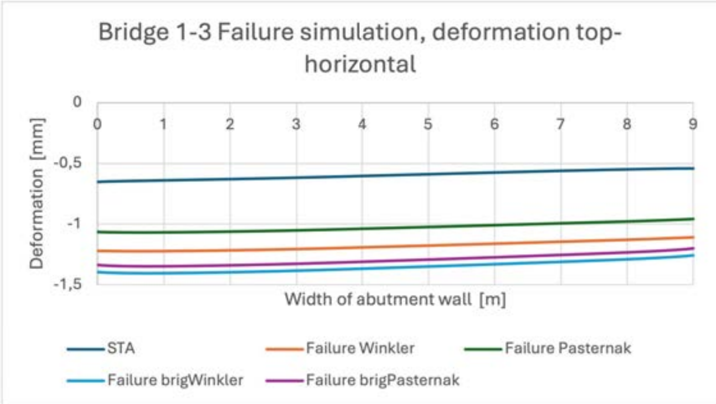

Figure A.159: Top horizontal deformation on the abutment wall for Failure simulations, Bridge 1-3.

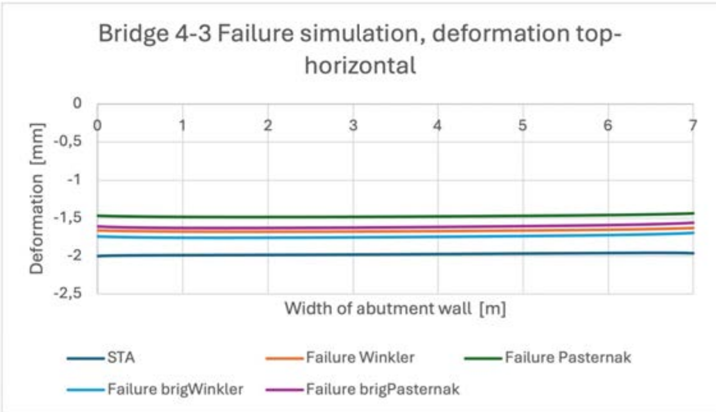

Figure A.160: Top horizontal deformation on the abutment wall for Failure simulations, Bridge 4-3.

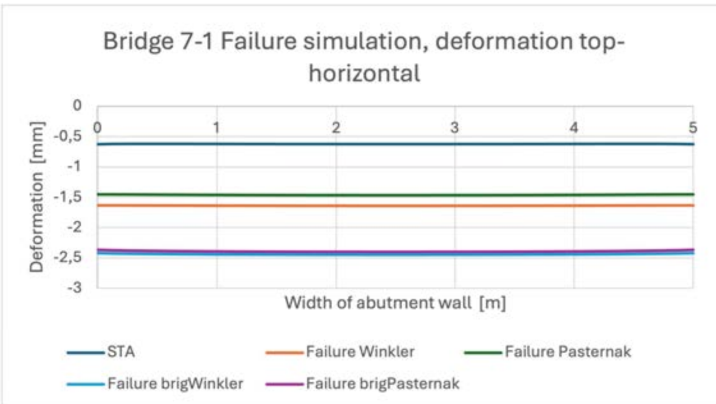

Figure A.161: Top horizontal deformation on the abutment wall for Failure simulations, Bridge 7-1.

Moments in horizontal result section 1

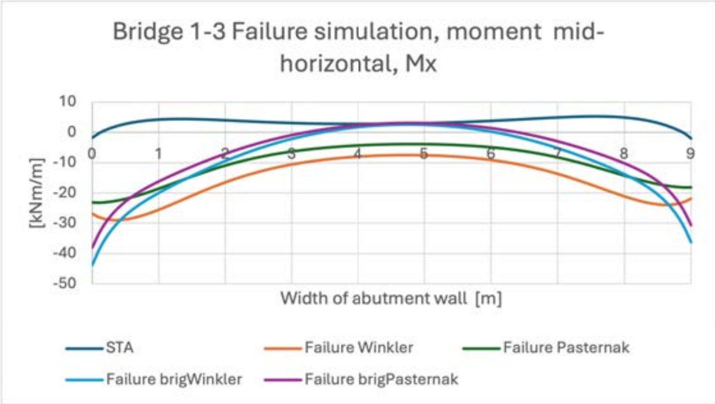

Figure A.162: Moment M_x, in horizontal result section 1, Failure simulations, Bridge 1-3.

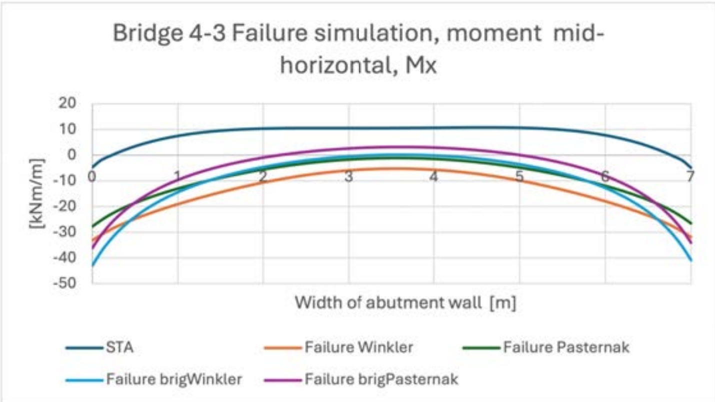

Figure A.163: Moment M_x, in horizontal result section 1, Failure simulations, Bridge 4-3.

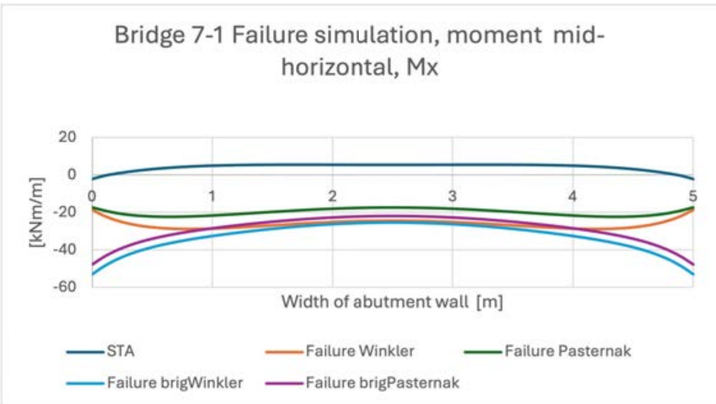

Figure A.164: Moment M_x, in horizontal result section 1, Failure simulations, Bridge 7-1.

Shear forces in horizontal result section 1

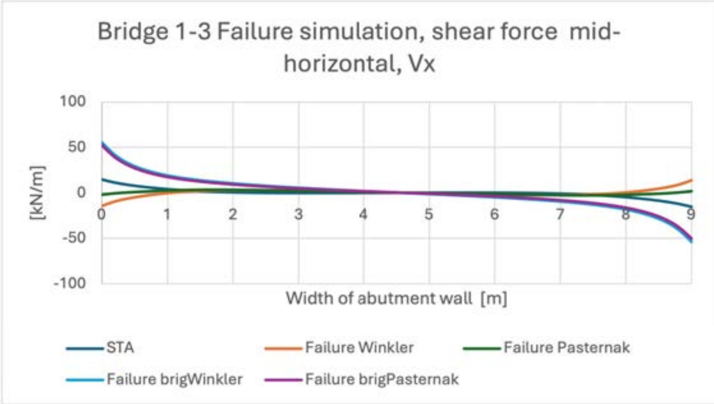

Figure A.165: Shear force V_x, in horizontal result section 1, Failure simulations, Bridge 1-3.

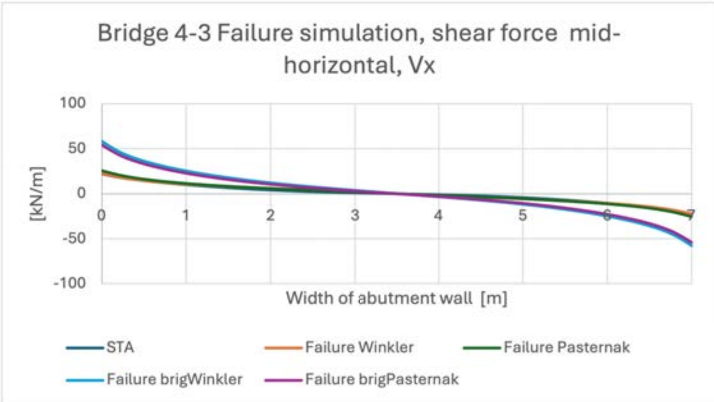

Figure A.166: Shear force V_x, in horizontal result section 1, Failure simulations, Bridge 4-3.

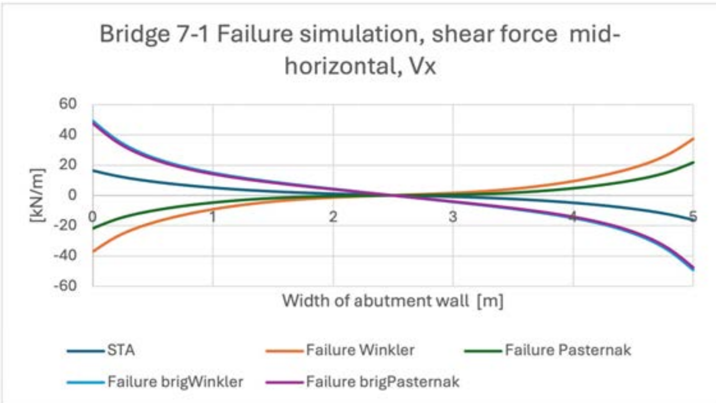

Figure A.167: Shear force V_x, in horizontal result section 1, Failure simulations, Bridge 7-1.

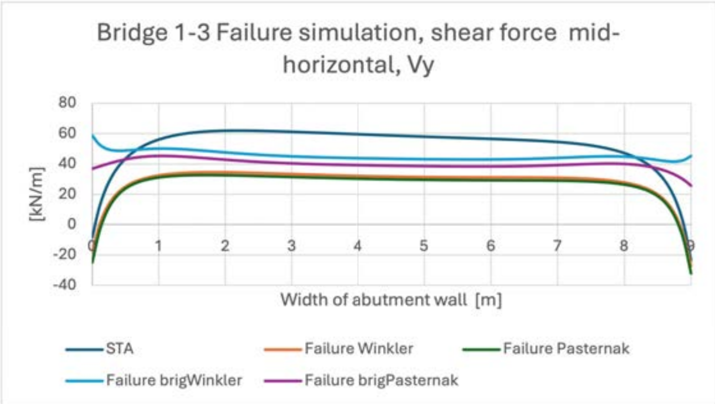

Figure A.168: Shear force V_y, in horizontal result section 1, Failure simulations, Bridge 1-3.

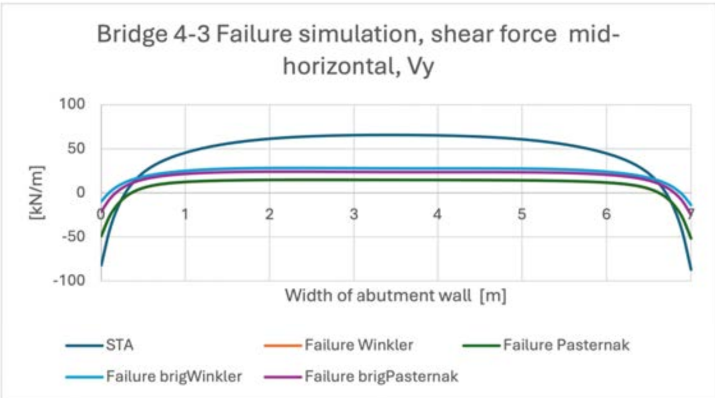

Figure A.169: Shear force V_y, in horizontal result section 1, Failure simulations, Bridge 4-3.

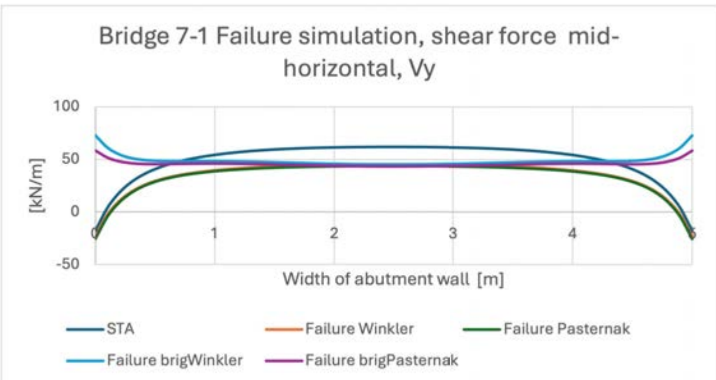

Figure A.170: Shear force V_y, in horizontal result section 1, Failure simulations, Bridge 7-1.

Moments in horizontal result section 2

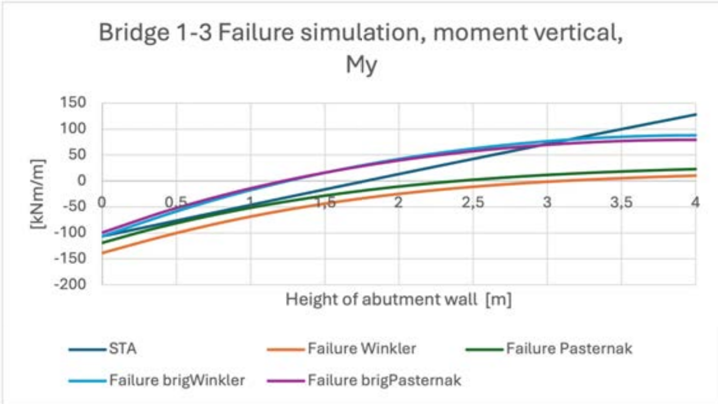

Figure A.171: Moment M_y, in horizontal result section 2, Failure simulations, Bridge 1-3.

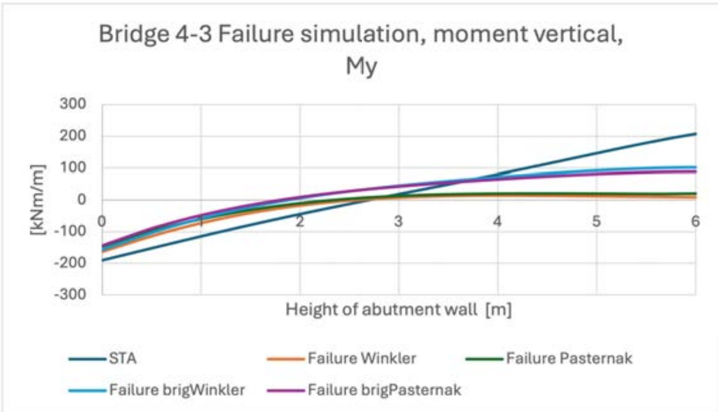

Figure A.172: Moment M_y, in horizontal result section 2, Failure simulations, Bridge 4-3.

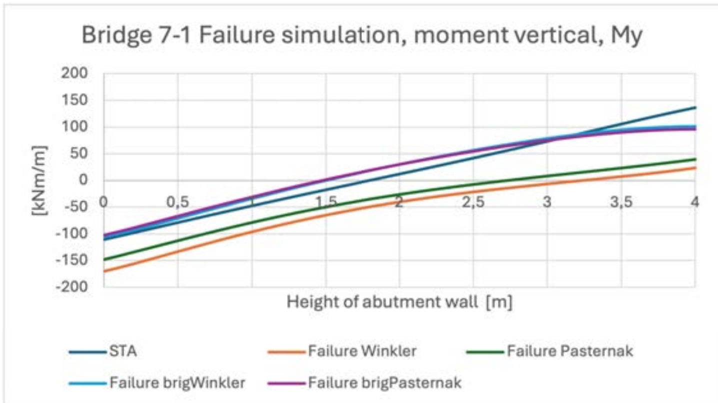

Figure A.173: Moment M_y, in horizontal result section 2, Failure simulations, Bridge 7-1.

Shear forces in horizontal result section 2

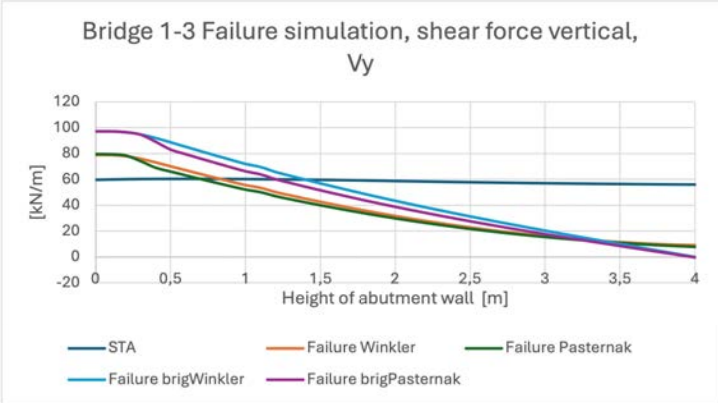

Figure A.174: Shear force V_y, in horizontal result section 2, Failure simulations, Bridge 1-3.

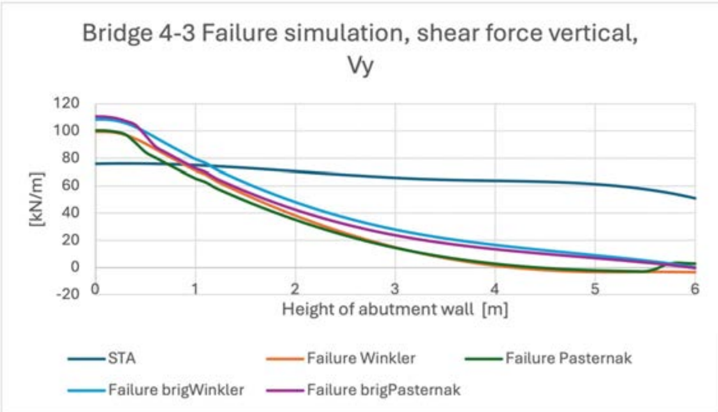

Figure A.175: Shear force V_y, in horizontal result section 2, Failure simulations, Bridge 4-3.

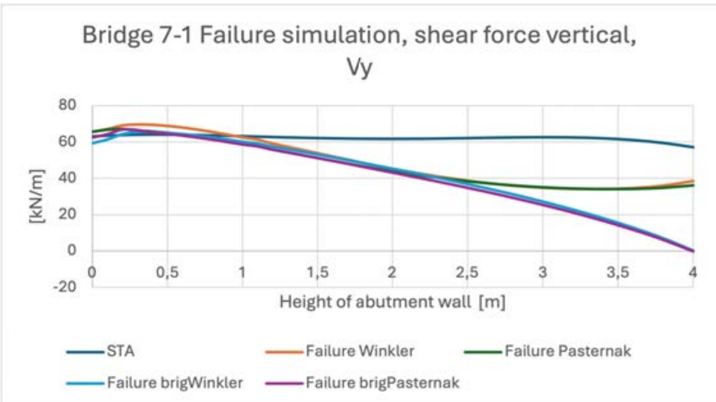

Figure A.176: Shear force V_y, in horizontal result section 2, Failure simulations, Bridge 7-1.